

THERMAL HYDRAULIC MODELLING OF INTERMEDIATE HEAT EXCHANGER USED IN LIQUID METAL COOLED NUCLEAR REACTOR

THESIS

MAJOR PROJECT II

Submitted for partial fulfilment of the award for the degree of
Master of Technology
in
Thermal Engineering
Submitted by

GAURAV KRISHNAYATRA

Roll No. – 2K18/THE/22

Under the supervision of

DR. RAJESH KUMAR

Professor

Department of Mechanical Engineering



Delhi Technological University

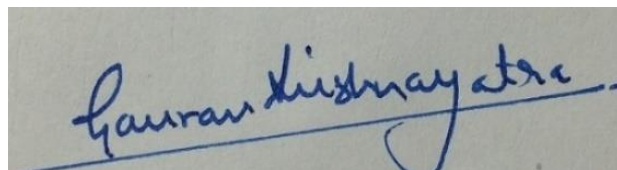
Shahbad Daultpur, Main Bawana Road, Delhi-110042, India

(Formerly known as Delhi College of Engineering)

August 2020

DECLARATION

I hereby declare that this submission of the THESIS of MAJOR PROJECT II titled “THERMAL HYDRAULIC MODELLING OF INTERMEDIATE HEAT EXCHANGER USED IN LIQUID METAL COOLED NUCLEAR REACTOR” towards the partial fulfilment for the award of MASTER OF TECHNOLOGY in THERMAL ENGINEERING from Delhi Technological University (formerly known as Delhi College of Engineering), New Delhi, India, is my authentic work and that to the best of my knowledge and belief, it contains no material previously written or published by another person and it has not been accepted for the award of any other degree or diploma in other university or institute of higher learning; except where the works which I co-authored for the publications used in the thesis, and the data & research used in this study published by other authors are duly acknowledged in the thesis.

A photograph of a handwritten signature in blue ink on a light-colored background. The signature reads "Gaurav Krishnayatra" and is written in a cursive style. A horizontal line is drawn across the bottom of the signature.

GAURAV KRISHNAYATRA

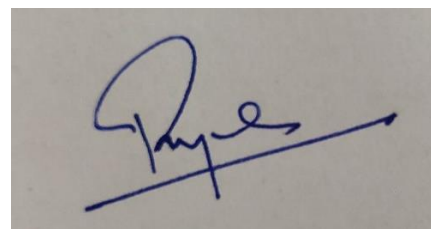
M.Tech | Thermal Engineering

Roll No. - 2K18/THE/22

gauravkrishnayatra_mt2k18@dtu.ac.in

CERTIFICATE

This is to certify that the THESIS of MAJOR PROJECT II titled “THERMAL HYDRAULIC MODELLING OF INTERMEDIATE HEAT EXCHANGER USED IN LIQUID METAL COOLED NUCLEAR REACTOR” which is submitted by GAURAV KRISHNAYATRA (Roll no. 2K18/THE/22), in the partial fulfilment of the requirement for the award of the degree of MASTER OF TECHNOLOGY in THERMAL ENGINEERING from Delhi Technological University (formerly known as Delhi College of Engineering), New Delhi, India, is a record of the candidates own authentic work carried out by him under my supervision. The matter embodied in this thesis is original and has not been submitted for the award of any degree or diploma in any other university or higher learning institute, except the research which is the part of jointly-authored publications.

A handwritten signature in blue ink, appearing to read 'Rajesh', with a long horizontal stroke extending to the right.

DR. RAJESH KUMAR

Professor

Delhi Technological University

Shahbad Daulatpur, Main Bawana Road

Delhi - 110042

India

ACKNOWLEDGEMENT

It gives me a great sense of pleasure to present the report of the M.Tech. Major Project II undertaken during M.Tech. Final Semester. I owe a special debt of gratitude to Professor Dr Rajesh Kumar, Department of Mechanical Engineering, Delhi Technological University (formerly known as Delhi College of Engineering), Shahbad, Daulatpur, Delhi for his content support and guidance throughout the course of work. His sincerity, thoroughness and perseverance have been a constant source of our inspiration. It is only his cognizant efforts that our endeavours have seen the light of the day. Not only he guided me through the project but also his wisdom and personal advice has enlightened me for my personal growth and future life.

I would like to take this opportunity to mention the support and hard work of my colleague and very close Mr Sulekh Tokas with whom I co-authored various articles in prestigious international scientific journals.

I also take the opportunity to acknowledge the contribution of Dr Vipin, Head of the Department, Mechanical Department, Delhi Technological University, Shahbad, Daulatpur, Delhi for his full support and assistance during the development of the project. I also do not like to miss the opportunity to acknowledge the contribution of all faculty members of the department for their kind assistance and cooperation during the development of our project. Last but not the least, I acknowledge our friends for their contribution to the completion of the project.

ABSTRACT

The thesis is focussed on the numerical simulation of a double-pipe heat exchanger which has potential to be used as an Intermediate Heat Exchanger in a Liquid Metal Cooled Nuclear Reactor. The intermediate heat exchanger has liquid metal and 100% glycerol as the working fluids, where the liquid metal is flowing through the tube section and the glycerol is flowing through the annular section. In this thesis, two liquid metals used are Lead-Bismuth Eutectic (LBE) & Liq. Sodium. The thermophysical properties along with the advantages and disadvantages of liquid metals are explained in the theoretical section of the thesis. The thermal-hydraulic principals of the liquid metal heat transfer are explained by the governing equations and the study of the boundary layer for liquid metals.

The geometrical models of the heat exchangers are designed in the Solidworks software and the meshing & the simulations are performed on ANSYS FLUENT. The heat transfer and fluid flow analysis are carried out by varying the inlet conditions and length of the heat exchanger, the inlet boundary conditions like inlet temperature of liquid metal, inlet velocity of the liquid metal, and the inlet temperature of the glycerol were varied, and a total number of 360 cases of heat exchangers were simulated. The thermal performance characteristics like Total rate of heat transfer, Overall heat transfer coefficient, pressure drop, and Logarithmic mean temperature difference were analyzed with the variations in the inlet conditions. All the fluid velocities were in the

turbulent flow region therefore, realizable $k - \varepsilon$ model with enhanced wall treatment was chosen for Turbulent modelling.

The thermal boundary layers were analyzed by the pictorial representation of the temperature profile of the axial cross-section of the heat exchanger under steady-state heat transfer process. The heat transfer rate, overall heat transfer coefficient, and LMTD were plotted against various inlet variables in order to assess their variation with the variation in the inlet conditions. It was observed that the overall heat transfer coefficient can be treated as a function of independent variables namely; the thermal conductivity of liquid metal, Reynolds number & Prandtl number of liquid metal, the inlet temperature of glycerol, and the length of the heat exchanger. Non-linear regression analysis was performed by developing a correlation between the overall heat transfer coefficient and the independent variables using the Generalized Reduced Gradient (GRG) algorithm. The predicted values from the correlation for LBE heat exchanger have R^2 score of 0.9847 and Liq. sodium heat exchanger has R^2 score of 0.9624.

Artificial Neural Network algorithm is used for regression analysis as well, a back-propagation feed-forward network was utilized. The input layer has 5 input variables which are the above-mentioned independent variables and the output layer has 1 variable which is the overall heat transfer coefficient. The prediction done by the ANN algorithm showed some remarkable accuracies, for LBE heat exchanger the R^2 score is 0.9964 with the configuration (6, 8, 6) and for Liq. sodium the R^2 score is 0.9918 with the configuration (10, 12, 10). The configurations represent the hidden layers with the corresponding number of nodes in them.

The analysis of the heat transfer and fluid flow characteristics were analyzed to assess their dependence on the input conditions which were later utilized in developing a correlation and regression analysis was performed. Along with the non-linear regression analysis, the ANN technique was used to predict the overall heat transfer coefficient. It was noted that ANN predictions were relatively more accurate than the predictions by the developed correlations. These techniques are quite robust, precise and relatively easy in use; therefore, these techniques can be used by thermal system design engineers in the future for the double-pipe heat exchanger with liquid metal heat transfer which will inherently reduce the time and cost of CFD simulations.

CONTENTS

DECLARATION	ii
CERTIFICATE	iii
ACKNOWLEDGEMENT	iv
ABSTRACT.....	v
CONTENTS.....	viii
NOMENCLATURE	xi
LIST OF FIGURES	xvi
LIST OF TABLES.....	xx
1. INTRODUCTION	2
1.1. Nuclear Energy	2
1.2. Nuclear Fission	3
1.3. Thermal Energy Production in Reactor	5
1.4. Nuclear Reactors.....	8
1.5. Liquid Metal Fast Breeder Reactors	12
1.5.1. Loop Design.....	15
1.5.2. Pool Design.....	16
1.5.3. Liquid Metal Coolants	17
1.6. Thesis Objective	19
2. LITERATURE SURVEY	21
3. THERMAL HYDRAULICS OF LIQUID METALS	33
3.1. Liquid Metals & Dimensionless Numbers.....	38

3.2. Boundary Layer Theory	40
3.3. Turbulent Flow	44
3.4. Pressure Drop in Liquid Metals	46
3.5. Heat Transfer in Liquid Metals.....	48
3.5.1. Constant Heat Flux	49
3.5.2. Constant Temperature.....	49
3.6. Turbulent Prandtl Number	51
3.7. Properties of Liquid Metals	52
I. Sodium.....	52
II. Lead-Bismuth Eutectic	53
III. Mercury.....	54
3.8. Intermediate Heat Exchanger Designing	55
3.9. Heat Transfer Enhancements	58
4. NUMERICAL MODELLING	62
4.1. CFD Modelling	63
4.2. Turbulence Modelling.....	66
4.3. Mesh Formations	70
4.4. Validation.....	74
4.5. Artificial Neural Network Modelling	77
5. RESULTS AND DISCUSSION.....	82
5.1. Effect of Reynolds Number	85
5.2. Effect of Inlet Temperature.....	92
5.3. Effect of Extended Surfaces	97
5.4. Comparison of LBE & Liq. Sodium.....	103
5.5. Correlation Formation.....	105
5.6. ANN Regression Analysis	108
6. CONCLUSIONS	111

REFERENCES	113
Appendix A.....	121
User Defined Functions	121
Appendix B.....	125
ANN Python Code.....	125
LIST OF PUBLICATIONS	129

NOMENCLATURE

Symbol	Description	Formula	Unit
ΔM	Mass defect		Amu/kg
M_X	Mass of nucleus		Amu/kg
M_p	Mass of 1 proton		Amu/kg
M_n	Mass of 1 neutron		Amu/kg
Z	Number of protons in nucleus		
N	Number of neutrons in nucleus		
V_r	Volume of reactor fuel		m^3
ϕ_m	average neutron flux		$1/m^2$
n	Number density of neutron projected on fission cross-section		
σ_f	Fission cross-section area		m^2
Σ_f	macroscopic fission cross-section		$1/m$
Q_r	Thermal energy produced in reactor	$Q_r = 200VN_f$	MeV
N_f	Average number of nuclear reactions taking place per unit volume of reactor		$1/m^3$
M_f	Mass of fissile material in reactor		kg
N_A	Avogadro's Number		$1/mol$
F_r	Number of fissile atoms per unit mole fuel		$1/mol$
q_r	Thermal energy produced in reactor per kg of fuel	$q_r = 3.20 \times 10^{-11} \frac{N_A}{F} \sigma_f \phi_m$	MeV/kg
q'	Thermal energy generated per unit volume of nuclear fuel	$q' = 3.20 \times 10^{-11} \frac{M_f N_A}{F V} \sigma_f \phi_m$	MeV/ m^3
N_{rod}	Number of fuel rods in single assembly		
A_{rod}	Area of single fuel rod		m^2
V_{rod}	Volume of single fuel rod		m^3

L_{rod}	Length of single fuel rod		m
Q_{den}	Volumetric Thermal power density	$Q_{den} = \frac{Q_r}{N_{rod}V_{rod}}$	W/m^3
Q_{flux}	Heat flux at the fuel surface	$Q_{flux} = \frac{Q_r}{N_{rod}A_{rod}}$	W/m^2
Q_{lin}	Linear power density	$Q_{lin} = \frac{Q_r}{N_{rod}L_{rod}}$	W/m
N_a	Absorbed number of nuclei per second per unit volume	$N_a = n\sigma_a\phi_m$	
σ_a	absorption cross-section		
Σ_a	macroscopic capture cross-section		
g	number of nuclei absorbed per second	$g = V\Sigma_a\phi_m$	
G	Consumption of U-235	$G = 3.37 \times 10^{-20}V\Sigma_a\phi_m$	kg/s
k	Thermal conductivity		W/mK
c_p	Specific heat capacity		J/kgK
α	Thermal diffusivity	$\alpha = \frac{k}{\rho c_p}$	m^2/s
ρ	Density (general)		kg/m^3
F	Figure of Merit for coolants	$F = \frac{c_p^{2.8}\rho^2}{\mu^{0.2}}$	
μ	Dynamic Viscosity		kg/ms
ν	Kinematic Viscosity	$\nu = \frac{\mu}{\rho}$	m^2/s
T_{boil}	Boiling Temperature		K
T_{melt}	Melting Temperature		K
k_{breed}	Breeding Ratio	$k_{breed} = \frac{mass(^{239}_{94}Pu)}{mass(^{238}_{92}U)}$	
t	Time (general)		s
\vec{v}	Velocity vector	$\vec{v} = u\hat{i} + v\hat{j} + w\hat{k}$	m/s
V	Velocity magnitude	$V = \sqrt{u^2 + v^2 + w^2}$	m/s
u, v, w	Velocity in x, y, z directions		m/s
u^*, v^*, w^*	Non-dimensional velocities	$u^* \equiv \frac{u}{L_c}$	
x, y, z	Cartesian coordinates		m
x^*, y^*, z^*	Non-dimensional coordinates	$x^* \equiv \frac{x}{L_c}$	m
\bar{g}	Gravitation acceleration (general)		m/s^2
g	Magnitude of gravitational acceleration		m/s^2
p	Pressure		N/m^2

∇	Gradient or Divergence Vector	$\nabla = \frac{\partial}{\partial x} \hat{i} + \frac{\partial}{\partial y} \hat{j} + \frac{\partial}{\partial z} \hat{k}$	
∇^*	Non-dimensional Divergence	$\nabla^* \equiv \frac{\nabla}{D}$	
$\bar{\tau}$	Stress Tensor		N/m^2
\vec{F}	External Force		N
E	Total Energy per unit mass	$E = e + \frac{1}{2}V^2$	J/kg
\dot{q}	Heat generation per unit volume		J/m^3
e	Internal thermal energy		J/kg
I	Unit Tensor		
L_c	Characteristic Length		m
\vec{V}^*	Non-dimensional velocity vector	$\vec{V}^* \equiv \frac{\vec{V}}{V}$	
p^*	Non-dimensional pressure	$p^* \equiv \frac{p - p_\infty}{p_o - p_\infty}$	
T^*	Non-dimensional temperature	$T^* \equiv \frac{T}{T_\infty}$	
p_o	Reference Pressure		N/m^2
p_∞	Pressure at free stream velocity		N/m^2
T_∞	Temperature at free stream velocity		K
g^*	Non-dimensional gravitational acceleration		
Re	Reynolds Number	$Re = \frac{\rho V D}{\mu}$	
Fr	Froude Number	$Fr = \frac{V}{\sqrt{gD}}$	
Pr	Prandtl Number	$Pr = \frac{\nu}{\alpha}$	
Eu	Euler Number	$Eu = \frac{p_o - p_\infty}{\rho V^2}$	
Pe	Peclet Number	$Pe = Re \cdot Pr$	
Re_L	Reynolds number based on Length L	$Re = \frac{\rho V L}{\mu}$	
Re_h	Reynolds number of hot fluid		
Pr_h	Prandtl number of hot fluid		
δ_h	Hydrodynamic Boundary layer		
δ_{th}	Thermal Boundary layer		
τ_w	Shear stress at the wall	$\tau_w = \mu \frac{\partial u}{\partial y}_{y=0}$	
f_D	Darcy friction factor	$f_D = \frac{\tau_w}{\rho V_{avg}^2 / 8}$	
Δp_L	Pressure drop for length L	$\Delta p_L = f_D \frac{L}{D} \frac{\rho V_{avg}^2}{2}$	
V_{avg}	Average velocity		m/s

h_x	Local convective heat transfer coefficient		W/m^2K
Nu_x	Local Nusselt number	$Re = \frac{\rho V x}{\mu}$	
u', v', w'	Fluctuating Turbulent Velocities		m/s
$\bar{u}, \bar{v}, \bar{w}$	Mean Velocities		m/s
\bar{P}	Mean Pressure		Pa
P'	Fluctuating Turbulent Pressure		Pa
\bar{T}	Mean Temperature		K
T'	Fluctuating Turbulent Temperature		K
τ_{turb}	Turbulent Shear Stress	$\tau_{turb} = \mu_t \frac{\partial \bar{u}}{\partial y}$	
μ_t	Turbulent Viscosity		kg/ms
ν_t	Turbulent Kinematic Viscosity	$\nu_t = \frac{C_v k^2}{\varepsilon}$	m^2/s
τ_{total}	Total Shear Stress	$\tau_{total} = \rho(\nu + \nu_t) \frac{\partial \bar{u}}{\partial y}$	N/m^2
q_{turb}	Turbulent heat transfer from the surface	$q_{turb} = -k_t \frac{\partial T}{\partial y}$	W/m^2
\dot{q}_{total}	Total Rate of Heat Transfer	$\dot{q}_{total} = -(k + k_t) \frac{\partial T}{\partial y}$	W/m^2
α_t	Turbulent thermal diffusivity		m^2/s
Pr_t	Turbulent Prandtl number	$Pr_t = \frac{\nu_t}{\alpha_t}$	
ϵ_R	Surface Roughness		mm
f	fanning friction factor	$f = \frac{f_D}{4}$	
ψ	Eddy thermal diffusivity/Eddy momentum diffusivity	$\psi = \frac{\alpha_t}{\nu_t}$	
k	Turbulent kinetic energy		
ε	Turbulent dissipation rate		
ϵ	Effectiveness of fins		
z	Function used in ANN	$z_{11} = x_1 w_{11} + x_2 w_{12} + x_3 w_{13} + b_1$	
w_i	Weights values for ANN functions		
b_i	Bias values for ANN functions		
ΔT_{lm}	Logarithmic Mean Temperature Difference	$\Delta T_{lm} = \frac{(T_{hi} - T_{co}) - (T_{ho} - T_{ci})}{\ln \left(\frac{T_{hi} - T_{co}}{T_{ho} - T_{ci}} \right)}$	K
U	Overall heat transfer coefficient	$U = Q / A \Delta T_{lm}$	W/m^2K
U^*	Non-dimensional overall heat transfer coeff.	$U^* = \frac{U}{U_o}$	
U_o	Reference overall heat transfer coeff.		W/m^2K

T_{hi}	Inlet temperature of hot fluid	K
T_{ho}	Outlet temperature of hot fluid	K
T_{ci}	Inlet temperature of cold fluid	K
T_{co}	Outlet temperature of cold fluid	K
u_h	Velocity of hot fluid	m/s
u_c	Velocity of cold fluid	m/s
L_f	Length of fins	m
η_f	Efficiency of single fin	
η_o	Efficiency of fin-tube system	
u^+	Dimensionless velocity in turbulent flow	$u^+ = \frac{V}{u_\tau}$
y^+	Dimensionless distance from wall (normal)	$y^+ = \frac{u_\tau y}{\nu}$

List of Abbreviations

KE	Kinetic Energy
TE	Thermal Energy
IHX	Intermediate Heat Exchanger
LMFBR	Liquid Metal Fast Breeder Reactor
FBR	Fast Breeder Reactor
LMCR	Liquid Metal Cooled Reactor
LBE	Lead Bismuth Eutectic (liquid metal coolant)
LM	Liquid Metal
SG	Steam Generator
SS	Stainless Steel
HTC	Heat Transfer coefficient
GRG	Generalized Reduced Gradient
ANN	Artificial Neural Network

LIST OF FIGURES

Fig. 1.1 Diagrammatic representation of nuclear fission.....	4
Fig. 1.2 Schematic representation of general Nuclear Reactor.....	8
Fig. 1.3 A typical Reactor Fuel Assembly.....	9
Fig. 1.4 A standard Fuel Rod.....	10
Fig. 1.5 Schematic representation of the LMFBR.....	13
Fig. 1.6 Loop Design of the LMFBR.....	16
Fig. 1.7 Pool design of the LMFBR.....	17
Fig. 3.1 Showing the thermal boundary layer (red) and hydrodynamic boundary layer (blue) (a) for Liquid Metal (b) for non-metallic fluids.....	41
Fig. 3.2 x-velocity with time showing average and fluctuating component.....	44
Fig. 3.3 Three-Dimensional Model of the IHX.....	55
Fig. 3.4 Axial View of the IHX.....	56
Fig. 3.5 Cross-sectional view of the IHX showing the various diameters of tube and the annulus region.....	56
Fig. 3.6 Cross-section of IHX with fins.....	59
Fig. 4.1 1/4 th Symmetrical 3D Model of the IHX showing the wall of symmetry	64
Fig. 4.2 2-Dimensional Model of IHX used for simulation.....	65
Fig. 4.3 Variation of Total Heat Transfer with Reynolds number showing comparisons between 3-dimensional & 2-dimensional CFD results.....	65
Fig. 4.4 Different layers near turbulence near the wall in hydraulic boundary layer	68

Fig. 4.5 Non-dimensional velocity profile for near the wall	69
Fig. 4.6 y^+ values for LBE and Liq. sodium for various inlet boundary conditions and length of IHX	70
Fig. 4.7 Axial view of Meshing of 3D model of IHX	71
Fig. 4.8 Lateral view of 3D model of IHX showing the uniformity in meshing	71
Fig. 4.9 Close up view of Meshing showing inflation region near the fluid-tube interface	72
Fig. 4.10 Meshing of 3D model of IHX with fins	72
Fig. 4.11 Close up view of Meshing of 3D model of IHX with fins showing the inflation regions near tube walls	73
Fig. 4.12 Meshing of 2D model of IHX showing the near wall treatment	73
Fig. 4.13 The Nusselt number variation with increasing Peclet number for constant heat flux	74
Fig. 4.14 The Nusselt number variation with increasing Peclet number for isothermal tube wall.....	75
Fig. 4.15 2D model of Johnson's Experiment	76
Fig. 4.16 Meshing of 2D model of Johnson's Experiment.....	76
Fig. 4.17 Nu vs Pe for Johnson's [50] and current CFD result with Mochizuki's [33] for Mercury	77
Fig. 4.18 Nu vs Pe for Johnson's [50] and current CFD result with Mochizuki's [33] results for LBE.....	77
Fig. 4.19 Flow chart showing the steps of artificial neural network programming...	78
Fig. 4.20 Artificial Neural Network showing the number of layers and nodes	80
Fig. 5.1 Thermal boundary layer & density variation for Liq. Na with L=250mm...	83
Fig. 5.2 Thermal boundary layer & density variation for LBE with L=500mm	84

Fig. 5.3 Thermal boundary layer & density variation for Liq. Na with L=1000 mm	84
Fig. 5.4 Thermal boundary layer of Glycerol for L=250mm for a) LBE b) Liq. Na.	85
Fig. 5.5 Thermal boundary layer of Glycerol for L=1000mm for a) LBE b) Liq. Na	85
Fig. 5.6 Variation of total rate of heat transfer with increasing Reynolds number for L=250mm for various inlet conditions	87
Fig. 5.7 Variation of total rate of heat transfer with increasing Reynolds number for L=500mm for various inlet conditions	88
Fig. 5.8 Variation of total rate of heat transfer with increasing Reynolds number for L=1000mm for various inlet conditions	89
Fig. 5.9 Skin friction coefficient as the function of Reynolds number.....	90
Fig. 5.10 Pressure Drop variation with increasing Reynolds number for various IHX lengths and inlet temperatures	91
Fig. 5.11 Variation of overall heat transfer coefficient with inlet temperature of liquid metals for L = 250mm	93
Fig. 5.12 Variation of overall heat transfer coefficient with inlet temperature of liquid metals for L = 500mm	94
Fig. 5.13 Variation of overall heat transfer coefficient with inlet temperature of liquid metals for L = 1000mm	95
Fig. 5.14 Logarithmic mean temperature difference as the function of inlet temperature of liquid metal.....	96
Fig. 5.15 a) 3-Dimensional representation of the model used for simulation b) Schematic diagram showing the geometrical dimensions for [67].....	98
Fig. 5.16 a) Effectiveness as a function of number of fins for different fin lengths b) Effectiveness as a function of non-dimensional fin length for different N_f	99

Fig. 5.17 a) Schematic diagram showing the geometrical dimensions for [48] b) 3-Dimensional representation of the model	100
Fig. 5.18 a) Effectiveness as a function of non-dimensional fin spacing b) Effectiveness predicted with respect to computed effectiveness representing the accuracy of machine learning regression.....	101
Fig. 5.19 a) Effectiveness of the fins with increasing fin length b) Non-dimensional overall heat transfer coefficient as a function of fin length	102
Fig. 5.20 Showing a) density variation and b) temperature plume along the length at steady state heat transfer for N=16 fins and 5.5 mm fin length.....	102
Fig. 5.21 a) Prandtl number as a function of temperature for various liquid b) Thermal conductivity as a function of temperature for various liquid metals	103
Fig. 5.22 Total Rate of Heat Transfer comparison for LBE and Liq. sodium.....	104
Fig. 5.23 Predicted values and calculated values of overall heat transfer coefficient for LBE.....	107
Fig. 5.24 Predicted values and calculated values of overall heat transfer coefficient for Liq. sodium.....	107
Fig. 5.25 Predicted and computed values of overall heat transfer coefficient for LBE using ANN regression model.....	110
Fig. 5.26 Predicted and computed values of overall heat transfer coefficient for Liq. sodium using ANN regression model.....	110

LIST OF TABLES

Table 1.1 Thermophysical properties of various coolants	11
Table 1.2 Nuclear Reactors categorized by countries, capacity, coolant, moderator and neutron spectrum [48], [3].	12
Table 1.3 Breeding Ratios values and respective type of reactors	14
Table 2.1 Specification of IHX in JOYO, MONJU & 50 MW-SG (flow rate conditions is specific for [28]).....	28
Table 3.1 Simplified Governing Equations in vector form, non-dimensional form, and differential form [59] & [39].	37
Table 5.1 Geometrical Parameter of the Finned-tube system.....	98
Table 5.2 Variables taken for ANN regression analysis.....	108
Table 5.3 ANN configuration with the corresponding R^2 values for LBE.....	109
Table 5.4 ANN configuration and the corresponding R^2 values for Liq. sodium ...	109

Chapter 1 – Introduction

This chapter is an introduction to the thesis which initiates with explanation of nuclear energy and concluded with the thesis objective. Various type of nuclear power plants and their schematic diagrams have been briefly mentioned and all the essential parts of a nuclear reactor have been explained. The purpose of this thesis is to explain the utilization of liquid metals and comparison of their heat transfer capabilities for intermediate heat exchanger used in liquid metal fast breeder reactor (LMFBR) therefore, main focus of chapter 1 is the working and functioning of the LMFBR.

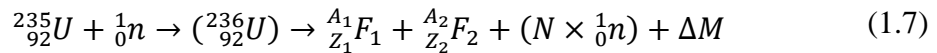
1. INTRODUCTION

1.1. Nuclear Energy

Nuclear energy is the energy released during the fission reaction of radioactive elements due to the mass defect. Nuclear energy in today's time is one of the most important sources of power in the world with the added benefits of moderate ecological impact and low carbon footprint. Nuclear reactors use various radioactive elements like Uranium, Plutonium and Thorium as a natural source for energy production. There are several key aspects of working and analysis of a nuclear reactor, like fuel rod design, radiation cladding, disaster mitigation, electric power conversion and thermal energy production. The Nuclear reaction produces extremely high thermal energy which has to be controlled and converted to electric energy in an efficient manner which is the basic intention of nuclear-thermal engineering. There are 440 power-producing Nuclear reactors and a little over 200 research reactors. As of 2018 nuclear power plants supplied about 2500 TWh of electric power to the world which is 10.2% of the total power demand. Countries like Sweden, France, Slovenia, Belgium, Bulgaria, Finland, Czech Republic & Switzerland cover more than 50% of their power demand by Nuclear energy however countries namely USA, UK, Spain, Romania, Russia and South Korea cover about 30% from nuclear [48]. For the case of India, only 1.5% of total energy demand is met by nuclear power even though India has been enhancing its research and development in the sector of nuclear engineering.

1.2. Nuclear Fission

When is there an interaction between a neutron and a fissile element's atoms nuclear reaction takes place resulting in two or more neutrons and a variety of other elements. In nuclear fission, a neutron is projected onto a heavy atom and along with 2 different type of elements and few neutrons [1], there is a release of enormous energy because of the mass defect caused due to disintegration and integrations of different nuclei as shown in Fig.1.1. For a better understanding of the matter at hand, a practical nuclear fission reaction of U-235 is explained in the coming section of the thesis.



Where, F_1 & F_2 are the fission product, N is the number of neutron release which is 2.5 on average and ΔM is the mass defect which is discharged as γ rays.

When a nucleus is disintegrated into its constituents, neutron and proton, there is an overall difference in mass. Mass of nucleus is lower than the mass of protons and neutrons when they are separated.

$$M_X + \Delta M = Z \cdot M_p + N \cdot M_n \quad (1.8)$$

Where ΔM is called the mass defect, M_X is the mass of nucleus, M_p is the mass of single proton, M_n is the mass of single neutron, Z is the number of protons in nucleus, and N is the number of neutrons in the nucleus. During a nuclear fission reaction, this mass defect having extremely high velocity is converted to energy since energy and mass are equivalent to each other according to the general theory of relativity.

The fission products F_1 & F_2 have to follow a combination.

$$A_1 + A_2 = 235 + 1 - 2 = 234 \quad (1.9)$$

$$Z_1 + Z_2 = 92 \quad (1.10)$$

After following this combination, during the course of nuclear reaction, there is almost 90 type of isotope production and these isotopes are disintegrated into two types of precursors giving a combination of 200 different types of radioactive nuclei for few hours before getting stabilized [1].

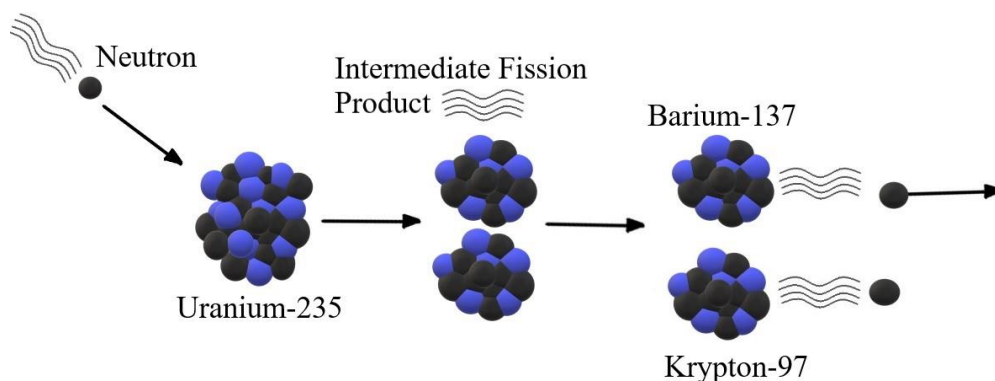


Fig. 1.1 Diagrammatic representation of nuclear fission of U-235

The products of fission reaction are called Fission Fragments. Initially, the energy released in fission fragments is in the form of kinetic energy. The kinetic energy decreases and it gets converted to thermal energy when these fragments collide with other nuclei of the unreacted fuel. In total there is about 207 MeV of released energy after fission reaction of a single U-235 atom, out of which 195 MeV is in thermal form. The kinetic energy of released neutrons (5 MeV) are utilized in the form of thermal energy in moderator, coolant and cladding material [2]. The types of fission decay are; β rays that have about 8 MeV, γ rays have 7 MeV and neutrinos have 12 MeV when they are released during fission reaction [1]. Special care is made during the designing for reactor chamber where the fission is taking place to contain such radiations and their energy levels. β particles are electrically charged and γ radiations are electromagnetic waves which are quite harmful to the human body are contained by the moderator where the radiation is absorbed and converted to thermal energy.

In nuclear fission reaction of U-235, 2.5 neutrons are released on an average. After the first nuclear fission when the neutrons are discharged, one of them is absorbed by the next U-235 nucleus, this gives us the 2nd generation of fission. Then consequently,

neutrons keep getting released and for each 2.5 release of neutrons in i^{th} generation fission, 1 neutron gets absorbed by the next U-235 to give $(i+1)^{\text{th}}$ generation fission. This continuous controlled fission is called the chain reaction by which the practical use of nuclear energy is possible. Now we know that out of every 2.5 neutron 1 is absorbed for fission reaction, therefore the controlling of released 1.5 neutrons is necessary, which is achieved by the nuclear reactor. The Nuclear reactor is either designed to convert the KE of the neutron to TE (Thermal reactors) or it gets absorbed by non-fissile U-238 to convert it into U-239 which in turns gets converted to Pu-239 (Fast Reactor) [2]. During a fission reaction, there are usually three types of neutrons released. Neutrons having energy < 0.1 MeV, they are primarily utilized in Nuclear Thermal Reactor. These neutrons are produced when fast neutrons are moderated by a medium in the thermal reactor. Neutrons having energy from 1 eV to 0.1 MeV, the reactors using these types of neutrons are called Intermediate Neutron Reactors. Neutrons having energy around 0.1 MeV and having velocity in the range of 10^7 m/s. The high velocity of these neutrons are used in the generation of a fissile isotope of plutonium (^{239}Pu) from non-fissile uranium isotope (^{238}U) in Fast Breeder Reactor.

1.3. Thermal Energy Production in Reactor

To analytically calculate the actual thermal energy produced by a reactor fuel, there are some factors needed to be assumed. Consider the volume of reactor fuel is V ; assuming that the fuel distribution is homogeneous; the average neutron flux is ϕ_m ; the number density is n and the fission cross-section is σ_f . The average number of nuclear fission reaction taking place per unit volume per unit time is [1]

$$N_f = n\sigma_f\phi_m = \Sigma_f\phi_m \quad (1.11)$$

Where, Σ_f is the macroscopic fission cross-section (1/m)

Assuming that the reactor is working at full power and as mentioned in section 1.2, thermal energy produced per nuclear fission is about 200 MeV, then thermal energy produced in the reactor fuel is

$$Q_r = 200V_r N_f \quad (1.12)$$

$$Q_r = 3.20 \times 10^{-11} V_r N_f \quad (1.13)$$

Assuming that the whole mass of the fissile material in the reactor fuel is M_f , then the number density can be shown by [1]:

$$n = \frac{M_f N_A}{F_r V_r} \quad (1.14)$$

Where, N_A is Avogadro's number ($N_A = 6.022 \times 10^{23}$ [1/mol]) and F_r is the number of fissile atoms per unit mole of nuclear fuel.

From Eq. 1.13 & 1.11,

$$Q_r = 3.20 \times 10^{-11} V_r n \sigma_f \phi_m \quad (1.15)$$

Now from Eq. 1.14 & 1.15,

$$Q_r = 3.20 \times 10^{-11} V_r \left(\frac{M_f N_A}{F_r V_r} \right) \sigma_f \phi_m \quad (1.16)$$

Therefore, the thermal energy generated per unit kg of nuclear fuel is

$$q_r = 3.20 \times 10^{-11} \frac{N_A}{F_r} \sigma_f \phi_m \quad (1.17)$$

And from using Eq. 1.16, the thermal energy generated per unit volume of nuclear fuel is,

$$q' = 3.20 \times 10^{-11} \frac{M_f N_A}{F_r V_r} \sigma_f \phi_m \quad (1.18)$$

Considering that the nuclear reactor consists of N_{rod} number of fuel rods and the heat transfer area of a single rod is A_{rod} , the volume of a single rod is V_{rod} & the length of a single rod is L_{rod} . Then,

The Thermal power density of the nuclear reactor is,

$$Q_{den} = \frac{Q_r}{N_{rod}V_{rod}} \quad (1.19)$$

The Heat flux at the fuel surface of the fuel rod is,

$$Q_{flux} = \frac{Q_r}{N_{rod}A_{rod}} \quad (1.20)$$

The Linear power density of the nuclear reactor is,

$$Q_{lin} = \frac{Q_r}{N_{rod}L_{rod}} \quad (1.21)$$

These, expression of various form of thermal power density are all average values [1].

The consumption of U-235 depends upon the number of neutrons absorbed in the reactor core. Therefore, the number of nuclei absorption taking place is

$$N_a = n\sigma_a\phi_m = \Sigma_a\phi_m \quad (1.22)$$

Where, N_a is the absorbed number of nuclei per second per unit volume; σ_a is absorption cross-section and Σ_a is the macroscopic capture cross-section.

Therefore, the number of nuclei absorbed per second (g) is

$$g = V_r N_a = V_r \Sigma_a \phi_m \quad (1.23)$$

Assuming that the mass of 1 mol of U-235 nuclei is 235 g, then the mass of 1 nucleus

is $\frac{235 \times 10^{-3}}{6.022 \times 10^{23}} = 3.37 \times 10^{-20} \text{ kg}$.

Hence, the consumption of U-235 is (G) [1],

$$G = 3.37 \times 10^{-20} V_r \Sigma_a \phi_m \quad (1.24)$$

1.4. Nuclear Reactors

The power generation from all type of nuclear reactors follow the same basic principles. Thermal energy is generated in the reactor core by a controlled fission chain reaction, that thermal energy in the core is transferred to the primary coolant which subsequently is transferred to the secondary coolant via Intermediate Heat Exchanger (IHX) [3]. The energy of the secondary coolant is extracted and is used for the generation of superheated steam to run the steam cycle to generate electricity.

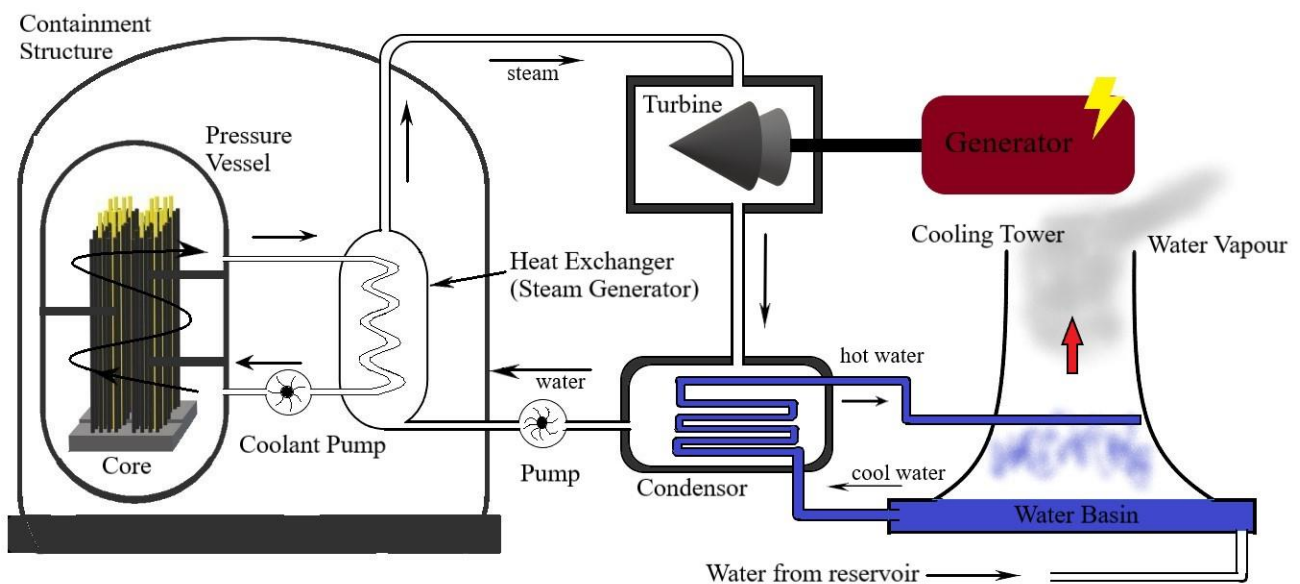


Fig. 1.2 Schematic representation of general Nuclear Reactor

The fission reactions occur at the reactor core and it consists of various components which are design to fulfil each specific task as shown in Fig. 1.2.

- Nuclear Fuel: A fissile isotope of a radioactive element is the obvious choice for nuclear fuel such as U-235 or Pu-239.

- Fuel Cladding: Nuclear fuel is usually in pellet form, size of which varies, is held and contained in the fuel cladding. Zirconium alloys or stainless steel is used as the cladding material in most of the commercial reactors as shown in Fig. 1.4.
- Fuel Assembly: The fuel pellets are stacked inside a fuel rod which is held by cladding material as mentioned above. Several fuel rods are grouped in various shapes namely, rectangular, hexagonal or circular designs to form fuel assembly as shown in Fig. 1.3.
- Moderator: Only thermal reactors used moderator material, which converts the kinetic energy of fast neutrons to thermal energy during the chain reaction. Moderator is not required in fast breeder reactor since fast neutrons are used to convert non-fissile U-238 to U-239.
- Control Rods: For maintaining the chain reaction, controls rods are required, which absorb the extra released neutrons to maintain the critical condition of the fission reaction. Neutron absorbing material is used for control rods like boric acid, boron, graphite, heavy water etc.

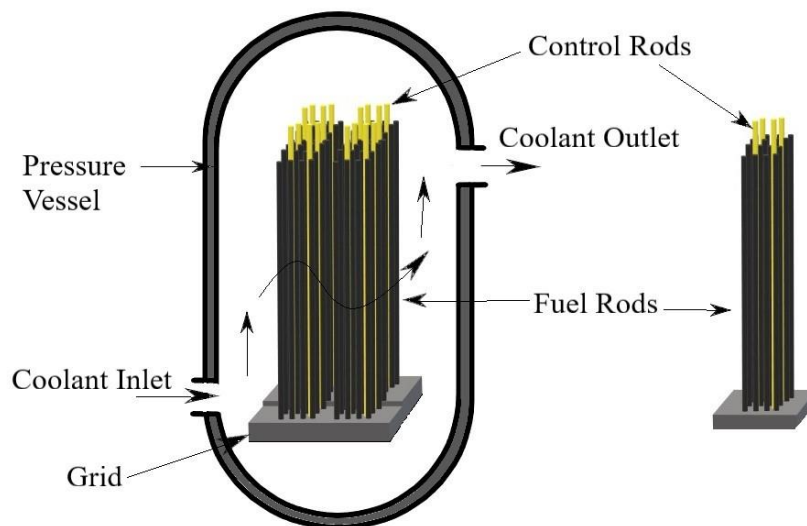


Fig. 1.3 A typical Reactor Fuel Assembly

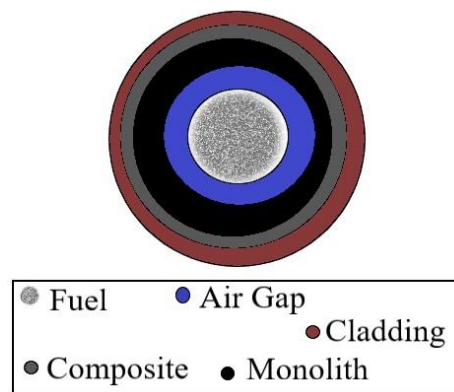


Fig. 1.4 A standard Fuel Rod

The reactor vessel and the heat exchangers designed are made up of 316L stainless steel. 316L is an austenitic steel which is more resistant to corrosion at high temperatures without compromising the tensile and creep strength. Reactor coolant is another vital part of a nuclear reactor, because of the enormous thermal energy dissipation during the normal operating condition. Coolant is used to transfer heat from the reactor core to the steam generator via different methods depending on the type of reactor. However, fluid has to have specific qualities so as to work as a nuclear reactor coolant.

Favourable Reactor Coolant Properties:

1. *High Thermal conductivity (k):* Thermal conductivity of the coolant should be high so that the temperature difference between the coolant flowing and the cladding surface is sufficiently high, otherwise the cladding could fail.
2. *High Specific Heat Capacity (c_p):* High specific heat in turns reduce the total mass flow rate of the coolant which subsequently reduces the cost of the coolant and pumping power.
3. *High Thermal diffusivity (α):* Thermal diffusivity governs the overall heat carrying capacity of a flowing fluid, it should be sufficiently high so that the thermal energy from the reactor core is extracted at a higher rate.
4. *Low Pumping Power:* Fluid having low viscosity can be a good reactor coolant since pumping power is directly proportional to the viscosity of the fluid. Hewitt & Collier [4] proposed a property derived from other fluid properties called the “Figure of Merit F” which is

$$F = \frac{c_p^{2.8} \rho^2}{\mu^{0.2}} \quad (1.25)$$

Where, ρ is the density of the fluid and μ is the dynamic viscosity of the fluid. The Figure of Merit F along with other properties are shown in Table 1.1 for various coolant used in nuclear reactors.

5. *Neutron Capture*: Coolant should have low neutron capture. A single neutron is required for controlled chain fission reaction, if the coolant accidentally absorbs a neutron, the chain reaction might get disturbed.
6. *Physical and Chemical Compatibility*: Coolant should not corrode the reactor container or the cladding, therefore it should be inert to 316 Stainless steel (steel used in nuclear reactors) and Zirconium alloys (cladding material).
7. *High operating Temperature*: Boiling point of the coolant should be sufficiently high so that it can operate in a single phase during the normal or abnormal operating conditions.
8. *Costing and Feasibility*: Coolant should be easily accessible at the nuclear power plant facility.

Table 1.1 Thermophysical properties of various coolants

Coolant	Working Temp. (K)	Pressure (Bar)	Viscosity $\times 10^4$ (kg/m.s)	Specific Heat (KJ/kg.K)	Density (Kg/m ³)	F Figure of Merit
Sodium	823	1	2.30	1.26	817	1
Carbon Dioxide	723	40	0.30	1.2	29.5	1.07×10^{-3}
Helium	723	40	0.36	5.2	3.08	1.1×10^{-3}
Water	543	70	0.98	5.09	770	52.5
	543	155	1.00	4.93	782	49.3
Heavy Water	543	60	1.13	5.27	817	63.4

Table 1.2 Nuclear Reactors categorized by countries, capacity, coolant, moderator and neutron spectrum [48], [3].

Type of Reactor	Country	No.	GWe	Fuel	Coolant	Moderator	Neutron Flux Spectrum
Pressurized Water Reactor (PWR)	USA, France, Japan, Russia, China, South Korea	299	283	Enriched UO ₂	Water	Water	Thermal
Light Water Graphite Reactor (LWGR)	Russia	13	9	Enriched UO ₂	Water	Graphite	
Pressurized Heavy Water Reactor (PHWR)	Canada, India	48	24	Natural UO ₂	Heavy Water	Heavy Water	
Boiling Water Reactor (BWR)	USA, Sweden, Japan	65	65	Enriched UO ₂	Water	Water	
Gas Cooled Reactor (AGR)	UK	14	8	Natural or Enriched UO ₂	CO ₂	Graphite	
Liquid Metal Fast Breeder Reactor (LMFBR)	Russia	2	1.4	PuO ₂ and UO ₂	Liquid Sodium	-	Fast
Total		441	390				

1.5. Liquid Metal Fast Breeder Reactors

The Liquid Metal Fast Breeder Reactor (LMFBR) also referred as Liquid Metal Cooled Reactor (LMCR) is a fast neutron reactor in which the fast neutrons are not thermalized by the moderator, hence there is no moderator in the reactor design. LMFBR rely on fast neutron for the fission reaction, considering natural uranium (0.7% U-235 & 99.3% U-238), the natural uranium going through fission reaction releases fast neutrons which are absorbed by the non-fissile U-238 isotope of uranium converting it to short-lived U-239 isotope. This U-239 isotope undergoes two levels of β decays to produces Pu-239, which is a highly fissile isotope of plutonium. Therefore, they are named *Breeder Reactor*, as it breeds a new fissile element during

the fission reaction. LMFBR has liquid metal coolants such as sodium (Na), potassium (K), sodium-potassium alloy (NaK), lead (Pb) and lead-bismuth eutectic alloy (LBE).

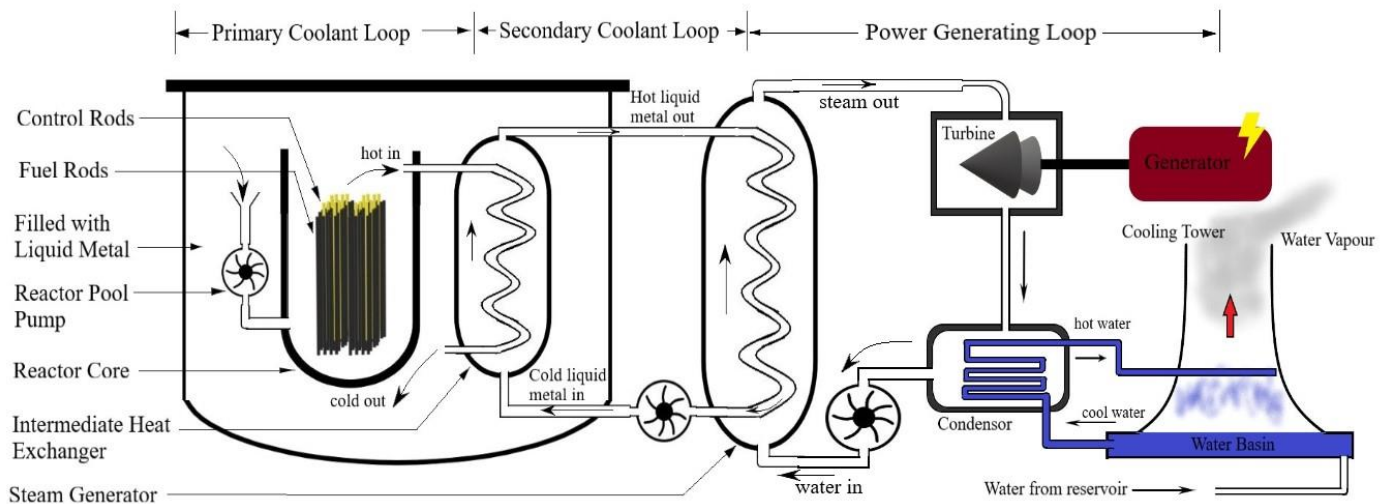
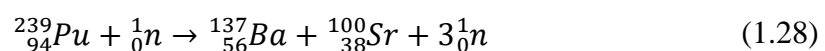
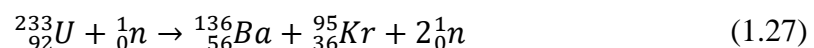
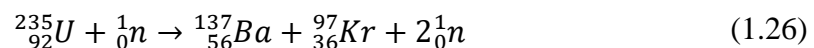


Fig. 1.5 Schematic representation of the LMFBR

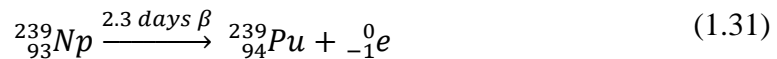
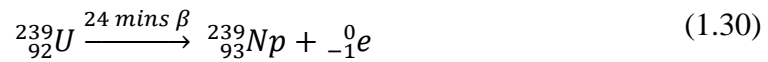
A general LMFBR design is shown in Fig. 1.5. There are two liquid metal (LM) circuits first, is called the primary cooling circuit which directly cools the reactor core and second is called the secondary cooling circuit. The primary liquid metal and secondary liquid metal pass through the IHX, primary LM extracts heat from the reactor core at around 600°C and transfers it to secondary LM, which enters the IHX at around 350°C. The secondary LM is used as the thermal energy source for steam generator circuit which generates power.

Controlled fission reactions in LMFBR are similar as those in PWR, BWR etc. [1]



Maintaining the fission reaction is highly crucial in the LMFBR since average energy of a fast neutron is around 1 MeV by fission of U-235 and Pu-239. Moreover, the fission must provide extra fast neutrons for “breeding” of Pu-239 from U-238.

The breeding of Pu-239 from U-238 follows two levels of β decays.



From the Eq. 1.26 – 1.28, it can be observed that there is 2 to 3 number of neutrons emitted during the fission reaction. Let us say that on an average ν number of neutrons are emitted per nuclear fission and η number of neutrons are emitted per unit neutron absorbed in the reactor (not necessarily for continuing the chain reaction), η is called the *Fission Factor*. The factors η & ν are important parameters for LMFBR, as they control the *Breeding Ratio*. Breeding ratio (k_{breed}) is the ratio of the amount of Pu-239 produced during fission and the amount of U-238 depleted.

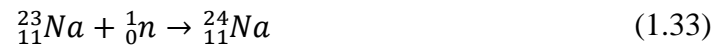
$$k_{breed} = \frac{\text{mass} ({}^{239}_{94}\text{Pu})}{\text{mass} ({}^{238}_{92}\text{U})} \quad (1.32)$$

Table 1.3 Breeding Ratios values and respective type of reactors

$k_{breed} > 1$	Breeder Reactor
$k_{breed} = 1$	Iso-Breeder Reactor
$k_{breed} < 1$	Depleting Reactor

The liquid metals used in the cooling systems are highly susceptible to radioactivity hence, radiation shielding is required between the primary coolant and secondary coolant in the intermediate heat exchanger.

The non-fission reaction of Liq. Na occurs when the primary coolant is flowing over the reactor core,



Where the Na-24 isotope of sodium is highly radioactive which emits 2.75 MeV of gamma (γ) radiations along with 1.3 MeV of beta (β) radiations. The Liq. Na in the primary circuit which comes in direct contact with the reactor core gets converted into a radioactive isotope of sodium which emits huge amounts of radiation, therefore the need of secondary coolant loop is essential. The primary and secondary coolant loop (both having LM) exchange heat through the IHX, which has to be heavily shielded for radiation.

1.5.1. Loop Design

The loop design of LMFBR has the reactor core is in 316L type stainless steel (SS) vessel which has LM flowing through it. The reactor core is vertically aligned and the LM is made to flow axially to get maximum contact surface area for heat transfer from the fuel assembly to the LM. The primary LM is flown by a pressure pump situated outside the reactor vessel or the flow is natural circulation created by the density variation. The inlet temperature of the primary LM is around 600°C and exit temperature is around 350°C. Forced convection is more convenient in the case of LM because of high thermal diffusivity & low viscosity so that they carry heat much quicker than normal non-metallic fluids. The secondary loop (intermediate loop) having the IHX and the steam generator (SG) also has LM as the coolant. The secondary LM enters the IHX at around 250°C and exits at around 500°C, the actual values of the temperature are subjected to design and load capacity of the fuel cycle [3]. The thermal energy absorbed by the secondary LM is utilized in the SG for generating superheated steam for power generating loop working on Rankine cycle. The schematic diagram of Loop design of LMCR is shown in Fig. 1.6.

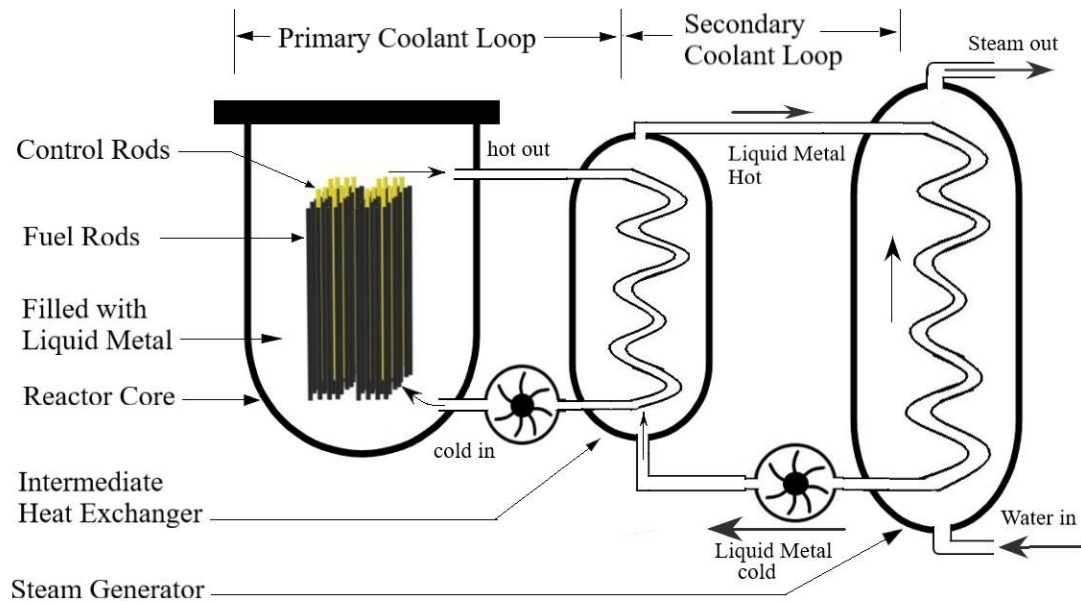


Fig. 1.6 Loop Design of the LMFBR

1.5.2. Pool Design

The Pool design also uses the 316L SS as the material for the reactor vessel, this particular alloy is used because it is compatible with liquid metals. In the pool design, the primary coolant loop is situated inside the reactor vessel. The reactor core is submerged in the pool of liquid metal all the time, where the pressure pumps created pressure difference for LM to flow inside the reactor vessel in circulation. The IHX is also situated inside the reactor vessel, where the secondary coolant LM and the primary coolant LM exchange heat whilst submerged in the LM pool. The secondary loop (intermediate loop) is situated outside the reactor vessel where the thermal energy in the secondary LM is utilized in generating steam through the SG for power generating loop. The schematic diagram of the pool type design is shown in Fig. 1.7.

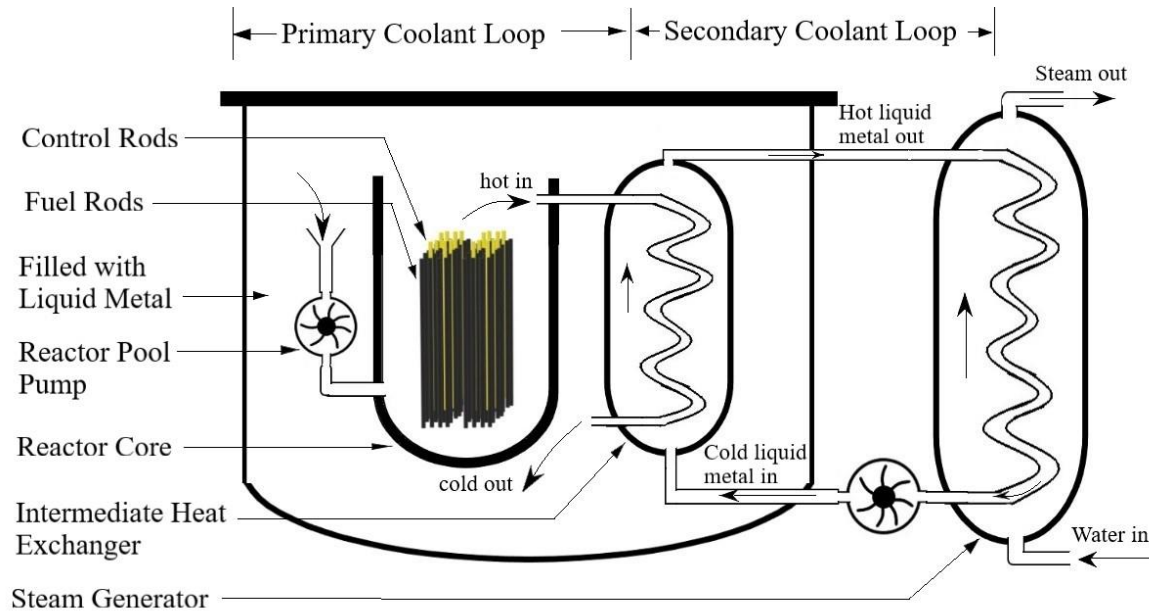


Fig. 1.7 Pool design of the LMFBR

1.5.3. Liquid Metal Coolants

Liquid metals coolants are unlike other fluids generally used as coolants, the thermophysical properties of liquid metal are fundamentally different from non-metallic fluids. The properties of LM are highly sensitive towards the temperature change, in other words, the thermophysical properties are functions of temperature. The use of liquid metal coolants come with advantages and also with drawbacks, in the upcoming section a general comparison of Liq. Na and LBE are given.

I. Advantages

- The liquid metals exist in the liquid phase at high temperatures ($300^{\circ}\text{C}\sim 500^{\circ}\text{C}$), the high working temperatures of operation increase the thermal efficiency of the whole system, therefore the use of liquid metals are beneficial in LMCR.
- The liquid metals have a high boiling point (T_{boil}), Liq. Na has $T_{boil} = 850^{\circ}\text{C}$ & LBE has $T_{boil} = 1750^{\circ}\text{C}$, which is sufficiently higher than the working temperatures. Therefore, the issue of phase change does not exist in the case of liquid metals.
- The high boiling point for both Liq. Na & LBE prevents the situation of core voiding which eventually leads to cladding failure.

- The sufficient margin between operating temperature and boiling point also eliminates the requirement of pressurization as done in PWR.
- Liquid metals have low neutron absorption characteristics which makes them perfect for the use of coolant.
- Liquid metals have very high thermal conductivity (k) which enhances the conduction heat transfer.
- Liquid metals have high thermal diffusivity (α) which enhances the rate with which it can carry thermal energy during fluid flow.
- Liq. Sodium has moderate density $\rho \approx 900 \text{ kg/m}^3$ in contrast to LBE which has $\rho \approx 11000 \text{ kg/m}^3$, substantially decreasing the required pumping power for the same pressure drop.
- LBE has self-shielding properties i.e. it absorbs γ radiations [2].

II. Drawbacks

- The high operating temperatures may induce corrosion however, recent developments in material sciences have limited chemical corrosion between the liquid metals and stainless steel such as the 316L steel.
- Liquid metals are opaque therefore making it impossible for engineers to have a visible inspection during general maintenance. Therefore, special inspection tools are needed for such tasks.
- During shutdowns, the liquid metals are required to be heated at all times for maintaining their liquid phase.
- LBE has a very high density in contrast to Liq. Na, therefore for equal mass flow ratio, LBE requires substantially high pumping power.
- LBE is radiation-absorbing but during its irradiation, it creates extremely lethal Polonium, therefore it has to be confined at all times.
- Liq. Na when comes in contact with reactor core absorbs emitted neutron for conversion to Na-24, which is a highly radioactive isotope of sodium hence, special radiation shielding is required in the primary coolant loop and the IHX.

1.6. Thesis Objective

The objective of this thesis is to analyze the heat transfer and fluid flow characteristics of Liq. sodium and LBE for turbulent flow in a double-pipe heat exchanger which is designed to be used as an Intermediate heat exchanger in liquid metal cooled nuclear reactor. The inlet boundary conditions of hot fluid (liquid metal) and the inlet condition of the cold fluid (glycerol) was varied in order to understand the effect of change of inlet temperature, inlet velocity, and length of the heat exchanger on thermal hydraulic characteristics namely, the rate of heat transfer, the pressure drop, the logarithmic temperature difference, and the overall heat transfer coefficient of the IHX.

1. Initially, geometrical models of the IHX were prepared in Solidworks software, and then were imported to Ansys Fluent software. The Ansys Fluent is used for heat transfer and fluid flow simulation of the heat exchanger for a various number of cases.
2. The outputs of the simulations are represented in the form of temperature contours, density variation contours, and plots representing the variation of thermal performance parameters with respect to the variation in inlet conditions.
3. Non-linear regression analysis is performed using a correlation which is developed by the author, it shows the overall heat transfer coefficient as the function of independent input variables.
4. Artificial neural network (ANN) algorithm is used for predicting the overall heat transfer coefficient and then comparing the predicted values with the CFD results in order to check the feasibility of using ANN as regression tool for heat exchangers.
5. Conclusions are drawn on the results from the plots and the regression analysis performed in this thesis.

Chapter 2 – Literature Survey

This chapter focuses on the previous research & studies done in the field of liquid metal heat transfer, converging towards the use of liquid metals in the cooling mechanism of nuclear reactors and the analysis of the various type of heat exchangers with liquid metals as their working fluid. Initiating with the studies and experiments done for understanding the flow physics of liquid metals and then carrying those researches to the mechanisms of convection heat transfer. Then, the survey turns to the practical applications of liquid metal in the nuclear reactors with experimentation and analysis results. With the development of computational methods for solving energy & momentum equations, the research diverted from the expensive experiments towards computational techniques like CFD for fluid flow and heat transfer analysis. The survey also follows the interdisciplinary sciences like Optimization Technique (OT) & Artificial Neural Network (ANN) required for studying the behaviour of characteristics and the changes in the outputs with respect to the variations in input parameters.

2. LITERATURE SURVEY

Lyon [64] conducted several experiments to analyze the fluid flow and heat transfer characteristics on a fully developed turbulent flow of Liq. Sodium in a tube with an isothermal wall. The experiment involved the variation of diameter and length of the tube to alter the length to diameter ratio and the inlet velocity of the liquid metal was also varied. An empirical correlation was developed in the results which shows avg. Nusselt number as a function of Peclet number of liquid metals.

Ibragimov et al. [5] studied the variation of the convective heat transfer coefficient in terms of avg. Nusselt number with the variations in the temperature difference & the inlet velocity of liquid metal. The tube was vertically aligned with liquid metal flowing against the gravity therefore, the buoyancy effects were in play. The liquid metals considered in the study were mercury, lead and LBE. The variation of the Nusselt number with Peclet number was observed and plotted for comparisons with correlation developed by [64] and other previous studies.

Dwyer et al. [6] evaluated the effects of dimensionless quantity ψ which is the ratio of eddy diffusivity of heat transfer and eddy diffusivity of momentum on the avg. Nusselt number for fully developed turbulent flow in an isothermal pipe with different liquid metals. The plots of Nusselt number vs Peclet number were analyzed and commented upon for different arrangements of tubes and rod bundles. Several experimental data were evaluated and analyzed for different values of ψ and new correlations for evaluating the Nusselt number for a different type of cross-sectional flow were

developed for constant heat flux conditions & these correlations were compared with previously conducted studies [64, 50].

Holtz [7] conducted an experimental analysis for a fully developed flow of Liq. NaK in vertically aligned stainless steel tubes, the liquid metal is made to flow through the pipe against the gravity by electromagnetic (EM) pump. The heat transfer results for constant heat flux at the tube wall were compared with results of [64] & [6] which showed high agreement.

Stein [8] explained the fundamentals of heat transfer in liquid metals while solving the energy and the momentum equations for liquid metals flowing tube and annulus region. In this chapter, several key factors like the thermophysical properties, Prandtl number, and turbulent flow was analyzed and commented upon. The flow physics and heat transfer principles were elaborated and the formation of Nusselt number as a function of Reynolds number and Prandtl number was explained.

Rust [9] conducted a parametric analysis of Lyon's correlation [64

] for analyzing the effects of flow velocity, eddy diffusivity for momentum & eddy diffusivity ratios on the Nusselt number calculated by the correlation. The results showed that the Nusselt number is insensitive by variation of the velocity profile of the liquid metal. The variation in eddy diffusivity ratio highly alters the overall Nusselt number for low flow rate however, the effect decreases as the flow rate increases.

Minkowycz & Stein [10] analyzed previously conducted studies of forced convection heat transfer of liquid metal in the turbulent region on circular tubes, parallel plates, annular regions & rod bundles for different Reynolds number. A new correlation was developed for each orientation which showed significant improvement over the already established correlations [64], [5], [7].

Nijsing & Eifler [11] developed a computational method for thermal-hydraulic analysis of Liq. Sodium cooled rod bundles and subassemblies in LMFBR. Transient heat transfer analysis was performed for cooling of triangular spaced rod bundles. The Liq. Na has axial flow along the rods and the velocity inlet was considered to be decreasing with time. An equation was developed for overall heat flux which was exponential in nature showed that the rate of heat transfer was decreasing with time and temperature profiles of heat-generating rod bundles were computed.

Kays [12] examined the experimental data on heat transfer of liquid metals in the turbulent flow region. He corroborated the physical significance of turbulent Prandtl number in the calculation of heat transfer coefficient for liquid metals. Analytical solutions, as well as the computational methods like RANS & DNS techniques were utilized in solving heat transfer equations in thermal boundary layer for liquid metals, water and air, which showed remarkable agreement with experimental results. Plots for turbulent Prandtl number versus turbulent Peclet number were plotted to observe the behaviour of the relation between the two values.

The research in the field of nuclear reactors took a sour turn after a few major accidents occurred in the 1970s and 80s. The accident on Three Mile Island reactor in Pennsylvania, USA and the worst nuclear accident in the history of mankind, the reactor explosion in Chernobyl, Russia. Till this date, Chernobyl is inhabitable and it will remain inhabitable for the next 10,000 years because of radiation leakage. The scientific community and the research investors established that the nuclear reactor technology is extremely lethal for working hence, there was an unprecedented gap in research from the 1980s to late 90s. However, with significant advanced in the field of material sciences and nuclear engineering, the research resumed with even more pace with involvement of safety regulatory councils like IAEA & NRC for ensuring proper safety guidelines.

Raghupathy et al. [13] proposed the design of a Prototype Fast Breeder Reactor (PFBR) with pool type sodium cooling system working on multiple oxides of fissile Uranium (MOX). The project was proposed by IGCAR for the government of India with an electric capacity of 500 MW. This reactor plant is under construction as of now and expected to be completed in 2022.

Cheng et al. [14] investigated the thermal hydraulic analysis of Liq. sodium in subchannels of reactor core using computational methods. Two types of subchannels were considered for analysis: Triangular & Square. The $k - \epsilon$ & SST models were used to solve the governing equations and the heat transfer outputs were compared with the experimental results. It was concluded that linear turbulence model over-predicted the heat flux values and non-linear turbulence model showed high accuracy with experimental data.

Khan et al. [15] studied the heat transfer phenomenon of liquid metals flowing across a heated cylinder, an analytical approach was applied to solve the governing equations. Two types of boundary conditions were applied, constant temperature and constant heat flux at the cylinder wall. The influence of the hydrodynamic boundary layer on heat transfer was analyzed for various Reynolds number. The Nusselt number versus angular displacement variation was observed for analytical and experimental data moreover, inviscid and viscous fluid flow was compared for same boundary conditions.

Mathews et al. [16] analyzed the functional reliability of the safety grade decay heat removal system (SGDRS) of the Indian PFBR. The SGDRS has primary sodium circuit which has 4 sodium to sodium IHX, the secondary cooling system which has sodium to air heat exchanger (AHX) and tertiary cooling system which has air as the working fluid. An in-house developed 1D code DHDYN (developed by the IGCAR) and the Monte-Carlo method is utilized for analysing the functional failure probability of the SGDRS and the responses were indicated in the results.

Deng et al. [17] argued that liquid metal is also capable of being used in the electronics industry as a coolant. They fabricated two types of sodium to air HX where the liquid sodium extracts heat from the CPU which is generating 10^6 W/m^2 heat flux and is transferred to air via a small HX. An Electromagnetic pump was used to create pressure difference for the Liq. sodium to flow and the design principles were discussed. Gallium-Indium-Tin alloy is used as the liquid metal. The heat transfer characteristics were discussed and compared with other heat extracting devices.

Guo et al. [18] used CFD techniques to study and analyze the heat transfer characteristics of LBE in the turbulent flow region flowing in a straight tube. The diameter of the tube was 10 mm and the length was 1 m . The inlet velocity of LBE was varied from 1 m/s to 3.5 m/s and the inlet temperature was taken as constant at 723.15 K with the tube wall being subjected to an average heat flux of $5 \times 10^5 \text{ W/m}^2$. The variation of thermophysical properties of LBE with temperature was presented. The $k - \epsilon$ model was used to solve the momentum, continuity and energy equations. The variation of pressure drop and the Nusselt number for varying inlet condition was observed and the results were compared with the experimental results of Ma et al. [19]. The variation of turbulent Prandtl number with increasing

Peclet number and the variation in the rate of heat transfer with increasing Peclet number was analyzed and the findings were also presented in form of plots.

Chen et al. [20] designed and analyzed a shell and tube type HX with LBE flowing in the tube and Helium gas in the shell side. 3 dimensional CFD analysis was performed using the $k - \epsilon$ model with scalable wall function which limits the y-plus (y^+) value at 11.06. The inlet boundary conditions were varied, such as the inlet temperature and inlet flow rate of LBE, to observe its effects on overall heat transfer coefficients (HTC). The HTC values computed from simulations were compared with analytical solutions. The pressure drop variation with increasing Reynolds number of LBE was also plotted and compared with Colebrook's correlation of pressure drop during turbulent flow. The $\epsilon - NTU$ analysis was compared with the effectiveness computed from the simulations which showed remarkable accuracies. Moreover, a new form of effectiveness was developed to assess the performance of the HX for different inlet conditions.

Pacio et al. [21] conducted heat transfer experiments using LBE and Liq. lead as the coolants on hexagonally shaped rods with triangular spaced sub-assembly. An array of 19-rod bundles was designed and fabricated for the experiment. The heat sources and the flow rate of liquid metals were varied to analyze the variation in the pressure drop and the heat transfer coefficient. The pressure loss coefficient was analyzed for different ratios of grid length to grid space for increasing Reynolds number of LM. The empirical relations and experimental calculation showed good agreement of Nusselt number for different Peclet number.

Pacio et al. [22] extensively researched on the developed correlations for predicting the Nusselt number based on Peclet number for turbulent flow in pipes. A summary and comparison of 21 experiments were discussed, which in total had about 1100 data points with 15 correlations showing Nusselt number as a function of Peclet number for different liquid metals. The study included observations of heat transfer characteristics of LBE, Liq. Na, Liq. NaK, Liq. Pb, and Liq. Hg. Out of the 21 correlations, some recommendations were made for future research purposes.

Taler [23] conducted the study for comparing the correlations developed for predicting the turbulent Prandtl number with the two new models developed. The new models

and the existing correlations derived by [56] were compared by plotting turbulent Prandtl number versus Reynolds number graphs. The study concluded by discussing new correlations which predicted the avg. Nusselt number for turbulent pipe flow with reasonable accuracy with the correlations developed by [56, 60, [24] .

Jaeger [25] conducted this study which reviews the HT performances of most the liquid metal used in nuclear reactors, namely LBE, Liq. Na, Liq. K, Liq. NaK, Liq. Pb & Liq. Hg. Detailed representation of the thermophysical properties of all the above-mentioned liquid metals was made in the study since all of the liquid metals are non-Newtonian fluids. The study included comparisons of correlations developed for predicting Nusselt number for various liquid metals for various geometries, namely circular pipe, annular channel, rod bundle, rectangular cross-section flow, & parallel plate flow.

Hata et al. [26] investigated the heat transfer characteristics of Liq. sodium for turbulent flow in a circular tube and concentric annulus region by numerical simulations. The hydraulic diameter of the circular tube and annulus region was kept equal for a proper parametric comparison. The diameter of the tube was $d = 6.7 \text{ mm}$ and the inner & outer diameters of annulus regions were $d_i = 7.6 \text{ mm}$ & $d_o = 14.3 \text{ mm}$. The inlet temperature of Liq. sodium was varied from $573 - 585 \text{ K}$ with inlet velocity being varied from $0.085 - 1 \text{ m/s}$. The walls of both types of ducts were given constant heat flux boundary conditions with $5 \times 10^5 \text{ W/m}^2$. The variation of Nusselt number along the length of the tube was observed for the variety of combination of cases and a correlation was developed for circular tube and concentric annulus region which was compared with previous correlations developed by [60, 61] and it was concluded that for same hydraulic diameter the Nusselt number for circular tubes was 32.14% lower than for concentric annulus region.

Unger et al. [27] studied the application of forced convection heat transfer from spent fuel rod bundles which are cooled via airflow. A CFD analysis was performed for rod bundles having different orientations and shapes for various temperature difference between the spent fuel rods and free stream temperature of the air. Ansys CFX was used for design and analysis. The number of rods, aspect ratio of fuel rods and their orientation was optimized after observing the effects of these parameters on the rate of heat transfer. It was concluded that staggered arrangement gives a higher rate of heat

transfer and the optimum number of fuel rods is 5, and the addition of any more rods had insignificant effect on the rate of heat transfer.

Mochizuki & Takano [28] discussed the heat transfer and performance of IHX and Air-cooled HX (AHX) used in MONJU, JOYO & 50 MW-SG (steam generator experimental plant). The heat transfer characteristic of IHX which is a shell and tube type HX was elaborated & compared for the three mentioned systems. The inlet temperature of primary Liq. sodium (shell side) is 400°C and secondary Liq. sodium is 300°C with a flow rate of primary Na being constant at 34.7 *kg/s* for natural circulation and 36.6 *kg/s* for forced circulation system. The secondary Liq. sodium (tube side) after extracting the heat from the primary side with increased temperatures is cooled by the AHX. The AHXs are usually used in the secondary cooling system of FBRs, where the residual thermal energy from the liquid metals is removed. AHX of these systems are annular finned-tube type heat exchangers with the diameter of tubes ($d = 50.8\text{mm}$), the diameter of annular fins ($d_f = 82.8\text{mm}$) having the number of tubes to 62 & 15 for MONJU and 50 MW-SG respectively. The inlet temperature of Liq. sodium in AHX is 500°C, which is cooled to 325°C by forced convection for MONJU. The experimental heat transfer data from several combinations of inlet variables is used to validate the results calculated using the NETFLOW code which showed exceptional agreement.

Mochizuki [29] investigated the analysis of IHX employed in MONJU, JOYO and 50 MW-SG facility as discussed in [28]. In this study the main focus was on the thermal performance of the IHX used in the three facilities, the specifications of IHX of JOYO, MONJU & 50 MW-SG is given in Table 2.1. The inlet conditions were varied to observe the effect on Nusselt number of the Liq. sodium used. Transient numerical solutions were conducted with the NETFLOW++ code and were compared with the experimental results for IHX moreover, correlations were developed for Nusselt number as a function of Peclet number. The developed correlations were compared with correlations developed by [30] & [60], the developed correlations showed accuracy for low Peclet number. Conduction heat transfer which is significant for low flow rate conditions (such as natural circulations) was also analyzed in this study which was significant in comparison to convection heat transfer.

Table 2.1 Specification of IHX in JOYO, MONJU & 50 MW-SG (flow rate conditions is specific for [28])

Parameters	JOYO	MONJU	50 MW-SG
Total Heat Transfer (<i>MW</i>)	70	238	50
Number of Tubes	2088	3294	2044
Outer Diameter of Tubes (<i>mm</i>)	19	21.7	15.9
Thickness of Tube (<i>mm</i>)	1	1.2	1.2
Mass flow rate – Secondary side (<i>kg/s</i>)	329	1038	222
Inner-shell Outer Diameter (<i>mm</i>)	532	746	457
Inner-shell Thickness (<i>mm</i>)	11.5	20	14.3
Outer-shell Outer Diameter (<i>mm</i>)	1872	2184	1560
Outer-shell Thickness (<i>mm</i>)	16	25	25
Mass flow rate – Primary side (<i>kg/s</i>)	370	1422	263
Total Effective Heat Transfer Length (<i>m</i>)	2.93	4.86	3.90

Mochizuki [31] conducted a similar study as conducted in [29] however, in this study IHX of only MONJU and 50 MW-SG were only under consideration. The input conditions of primary and secondary side Liq. sodium was varied to analyze its effect on Peclet number, Prandtl number & Nusselt number. The Nusselt number variation was observed along with the height of IHX for both the cases. The experimental results were compared with the results of studies [30] & [50] and it showed good agreement for low flow rate conditions.

Mochizuki [32] performed a numerical analysis of the IHX of MONJU, in this study the IHX was designed and divided into three parts. These three parts were separately designed & solved using Ansys CFX with variable inlet boundary conditions.

1. Model - I: the upper plena with inlet nozzles and top part of the tubes.
2. Model - II: the centre pipe with lower plena
3. Model - III: heat transfer tubes

The standard $k - \varepsilon$ model with scalable wall function & 2nd order upwind was used and the thermophysical properties of Liq. sodium were input with polynomial

approximation instead of actual functions, few of the conditions were estimated by analytical calculations. The solutions from the three models were compiled and presented in form of plots. The Nusselt number for Liq. sodium was compared with the one-dimensional NETFLOW++ code and the experimental results of [28] & [29].

Mochizuki [33] analyzed the behaviour of the Nusselt number of LBE for turbulent flow in a circular tube and compared with the experimental results of [50] for low Peclet number condition. The outer diameter of the tube was 0.75 *in* and the inner diameter of tube was 0.625 *in* with the total length of 4 *ft*. For the study low Peclet number is considered since the result data from experiments performed in [29] were overestimated with respect to the correlation presented by [50]. The numerical solution was performed in Ansys Fluent, in which two types of RANS models were used: $k - \epsilon$ model & $k - kl - \omega$ model. The inlet velocity of LBE was varied from 0.13 – 0.37 *m/s* with inlet temperature being varied from 480K to 512 K. The variation of the inlet conditions resulted in 8 types of cases which were solved for both types of RANS models and then compared with the experimental results for the same inlet conditions with great accuracy.

Mochizuki [34] surveyed experimental research done on heat transfer coefficient for turbulent flow in pipes for liquid metals. A variety of experiments were studied such as [24], the schematic representation of the apparatus used for these experiments were elaborated. [34] conducted a similar analysis done in [33] but with different inlet conditions. Experimental results of [64], [50], [54] & [24] were used to validate the CFD analysis done to compute the HTX for LBE turbulent flow in the circular tube.

Ma et al. [19] conducted experimental research on the heat transfer and fluid flow characteristics of LBE in a straight tube HX & U-tube double-pipe HX with the secondary fluid as 100% glycerol. The inlet velocity and the inlet temperature of LBE were varied to understand its effects on the pressure drop and overall rate of heat transfer while keeping other inlet conditions constant. The inner diameter of the tube carrying LBE was 10 *mm* with the thickness of 1.5 *mm* and the inner diameter of the outer pipe was 25 *mm*. The inlet velocity of LBE was varied from 0.5 – 2.5 *m/s*, the inlet temperature of LBE was varied from 200 – 450°C, and also, the inlet temperature and inlet volume flowrate of glycerol was varied from 150 – 180°C and 25 – 115 *l/min* respectively. For fluid flow analysis of LBE, the pressure drops were

measured with respect to changing Reynolds number & represented in form of plots and the friction factor calculated from experimental results was compared with analytical calculations with a satisfactory agreement. The variation of the overall heat transfer coefficient was represented with increasing Reynolds number of LBE. It was concluded that experimental results were in good agreement with the analytical calculations and U-tube HX showed more rate of heat transfer.

The applications of Artificial Intelligence (AI) is growing at a monumental rate; in the fields like genetic engineering, cancer research, facial recognition software, analysis of thermal systems like heat exchangers are all using the AI. Machine Learning (ML) is a subset of AI, it is the field of computer science in which the systems learn for the data available without being explicitly programmed. Deep Learning is a subset of machine learning, it is the domain in which neural networks are used as the learning algorithm.

Diaz et al. [35] performed a heat transfer analysis of a plate-fin heat exchanger using ANN. Initially, the ANN predictions were validated for simple one-dimensional conduction heat transfer and then it was performed for convective heat transfer. The Sigmoid function was used as the activation function for ANN regression analysis. The predicted values were compared with computed values of the total rate of heat transfer for plate-fin HX with 10% error. Along with predictions, various combination of nodes and number of hidden layers were also compared.

Islamoglu [36] conducted an experimental study on wire-on-tube heat exchanger having various inlet boundary conditions and geometrical dimensions. ANN was used to predict the rate of heat transfer for 3 types of HX and the results were plotted against the experimental data. The results showed under 3% error for a single setup of ANN with 1 hidden layer having 5 nodes.

Xie et al. [37] performed experimental heat transfer analysis on 3 different designs of a shell-tube heat exchanger having water and oil as the working fluids with variable inlet boundary conditions and used ANN regression technique for predicting the temperature differences. Backpropagation technique was used in ANN regression analysis where the temperature difference between inlet and outlet conditions for water and oil was predicted. Several combinations of ANN configurations were used to

predict the output and were compared. The results showed predictions with an error less than 10% for both water and oil for 8-6-5-3 configuration. The 8-6-5-3 configuration represents that the input layer has 8 nodes and there are two hidden layers with 6 & 5 nodes respectively and the output layer has 3 nodes.

Tan et al. [38] performed experimental analysis on a compact fin-tube type heat exchanger with aqueous ethylene glycol solution and air as the working fluids. The mass flow rate of air was varied for various inlet temperature of the glycol solution. A multi-layered feed-forward ANN was utilised in this study to perform a regression analysis for predicting heat transfer rate for the same inlet boundary conditions. The predictions of ANN were compared with non-linear regression model which was used to form a correlation. The prediction with both the techniques showed remarkable accuracies with ANN showing better results.

Chapter 3 – Thermal Hydraulics of Liquid Metals

This chapter primarily focuses on the thermophysical properties of liquid metals and their fluid flow physics and heat transfer characteristics. The temperature dependency of thermophysical properties have been explained and its significance on the energy and momentum equations are also commented upon in details. The uniqueness of liquid metals over normal non-metallic coolant has been explained and various types of liquid metals have been considered and compared in this chapter.

3. THERMAL HYDRAULICS OF LIQUID METALS

The fundamental equations that govern the heat transfer and fluid flow principles shown in vector form are [59]:

The continuity equation:

$$\frac{\partial \rho}{\partial t} + \nabla \cdot (\rho \vec{V}) = 0 \quad (3.1)$$

The momentum equation:

$$\frac{\partial(\rho \vec{V})}{\partial t} + \nabla(\rho \vec{V} \cdot \vec{V}) = \rho \vec{g} - \nabla p + \nabla \bar{\tau} + \vec{F} \quad (3.2)$$

The energy equation:

$$\frac{\partial(\rho E)}{\partial t} + \nabla(\rho E \vec{V}) = -\nabla(\vec{V} p) + \nabla(k \nabla T + \bar{\tau} \cdot \vec{V}) + \dot{q} \quad (3.3)$$

The equations of state:

$$p = p(\rho, T) \quad (3.4)$$

$$e = e(\rho, T) \quad (3.5)$$

Where, ρ is the density of the fluid, p is the pressure, T is the temperature, e is the internal thermal energy, \bar{g} is the gravitational acceleration, \dot{q} is heat generation per unit volume, \vec{F} is the external force applied, \vec{V} is the velocity vector given as:

$$\vec{V} = u\hat{i} + v\hat{j} + w\hat{k} \quad (3.6)$$

And E is the total energy of the fluid,

$$E = e + \frac{1}{2}V^2 \quad (3.7)$$

The $\bar{\tau}$ is the stress tensor of fluid represented as:

$$\bar{\tau} = \mu \left(\nabla \vec{V} + \nabla \vec{V}^T - \frac{2}{3} \nabla \vec{V} I \right) \quad (3.8)$$

Where, I is unit tensor.

The momentum equation 3.2 also called the Navier-Stokes Equation (NSE) is a non-linear second-order partial differential equation. At present no developed mathematics can solve these types of equations, however, NSE is linearized by appropriate boundary conditions pertaining to the problem at hand, thus making it solvable. The Eq. 3.1 – 3.3 are mentioned for unsteady flow, we need to appropriate these equations according to our boundary conditions. The analysis in this study is considered to be invariant to change in time i.e. steady-state analysis therefore the Eq. 3.1 – 3.3 will be changed.

The continuity equation becomes:

$$\nabla \cdot (\rho \vec{V}) = 0 \quad (3.9)$$

The momentum equation becomes (without external forces):

$$\nabla(\rho \vec{V} \cdot \vec{V}) = \rho \bar{g} - \nabla p + \nabla \bar{\tau} \quad (3.10)$$

The energy equation becomes (without internal heat generation):

$$\nabla(\rho E \vec{V}) = -\nabla(\vec{V} p) + \nabla(k \nabla T + \bar{\tau} \cdot \vec{V}) \quad (3.11)$$

The solution of these equations is depended upon the thermophysical properties incorporated in the above equations. The liquid metals are classified as non-Newtonian; their properties are not constant during the heat transfer process. The thermophysical properties vary with the flow and the bulk temperature.

For a better understanding of the thermal hydraulic behaviour of different fluids, liquid metals, in this case, the equations are needed to be converted to non-dimensional form. The non-dimensional forms of Eq. 3.9 – 3.11 are highly complicated and not necessary at this level of the study therefore, assuming steady-state, laminar flow & ignoring the viscous dissipation, the simplified forms of Eq. 3.1 – 3.3 are mentioned below along with the non-dimensional forms in Table 3.1.

The equations are normalized into non-dimensional form by defining non-dimensional independent variables [39]. The direction variables are:

$$x^* \equiv \frac{x}{L_c} \quad y^* \equiv \frac{y}{L_c} \quad z^* \equiv \frac{z}{L_c} \quad (3.12)$$

Where, L_c is the characteristic length, the other parameters are as follow:

$$\vec{V}^* \equiv \frac{\vec{V}}{V} \quad (3.13)$$

$$u^* \equiv \frac{u}{L_c} \quad v^* \equiv \frac{v}{L_c} \quad w^* \equiv \frac{w}{L_c} \quad (3.12)$$

Where,

$$V = \sqrt{u^2 + v^2 + w^2} \quad (3.14)$$

The non-dimensional pressure & temperature are:

$$p^* \equiv \frac{p - p_\infty}{p_o - p_\infty} \quad T^* \equiv \frac{T}{T_\infty} \quad (3.15)$$

Where, p_o is the reference pressure, p_∞ & T_∞ is the free stream pressure & temperature respectively.

The non-dimensional form of external gravitational acceleration:

$$g^* \equiv \frac{\bar{g}}{g} \quad (3.16)$$

Where, \bar{g} is the gravitational acceleration vector and g is the absolute value of that vector.

The ∇ operator is also needed to be non-dimensional:

$$\nabla^* \equiv \frac{\nabla}{D} \quad (3.17)$$

The upcoming section is the description of thermophysical properties of liquid metal and its effects on the dimensionless parameters (shown in Eq. 3.19, 3.22 & 3.27) which governs the thermal hydraulics of the liquid metals.

Table 3.1 Simplified Governing Equations in vector form, non-dimensional form, and differential form [59] & [39].

Equation	Vector Form (simplified)	Non-dimensional Form	Differential Form
Continuity Equation	$\nabla \cdot (\rho \vec{V}) = 0$ (3.18)	$\nabla^* (\rho^* \vec{V}^*) = 0$ (3.19)	$\frac{\partial(\rho u)}{\partial x} + \frac{\partial(\rho v)}{\partial y} + \frac{\partial(\rho w)}{\partial z} = 0$ (3.20)
Momentum Equation	$\rho \vec{V}(\nabla \vec{V}) = -\nabla p + \mu(\nabla^2 \vec{V}) + \rho \vec{g}$ (3.21)	$\vec{V}^*(\nabla^* \vec{V}^*) = -Eu(\nabla^* p^*) + \frac{1}{Re}(\nabla^{*2} \vec{V}^*) + \frac{1}{Fr^2} g^*$ (3.22)	<p>x-direction:</p> $\rho \left(u \frac{\partial u}{\partial x} + v \frac{\partial u}{\partial y} + w \frac{\partial u}{\partial z} \right) = -\frac{\partial p}{\partial x} + \mu \left(\frac{\partial^2 u}{\partial x^2} + \frac{\partial^2 u}{\partial y^2} + \frac{\partial^2 u}{\partial z^2} \right) + \rho g_x$ (3.23) <p>y-direction:</p> $\rho \left(u \frac{\partial v}{\partial x} + v \frac{\partial v}{\partial y} + w \frac{\partial v}{\partial z} \right) = -\frac{\partial p}{\partial y} + \mu \left(\frac{\partial^2 v}{\partial x^2} + \frac{\partial^2 v}{\partial y^2} + \frac{\partial^2 v}{\partial z^2} \right) + \rho g_y$ (3.24) <p>z-direction:</p> $\rho \left(u \frac{\partial w}{\partial x} + v \frac{\partial w}{\partial y} + w \frac{\partial w}{\partial z} \right) = -\frac{\partial p}{\partial z} + \mu \left(\frac{\partial^2 w}{\partial x^2} + \frac{\partial^2 w}{\partial y^2} + \frac{\partial^2 w}{\partial z^2} \right) + \rho g_z$ (3.25)
Energy Equation	$\vec{V}(\nabla T) = \alpha(\nabla^2 T)$ (3.26)	$\vec{V}^*(\nabla^* T^*) = \frac{1}{RePr}(\nabla^{*2} T^*)$ (3.27)	$\left(u \frac{\partial T}{\partial x} + v \frac{\partial T}{\partial y} + w \frac{\partial T}{\partial z} \right) = \alpha \left(\frac{\partial^2 T}{\partial x^2} + \frac{\partial^2 T}{\partial y^2} + \frac{\partial^2 T}{\partial z^2} \right)$ (3.28)

3.1. Liquid Metals & Dimensionless Numbers

Liquid metals are fundamentally different from non-metallic fluids, firstly they require high working temperatures to be maintained at liquid phase, secondly most or all of their thermophysical properties are temperature dependent. The temperature dependent behaviours of their properties warrant even more attention of its effects on the heat transfer and fluid flow characteristics. From the Table 3.1, by carefully observing the Eq. 3.19, 3.22 & 3.27, it can be seen that in the momentum and the energy equations, there are some non-dimensional parameters formed on which the thermal hydraulic behaviour depends upon.

The Froude Number (Fr):

$$Fr = \frac{V}{\sqrt{gD}} \quad (3.29)$$

It is the ratio of inertia force and the gravitational force. It is a parameter which defines the flow of fluid across a stagnant body like a cylinder or a flat plate when buoyancy is in effect.

The Euler Number (Eu):

$$Eu = \frac{p_o - p_\infty}{\rho V^2} \quad (3.30)$$

It is the ratio of pressure forces and the inertia force; it is significant where the pressure drop is observable and the loss of kinetic energy caused due to friction coefficient of the pipe or the plate on which the flow is occurring.

Both the above-mentioned dimensionless numbers are based upon the boundary conditions, which are defined by the user. However, the Reynolds number and the Prandtl number are based upon the thermophysical properties of the fluid in this particular case Liquid metals.

The Reynolds Number (Re):

$$Re = \frac{\rho V L_c}{\mu} = \frac{V L_c}{\nu} \quad (3.31)$$

The Reynolds number signifies the type of flow, it is the ratio of inertia forces and the viscous forces. For a low value of Re , the viscous forces are dominant over inertia forces, it is classified as Laminar flow. For high values of Re , the inertia forces are dominant over viscous forces, therefore the flow is classified as Turbulent Flow (will be discussed later in detail). The heavy liquid metals like LBE have high density and low dynamic viscosity, and alkali liquid metals like sodium & potassium have moderate density but with extremely low kinematic viscosity, therefore, the kinematic viscosity (or momentum diffusivity) becomes low ($\nu \sim 10^{-5}$). With exceptionally low kinematic viscosity, the Reynolds number is usually very high even with a low flow rate of the liquid metal. Hence, for most of the practical applications, the flow of liquid metals lies in the turbulence region only, and analysis of turbulent flow is highly complex which makes it a tedious task for the engineers.

The Prandtl Number (Pr):

$$Pr = \frac{\nu}{\alpha} = \frac{\mu c_p}{k} \quad (3.32)$$

It is the ratio of kinematic viscosity and the thermal diffusivity of a fluid. The value of Prandtl number signifies the ratio by which the fluid transfer momentum across the layer with respect to the amount of heat transfer. Considering the liquid metals, the liquid metals, in general, have low dynamic viscosity ($\mu \sim 10^{-3}$) and high thermal conductivity ($k \sim 10^2$). Therefore, the Prandtl number values for LM are usually in the range of 0.001 - 0.02. Such low value of Pr implies that during the flow of liquid metals, the heat transfer is way more significant than momentum transfer in contrast to general non-metallic fluids like water ($Pr \sim 1$).

3.2. Boundary Layer Theory

The heat transfer during a fluid flow always occurs due to temperature difference between the temperature of surface on which the fluid is flowing and the free stream temperature of the fluid therefore, study of the boundary layer is a key aspect for understanding the convection heat transfer. Considering a steady state, laminar 2-dimensional flow with constant properties. So, from the Eq. 3.23, 3.24 & 3.28, and converting them to non-dimensional form by using the following non-dimensional parameters:

$$\begin{aligned} x^* &= \frac{x}{L} & u^* &= \frac{u}{V} & p^* &= \frac{p}{\rho V^2} \\ y^* &= \frac{y}{L} & v^* &= \frac{v}{V} & T^* &= \frac{T - T_s}{T_\infty - T_s} \end{aligned} \quad (3.32)$$

Inside the boundary layer, the velocity, temperature, and pressure change with respect to the normal of surface i.e. the y-direction and with respect to x-direction their changes are very low. Hence, the equations become,

Momentum:

$$u^* \frac{\partial u^*}{\partial x^*} + y^* \frac{\partial u^*}{\partial y^*} = -\frac{dp^*}{dx^*} + \frac{1}{Re_L} \frac{\partial^2 u^*}{\partial y^{*2}} \quad (3.33)$$

Energy:

$$u^* \frac{\partial T^*}{\partial x^*} + y^* \frac{\partial T^*}{\partial y^*} = \frac{1}{Re_L Pr} \frac{\partial^2 T^*}{\partial y^{*2}} \quad (3.34)$$

The range of Prandtl number for liquid metals effect the study of thermal and hydraulic boundary layers since, the ratio of hydraulic boundary layer and thermal boundary layer is directly proportional to the Prandtl number.

$$Pr \propto \frac{\delta_h}{\delta_{th}} \quad (3.35)$$

Where, δ_h is the hydraulic boundary layer & δ_{th} is the thermal boundary layer. As it can be seen in the visual representation of boundary layers for LM and non-metallic fluids in Fig. 3.1, the thickness of thermal boundary layer is significantly larger than thickness of hydraulic boundary layer for LM in contrast to non-metallic fluids which have comparable boundary layer thicknesses.

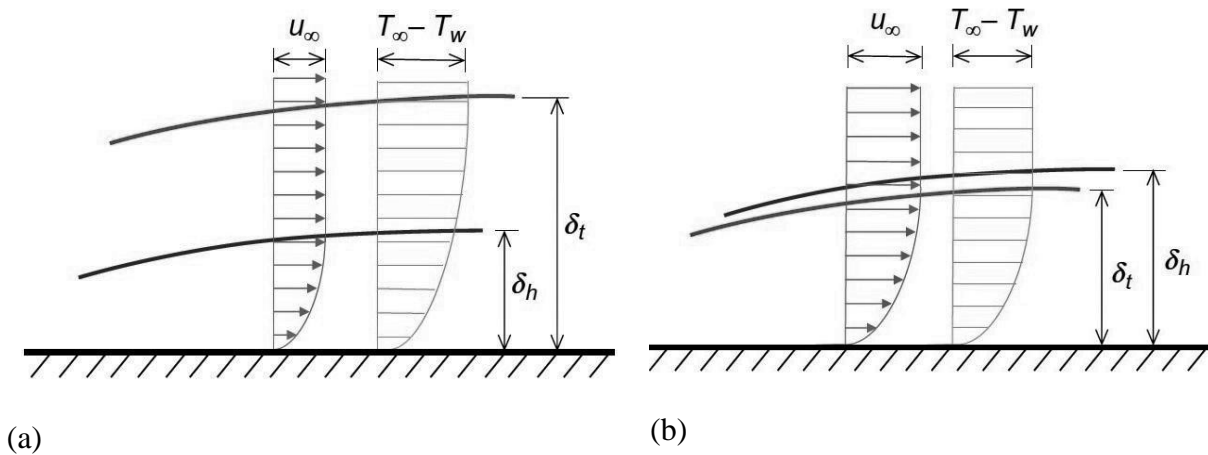


Fig. 3.1 Showing the thermal boundary layer (red) and hydrodynamic boundary layer (blue) (a) for Liquid Metal (b) for non-metallic fluids

The enhanced height of thermal boundary layer with respect to hydraulic boundary layer for liquid metals signify that the rate of heat transfer is more significant than the rate of momentum transfer which is also in correspondence to the value of the Prandtl number already discussed.

From the above description of boundary layers and Eq. 3.33, it can be asserted that the solution of u^* can be shown in the form

$$u^* = f_1(x^*, y^*, Re_L) \quad (3.36)$$

$$\frac{\partial u^*}{\partial y^*} = f_2(x^*, Re_L) \quad (3.37)$$

Then, the shear stress on the fluid at the surface becomes

$$\tau_w = \mu \frac{\partial u}{\partial y}_{y=0} = \frac{\mu V}{L} \frac{\partial u^*}{\partial y^*}_{y=0} = \frac{\mu V}{L} f_2(x^*, Re_L) \quad (3.38)$$

For finding the friction factor f_D , also called as the Darcy-Weisbach Friction Factor.

$$f_D = \frac{\tau_w}{\rho V_{avg}^2 / 8} = \frac{\frac{\mu V}{L}}{\rho V_{avg}^2 / 8} f_2(x^*, Re_L) \quad (3.39)$$

$$f_D = f_3(x^*, Re_L) \quad (3.40)$$

The pressure loss for the length L with average velocity V_{avg} for fully developed internal laminar or turbulent flows with diameter D is expressed as

$$\Delta p_L = f_D \frac{L}{D} \frac{\rho V_{avg}^2}{2} \quad (3.41)$$

Therefore, the pressure drop can also be expressed as a function of Reynolds number.

Similarly, from Eq. 3.34, it can be observed that the T^* can be expressed in a form of equations

$$T^* = g_1(x^*, y^*, Re_L, Pr) \quad (3.42)$$

$$\frac{\partial T^*}{\partial y^*} = g_2(x^*, Re_L, Pr) \quad (3.43)$$

For finding the convective heat transfer coefficient for heat transfer from the surface,

$$h_x(T_s - T_\infty) = -k \left(\frac{\partial T}{\partial y} \right)_{y=0} \quad (3.44)$$

$$h_x = \frac{-k(T_\infty - T_s)}{L(T_s - T_\infty)} \frac{\partial T^*}{\partial y^*}_{y=0} = \frac{k}{L} \frac{\partial T^*}{\partial y^*}_{y=0} \quad (3.45)$$

Where, h_x is the local convective heat transfer coefficient at the position x .

The Nusselt Number (Nu):

$$Nu_x = \frac{h_x L}{k} \quad (3.46)$$

The Nusselt number is the non-dimensional form of convective heat transfer coefficient, it can also be termed as the ratio of rate of convective heat transfer and the rate of conductive heat transfer. Physical significance of the Nusselt number is basically the enhancement in the rate of heat transfer in a fluid layer as a result of motion with respect to conduction heat transfer in the same fluid layer. It is also referred as the ratio of conduction thermal resistance and convection thermal resistance for same parameters. From Eq. 3.43 it is understandable that the convective heat transfer coefficient in a fluid is dependent upon the temperature gradient normal to the surface. From Eq. 3.41, it is inferred that the temperature gradient is a function of non-dimensional parameters as mentioned. From Eq. 3.43 & 3.45,

$$Nu_x = \frac{h_x L}{k} = \frac{\frac{k}{L} \frac{\partial T^*}{\partial y^*}_{y=0}}{k} L = \frac{\partial T^*}{\partial y^*}_{y=0} \quad (3.47)$$

$$Nu_x = g_2(x^*, Re_L, Pr) \quad (3.48)$$

From the Eq. 3.48, the Nusselt number can be calculated. For average values of Nu , the equations are needed to be integrated for x^* . The Nusselt number becomes,

$$Nu = g_3(Re_L, Pr) \quad (3.49)$$

The experimental correlations developed over the years by various researchers and scientist tend to follow the functional trend shown in Eq. 3.41 & 3.49.

3.3. Turbulent Flow

Turbulent flow is the type of flow where the fluid flow parameters like velocity, pressure & temperature are not steady but also has a fluctuating component. Turbulent flow can be classified as the sum average values of parameters and the fluctuating components of those parameters. Consider the velocities in x, y, z directions, the average components of the velocities are $\bar{u}, \bar{v}, \bar{w}$ respectively along with the fluctuating components u', v', w' . Thus, the actual velocity components in turbulent flow are

$$u = \bar{u} + u' \quad (3.50a)$$

$$v = \bar{v} + v' \quad (3.50b)$$

$$w = \bar{w} + w' \quad (3.50c)$$

This phenomenon also applies to the pressure and the temperature in turbulent flow thus, $P = \bar{P} + P'$ & $T = \bar{T} + T'$.

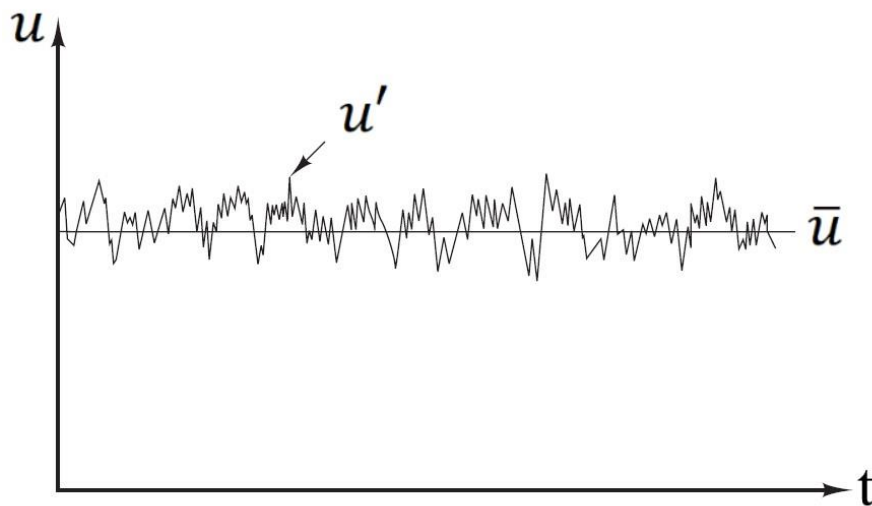


Fig. 3.2 x-velocity with time showing average and fluctuating component

The main purpose to the study the boundary layer theory is to incorporate the effects of turbulence to the wall shear stress and the heat transfer from the surface. In

analogous to the laminar shear stress $\tau = \mu \left(\frac{\partial \bar{u}}{\partial y} \right)$, the turbulent shear stress is expressed as

$$\tau_{turb} = \mu_t \frac{\partial \bar{u}}{\partial y} \quad (3.51)$$

Where, the μ_t is the turbulent viscosity, which drives the momentum transfer by eddy formations during turbulent flows. Thus, the total shear stress at the wall will be,

$$\tau_{total} = \tau + \tau_{turb} = \mu \frac{\partial \bar{u}}{\partial y} + \mu_t \frac{\partial \bar{u}}{\partial y} \quad (3.52)$$

$$\tau_{total} = (\mu + \mu_t) \frac{\partial \bar{u}}{\partial y} \quad (3.53)$$

$$\tau_{total} = \rho(\nu + \nu_t) \frac{\partial \bar{u}}{\partial y} \quad (3.54)$$

Where, the ν_t is the turbulent momentum diffusivity or kinematic turbulent viscosity.

Similarly, the turbulent heat transfer from the surface is expressed as

$$q_{turb} = -k_t \frac{\partial T}{\partial y} \quad (3.55)$$

Where, the k_t is the turbulent thermal conductivity, which accounts to the heat transfer due eddy formations in turbulent flow. Thus, the total heat transfer from the heated surface is

$$\dot{q}_{total} = \dot{q}_{lam} + \dot{q}_{turb} = - \left(k \frac{\partial T}{\partial y} + k_t \frac{\partial T}{\partial y} \right) \quad (3.56)$$

$$\dot{q}_{total} = -(k + k_t) \frac{\partial T}{\partial y} \quad (3.57)$$

$$\dot{q}_{total} = -\rho c_p (\alpha + \alpha_t) \frac{\partial T}{\partial y} \quad (3.58)$$

Where, α_t is the turbulent thermal diffusivity.

Since, the Prandtl number is the ratio of momentum diffusivity and thermal diffusivity thus, turbulent Prandtl number can be defined as the ratio of turbulent momentum diffusivity and the turbulent thermal diffusivity.

$$Pr_t = \frac{\nu_t}{\alpha_t} \quad (3.59)$$

The Eq. 3.60 can be inserted in the Eq. 3.59,

$$\dot{q}_{total} = -\rho c_p \left(\alpha + \frac{\nu_t}{Pr_t} \right) \frac{\partial T}{\partial y} \quad (3.60)$$

As it can be seen that the total heat transfer also incorporates the turbulent Prandtl number therefore, the function of avg. Nusselt number must also incorporate the turbulent Prandtl number as well thus, the Eq. 3.50 becomes

$$Nu = g_3(Re_L, Pr, Pr_t) \quad (3.61)$$

There is a lot of research and various kinds of correlations developed which include the turbulent Prandtl number.

3.4. Pressure Drop in Liquid Metals

Pressure drop in laminar flow depends on the wall shear stress as mentioned in previous section, which is the function of the Reynolds number as shown in Eq. 3.40. The Darcy friction factor (f_D) for turbulent flow also depends on the surface roughness of the pipe in which the fluid is flowing. The Darcy friction factor for turbulent flow was given by Colebrook [59]:

$$\frac{1}{\sqrt{f_D}} = -2 \log \left\{ \frac{\epsilon_R/D}{3.7} + \frac{2.51}{Re \sqrt{f_D}} \right\} \quad (3.62)$$

Where, ϵ_R is the surface roughness of the pipe flow.

Another term called Fanning friction factor was developed and a simplified correlation was given by Colebrook [58] & [20].

$$\frac{1}{\sqrt{f}} = 1.5635 \ln \left\{ \frac{Re}{7} \right\} \quad (3.63)$$

Where, the fanning friction factor is 1/4th of the Darcy friction factor.

$$f = \frac{f_D}{4} \quad (3.64)$$

The accuracy of Eq. 3.63 is relatively low and the Eq. 3.62 requires iterative methods for solving. Moody [58] studied the effect of surface roughness and inlet flow condition to construct a chart showing variation of the Darcy friction factor with Reynolds number for various roughness values, a correlation was also formed in that study showing the same.

$$f = 1.375 \times 10^{-3} \left[1 + 21.544 \left\{ \frac{2\epsilon_R}{D} + \frac{100}{Re} \right\}^{1/3} \right] \quad (3.65)$$

In this study, the pressure drop for liquid metals is compared by Colebrook's correlation, Moody's correlation, and Tecko's correlation [19] given below.

$$\frac{1}{\sqrt{f}} = 1.7372 \ln \left(\frac{Re}{1.964 \ln Re - 3.8215} \right) \quad (3.66)$$

The material chosen in this is study is 316L stainless steel which has the surface roughness of $\epsilon_R = 0.015 \text{ mm}$ [19], therefore for pressure loss calculation the roughness will be taken as such.

3.5. Heat Transfer in Liquid Metals

The experimentation studies conducted to analyze the behaviour of the Nusselt number with respect to the Reynolds number and the Prandtl number. This behaviour was analytically achieved in Eq. 3.49 also shown below

$$Nu = f(Re, Pr) \quad (3.67)$$

From past experiences, the function followed a general pattern as it does in the non-metallic fluids, shown below

$$Nu = a + bRe^cPe^d \quad (3.68)$$

But, with the observation of the results for liquid metals, it was inferred that the coefficient c & d are equal. Therefore, the general function was altered.

$$Nu = a + b(Re.Pr)^c \quad (3.69)$$

And,

$$Re \times Pr = Pe \quad (3.70)$$

$$Nu = a + b(Pe)^c \quad (3.71)$$

Where, Pe is the Peclet number, it is the product of Reynolds number and the Prandtl number. The value of Peclet number signifies the ratio of convection transport and the thermal energy diffusion.

The studies were conducted usually by maintaining two type of boundary conditions at the pipe wall, the constant heat flux boundary condition, and the constant temperature boundary condition at the pipe wall.

3.5.1. Constant Heat Flux

In the experimental research conducted by Lyon [64], the Nusselt number was shown to be a function of Peclet number for constant heat flux ($\dot{q}_{flux} = constant$) boundary condition at the pipe wall. The studies conducted by Ibragimov et al. [5], Subbotin et al. [24] and Kirillov & Ushakov [62] also resulted in correlation showing Nusselt number as a function of Peclet number.

Lyon's correlation:

$$Nu = 7 + 0.025Pe^{0.8} \quad (3.72)$$

Valid for $4 \times 10^3 < Re < 3 \times 10^6$ & $0 < Pr < 0.1$

Ibragimov's correlation:

$$Nu = 4.5 + 0.014Pe^{0.8} \quad (3.73)$$

Valid for all range of Re & Pr, for mercury and LBE.

Subbotin's correlation:

$$Nu = 5 + 0.025Pe^{0.8} \quad (3.74)$$

Valid for all range of Re & Pr, for liquid sodium.

Kirillov & Ushakov's correlation:

$$Nu = 4.5 + 0.018Pe^{0.8} \quad (3.75)$$

For $Re > 10^4$.

The mentioned correlations have been used for showing comparisons and also for validation for various studies [15], [18], [20], [22], [23], [25], [32], [34], [40].

3.5.2. Constant Temperature

Many of the studies were conducted to understand the effect of isothermal boundary condition of the pipe wall on the heat transfer phenomenon during liquid metal flow.

The studies conducted by Seban & Shimazaki [60], Notter & Sleicher [41], Sleicher et al. [42], and Chen & Chiou [43] resulted in the formation of correlations showing the Nusselt number was the function of Peclet number as well.

Seban & Shimazaki's correlation [60]:

$$Nu = 5 + 0.025Pe^{0.8} \quad (3.76)$$

Notter & Sleicher's correlation [41]:

$$Nu = 4.8 + 0.0156Pe^{0.85}Pr^{0.08} \quad (3.77)$$

Eq. 3.77 is valid for $10^4 < Re < 10^6$ & $0.004 < Pr < 0.1$.

Sleicher's correlation [42]:

$$Nu = 2.75 + 0.02Pe^{0.8} \quad (3.78)$$

Eq. 3.78 is valid for $0.004 < Pr < 0.1$.

Chen & Chiou's correlation [43]:

$$Nu = 4.5 + 0.0156Pe^{0.85}Pr^{0.01} \quad (3.79)$$

Eq. 3.79 is valid for $10^4 < Re < 5 \times 10^6$ & $0 < Pr < 0.1$.

These correlations are used in several studies for validation and comparison of experimental results [10], [20], [22], [23], [25], [30], [40], [44], [45].

3.6. Turbulent Prandtl Number

For turbulent flows, the Turbulent Prandtl number is assumed to be in range of 0.85–1 however, this range is not valid for the case of liquid metals. Lyon [64] & Martinelli [57] suggested that the turbulent Prandtl number is needed to be incorporated in the Nusselt number correlations. Therefore, they suggested a new correlation called the “Lyon-Martinelli’s Correlation”

$$Nu = 7 + 0.025 \left(\frac{Pe}{Pr_t} \right)^{0.8} \quad (3.80)$$

But in the study conducted by Lyon [64] the turbulent Prandtl number was neglected. ($Pr_t \sim 1$). In the study conducted by Aoki [56], a correlation was proposed which showed the Turbulent Prandtl number as the function of the Reynolds number and the Prandtl number for internal turbulent flows.

$$Pr_t = \left\{ 0.014A \left[1 - e^{\left(\frac{-1}{0.014A} \right)} \right] \right\}^{-1} \quad (3.81)$$

Where,

$$A = Re^{0.45} Pr^{0.2} \quad (3.82)$$

However, the study conducted by Taler [23] in which it was proposed that the coefficient of A can be altered. A new correlation for the turbulent Prandtl number was proposed.

$$Pr_t = \left\{ aA \left[1 - e^{\left(\frac{-1}{bA} \right)} \right] \right\}^{-1} \quad (3.83)$$

Where, a & b coefficients of A are computed by least square based method of regression technique using the data of Sheriff & O’Kane [46] for liquid sodium. Two type of equations were developed, the model I correlation is

$$Pr_t = \left\{ 0.01592A \left[1 - e^{\left(\frac{-1}{0.01592A} \right)} \right] \right\}^{-1} \quad (3.84)$$

And the Model II correlation is

$$Pr_t = \left\{ 0.01177A \left[1 - e^{\left(\frac{-1}{0.007117A} \right)} \right] \right\}^{-1} \quad (3.85)$$

Taler [23] used the above to correlations and incorporated the turbulent Prandtl number in the Lyon-Martinelli's correlation to form two new correlations.

$$Nu = 5.72 + 0.0184Pe^{0.8205} \quad (3.86a)$$

$$Nu = 5.51 + 0.015Pe^{0.865} \quad (3.86b)$$

These correlations are valid for $3 \times 10^3 \leq Re \leq 3 \times 10^6$ and $0.0001 \leq Pe \leq 0.1$.

3.7. Properties of Liquid Metals

In this study three liquid metals are considered, Lead-Bismuth Eutectic (LBE), liquid sodium, and mercury (Hg). In this section, the behaviour of thermophysical properties of liquid metals is briefly explained. As mentioned in previous section, for most of the liquid metals the properties are temperature dependent, i.e. they can be represented as functions of temperature. The user-defined functions which are programmed in C language for the thermophysical properties of the liquid metals used in the simulations are shown in the Appendix A.

I. Sodium

Sodium (Na) is a light alkali metal with melting point at $T_{melt} = 98^\circ\text{C}$ (371 K) and boiling point at $T_{boil} = 883^\circ\text{C}$ (1156 K). Liquid sodium is mostly non-lethal therefore preferred over the use of other liquid metals as coolants. However, Liq. sodium reacts with oxygen and hydrogen to form sodium oxide and sodium hydride respectively,

which can hinder the general working condition of any thermal system involved. The thermophysical properties of sodium are [47]:

Density ($\rho, kg/m^3$):

$$\rho = 954.1579 + [(0.9667 \times 10^{-9}T - 0.46005 \times 10^{-5})T - 0.1273534]T \quad (3.87)$$

Specific Heat is considered to be constant $c_p = 1320 J/kg.K$

Thermal conductivity ($k, W/m.K$):

$$k = 93.9892 - 3.20503 \times 10^{-2}t_f + 3.6197 \times 10^{-6}t_f^2 \quad (3.88)$$

Where, $t_f = 1.8(T - 273.15) + 32$.

Dynamic Viscosity ($\mu, N.s/m^2$):

$$\mu = \frac{0.11259 \times 10^{-3} e^{\left(\frac{\rho}{1.3349T}\right)}}{\left(\frac{1000}{\rho}\right)^{0.333}} \quad (3.89)$$

All the above relations are valid for ($370 K < T < 1100 K$).

II. Lead-Bismuth Eutectic

Lead-Bismuth Eutectic (LBE) alloy is heavy metal having 44.5% (*Pb*) lead and 55.5% (*Bi*) bismuth with melting point at $T_{melt} = 125^\circ C$ ($398K$) & boiling point at $T_{boil} = 1670^\circ C$ ($1943K$). LBE is highly reactive with all constituents of atmospheric air, it forms lead oxide when it comes in contact with air. Therefore, special care and precautions are required while using LBE as coolant in thermal systems. The thermal conductivity of LBE is relatively lower than that of liq. Na and comparable to Mercury. The thermophysical properties of LBE are [25]:

Density ($\rho, kg/m^3$):

$$\rho = 11105 - 1.3312T \quad (3.90)$$

Specific Heat is considered to be constant $c_p = 146.341 J/kg.K$

Thermal conductivity ($k, W/m.K$):

$$k = 5.3557 - 1.181 \times 10^{-2}T \quad (3.91)$$

Dynamic Viscosity ($\mu, N.s/m^2$):

$$\mu = 5.293 \times 10^{-4} e^{\left(\frac{732.3}{T}\right)} \quad (3.92)$$

All the above relations are valid for ($398 K < T < 1300 K$).

III. Mercury

Mercury (Hg) is lethal liquid metal which exists in liquid phase at room temperature, it is lethal mainly because of its harmful effects on human beings. The melting point of the Hg is $T_{melt} = -38.8^\circ\text{C}$ ($234.2 K$) and the boiling point is $T_{boil} = 356.7^\circ\text{C}$ ($629.7 K$). The mercury is non-reactive in ambient environment and at room temperatures, along with moderate thermal conductivity, making it ideal for being used as a coolant. The thermophysical properties of mercury are [25]:

Density ($\rho, kg/m^3$):

$$\begin{aligned} \rho = 13595[& 1 - 1.8144 \times 10^{-4}(T - 273.15) \\ & - 7.016 \times 10^{-9}(T - 273.15)^2 \\ & - 2.8625 \times 10^{-11}(T - 273.15)^3 \\ & - 2.617 \times 10^{-14}(T - 273.15)^4] \end{aligned} \quad (3.93)$$

Specific Heat is considered to be constant $c_p = 135.4 J/kg.K$

Thermal conductivity ($k, W/m.K$):

$$\begin{aligned} k = 8.178 - 1.36 \times 10^{-2}(T - 273.15) \\ - 6.378 \times 10^{-8}(T - 273.15)^2 \end{aligned} \quad (3.94)$$

Dynamic Viscosity ($\mu, N.s/m^2$):

$$\mu = 3 \times 10^{-4} e^{\left(\frac{341.13}{T}\right)} \quad (3.95)$$

All the above relations are valid for ($273 K < T < 1073 K$).

3.8. Intermediate Heat Exchanger Designing

In this thesis, a counter flow double-pipe heat exchanger is designed for heat transfer between glycerol & liquid metals for its potential use in liquid metal cooled reactor (LMCR). Liquid metal is taken to be the hot fluid (subscript h) flowing through the inner circular tube and the Glycerol is taken to be the cold fluid (subscript c) flowing through the circular annulus region. The diameters of inner tube are $d_i = 10\text{mm}$ & $d_o = 13\text{mm}$ respectively, and the diameters of the outer tube are $D_i = 25\text{mm}$ & $D_o = 28\text{mm}$ respectively. For this study, three values of IHX lengths are taken 250 mm , 500 mm , & 1000 mm , in order to truly understand the behaviour of liquid metal heat transfer for different inlet boundary conditions. The 3-dimensional model of the heat exchanger is shown in the Fig. 3.3, the inlet and outlet boundaries of the working fluids are clearly visible.

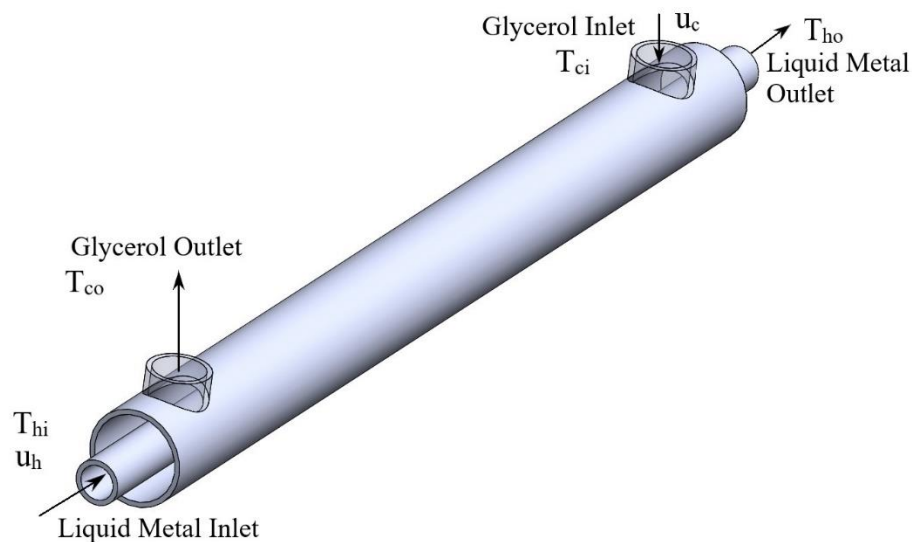


Fig. 3.3 Three-Dimensional Model of the IHX

The heat transfer characteristics of the IHX namely the logarithmic mean temperature difference (LMTD), the overall heat transfer coefficient, and the total rate of heat transfer are analyzed with variations in the inlet boundary conditions. For the analysis

of the IHX two liquid metals are considered, Lead-Bismuth Eutectic (LBE) alloy & Liq. Sodium. The inlet temperature of liquid metals is varied from 553 K to 773 K and the inlet temperature of glycerol is varied from 373 K to 473 K. The inlet velocity of LBE is varied from 0.5 m/s to 2.0 m/s and the inlet velocity of Liq. Na is varied from 5.875 m/s to 23.5 m/s. The inlet velocities of LBE & liq. Na are chosen such as to have equal mass flow rate at 553 K inlet temperature to compare the heat transfer characteristics. The inlet velocity of glycerol is kept constant at 1.163 m/s.

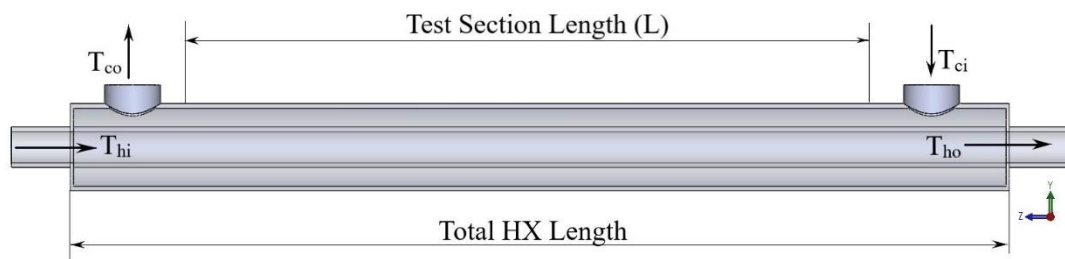


Fig. 3.4 Axial View of the IHX

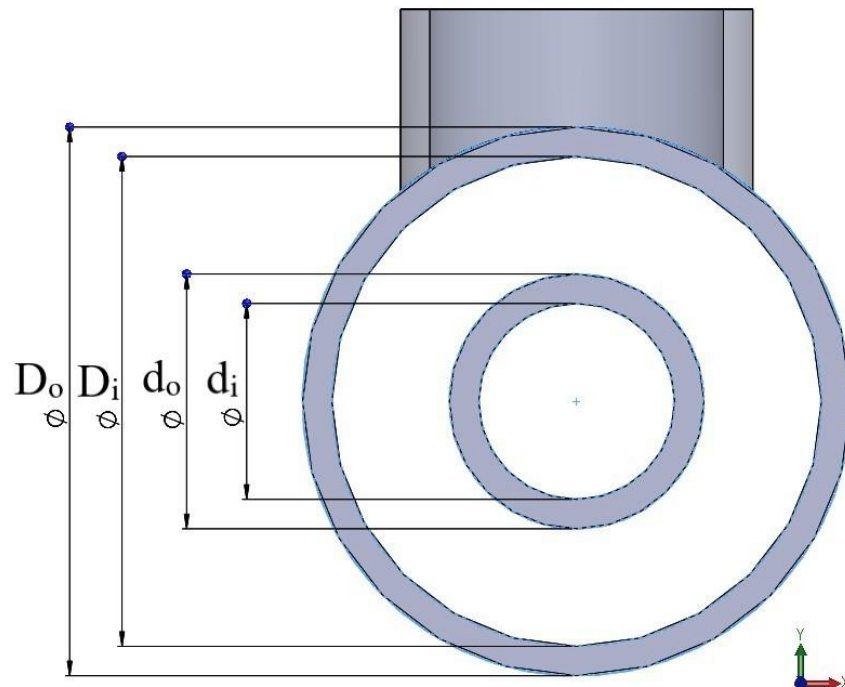


Fig. 3.5 Cross-sectional view of the IHX showing the various diameters of tube and the annulus region

The Fig. 3.4 & 3.5 are representing the axial and cross-sectional view of the IHX model respectively. It can be observed that the test section length is smaller than the total length of the IHX since, significant heat exchange will only be taking place in that portion of the tube length.

For heat transfer analysis some assumptions are considered:

1. The outer wall of shell is perfectly insulated, that means heat transfer is only occurring between the two working fluids.
2. The axial conduction is neglected.
3. Specific heat is constant for both the fluids.
4. Properties of glycerol are kept constant.
5. The thermal conductivity, viscosity, and density are all temperature dependent for liquid metals.
6. The Reynolds number and Prandtl number is calculated at inlet condition.

The mass flow rate of hot fluid (liquid metal) in kg/s:

$$\dot{m}_h = \rho_h A_i u_h \quad (3.96)$$

The mass flow rate of glycerol in kg/s:

$$\dot{m}_c = \rho_c A_o u_c \quad (3.97)$$

The rate of heat transfer in the IHX will be:

$$Q = \dot{m}_h c_{ph} (T_{hi} - T_{ho}) = \dot{m}_c c_{pc} (T_{co} - T_{ci}) \quad (3.98)$$

The rate of heat transfer is also represented by:

$$Q = U_i S_i \Delta T_{lm} = U_o S_o \Delta T_{lm} \quad (3.99)$$

Where, the U is the overall heat transfer coefficient and S is the surface area through which the heat exchange is taking place, i & o in the suffix represents the inner and the outer wall of the tube.

The overall heat transfer coefficient depends on the convection at the hot side & the cold side and also the conduction in the tube, thus

$$\frac{1}{US} = \frac{1}{U_i S_i} = \frac{1}{U_o S_o} = \frac{1}{h_h S_i} + \frac{\ln(r_2/r_1)}{2\pi LK} + \frac{1}{h_c S_o} \quad (3.100)$$

Where, h_h is the convective heat transfer coefficient for the inner fluid flow i.e. the hot fluid (liquid metal) and h_c is the convective heat transfer coefficient for the outer fluid flow i.e. the cold fluid (glycerol) & the middle term is the conductive thermal resistance of the tube. The analytical calculation of convective heat transfer coefficient for the liquid metal is quite difficult because the wall boundary condition neither follows the constant heat flux condition nor the constant temperature condition, and moreover the properties of liquid metals are temperature dependent, therefore the properties change during the heat exchanger. Therefore, numerical approach is feasible in solving heat transfer involving the liquid metals in heat exchangers.

Since, the heat exchanger is counter flow then the LMTD will be:

$$\Delta T_{lm} = \frac{(T_{hi} - T_{co}) - (T_{ho} - T_{ci})}{\ln\left(\frac{T_{hi} - T_{co}}{T_{ho} - T_{ci}}\right)} \quad (3.101)$$

3.9. Heat Transfer Enhancements

There are a number of ways to enhance the rate of heat transfer, in this thesis the application of extended surfaces has been employed. The extended surfaces or Fins increase the area for convective heat transfer without increasing the conductive thermal resistance significantly. The longitudinal fins are attached to the outer surface of the tube in the annulus region where the glycerol is flowing. The thickness of fins is kept constant at $t = 0.5 \text{ mm}$ and the length of fins are 2.5 mm , 4.0 mm , & 5.5 mm . The Fig. 3.6 is showing the cross-section view of the IHX along with the parameters of fins attached.

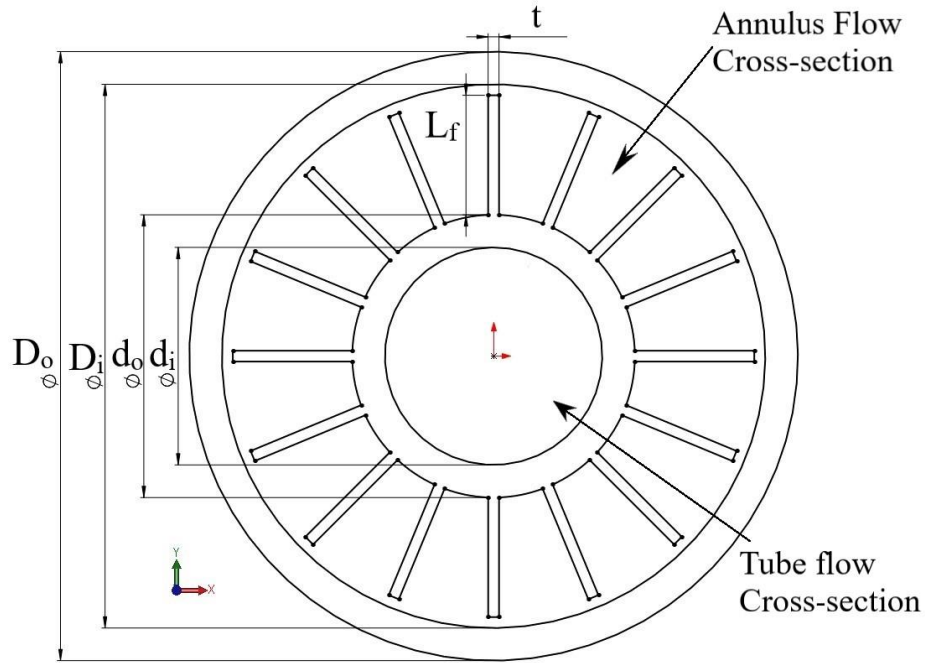


Fig. 3.6 Cross-section of IHX with fins

The application of fins will alter the cross-sectional flow area.

$$A'_o = \frac{\pi}{4} (D_i^2 - d_o^2) - n_f L_f t \quad (3.102)$$

Where, n_f is the number of fins. The total outer surface area tube

$$S'_o = (\pi d_o - n_f t + 2n_f L_f) L \quad (3.103)$$

The efficiency of single fin:

$$\eta_f = \frac{\tanh(m L_{fc})}{m L_{fc}} \quad (3.104)$$

Where, L_{fc} is the corrected fin length.

$$L_{fc} = L_f + 0.5t \quad (3.105)$$

and m is the dimensionless number is:

$$m = \sqrt{\frac{h_c t}{k_c L_f}} \quad (3.106)$$

Where, k_c is the thermal conductive of the cold fluid (glycerol)

The overall efficiency:

$$\eta_o = 1 - \frac{S_f}{S'_o} (1 - \eta_f) \quad (3.107)$$

The overall efficiency will be incorporated in the overall heat transfer coefficient calculation.

$$\frac{1}{US} = \frac{1}{U_i S_i} = \frac{1}{U_o S'_o} = \frac{1}{h_h S_i} + \frac{\ln(r_2/r_1)}{2\pi L K} + \frac{1}{\eta_o h_c S'_o} \quad (3.108)$$

The effectiveness of the fins is calculated by:

$$\epsilon = \frac{Q_{fins}}{Q_{without fins}} \quad (3.109)$$

Where, Q_{fins} and $Q_{without fins}$ are both computed by CFD analysis.

Another parameter has also been defined in this study, non-dimensional overall heat transfer coefficient.

$$U^* = \frac{U}{U_o} \quad (3.110)$$

Where, U_o is the reference overall heat transfer coefficient.

Chapter 4 – Numerical Modelling

In this chapter, the procedure by which the numerical modelling of the intermediate heat exchanger is done and the steps taken during CFD analysis have been explained. The description of meshing generation and turbulence modelling has been done in this chapter as well. The validation of heat transfer process during turbulent flow in tube is performed by comparing the results with well-established experimental results and empirical correlations. The concept of artificial neural network is briefly explained and the Python code for ANN regression algorithm is shown for one particular case.

4. NUMERICAL MODELLING

Computational Fluid Dynamics (CFD) is the method of solving heat transfer and fluid flow problems by numerical methods using computer simulations. The utilization of CFD analysis became feasible with the advancement in computational powers of computers and with time the cost of experimentation also increased thus, the researchers usually prefer computational techniques for solving fluid flow and heat transfer problems. The CFD codes or analysis software all follow the same basic procedure.

I. PREPROCESSING

The model that has to be solved, is needed to be defined according to the CFD software.

- The fluid domains, solid domains, interfaces, walls boundary conditions, symmetry etc. all geometrical parameters are defined in preprocessing.
- The domains are divided into many small elements, this process is called Mesh generation or grid generation.
- The selection of the type of meshing is extremely crucial to the solving parameters.

II. SOLVING

- The CFD tool linearizes the governing equations by approximations and boundary conditions defined by the user.

- These linearized governing equations are converted to algebraic form and are solved for each discretized control volume.
- Then the solutions are computed over the whole domain.

III. POSTPROCESSING

Post-processing includes representation of temperature profiles, velocity profiles and any other variable which the user would like to be monitored. The representation can be of various types like

- 2D contours.
- 3D contours.
- X-Y plots.
- Streamlines etc.

4.1. CFD Modelling

In this study, all of the geometrical models are prepared in Solidworks software and Ansys Fluent has been used for CFD analysis. The Ansys Fluent uses the Finite Volume Method to discretize the computational domain into a number of small control volumes. The Pressure-based solver is used to linearize the required governing equation by applying suitable approximations and the boundary conditions defined for this study. SIMPLE algorithm is used for pressure-velocity coupling. Second-order upwind is used for pressure, energy, and momentum equations. The residual values for momentum and continuity are set to 10^{-4} and for energy, it is set to 10^{-8} .

Initially for this study, 3-dimensional IHX geometrical designs were prepared for simulations but due to the limitations of computing power, the designs were shifted to 2-dimensional. However, a comparison of 3-dimensional simulation and 2-dimensional has been explained. A simple double-pipe type of heat exchanger was

chosen for the design of IHX. The double-pipe HX is a simple tube-in-tube system in which one fluid flows in the inner tubular cross-section and the other fluid flows through the annulus cross-section. By design, this IHX is symmetrical about 2 axes, therefore 1/4th design is selected for simulations. From Fig. 4.1 it can be observed that the inlet and outlet face for liquid metal and glycerol are clearly visible and the two walls about which the model is symmetrical are also represented.

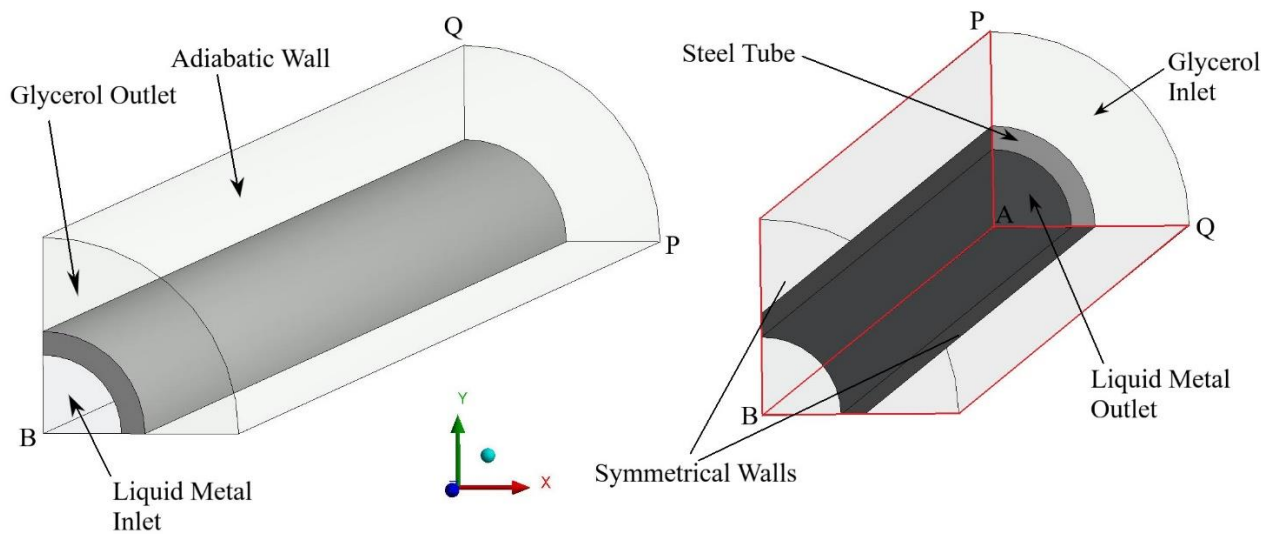


Fig. 4.1 1/4th Symmetrical 3D Model of the IHX showing the wall of symmetry

Due to limitations in computing power, only few of the cases were solved for the 3-dimensional model. The glycerol inlet velocity is constant at 1.163 m/s and temperature 423K , with the temperature of LBE was varied from 553K to 673K and the velocity was varied from 0.5 m/s to 2.0 m/s . These cases are compared to 2-dimensional model.

Fig. 4.2 shows the 2-dimensional model with the boundary wall and designations. For 2-dimensional modelling of IHX, the glycerol inlet velocity was kept constant at 1.163 m/s and the inlet temperature is varied from 373K to 473K . Two liquid metals are chosen to be used as coolants in the IHX, firstly Lead-bismuth eutectic (LBE) and secondly Liq. Sodium (Na). The inlet temperature is being varied from 553K to 773K , for LBE the inlet velocity is varied from 0.5 m/s to 2.0 m/s , and for Liq. sodium the

inlet velocity is varied from 5.875 m/s to 23.5 m/s . The inlet velocities of LBE and Liq. sodium are specifically selected such that the inlet mass flow rate at 553K is equal for both liquid metals in order to properly compare the heat transfer characteristics.

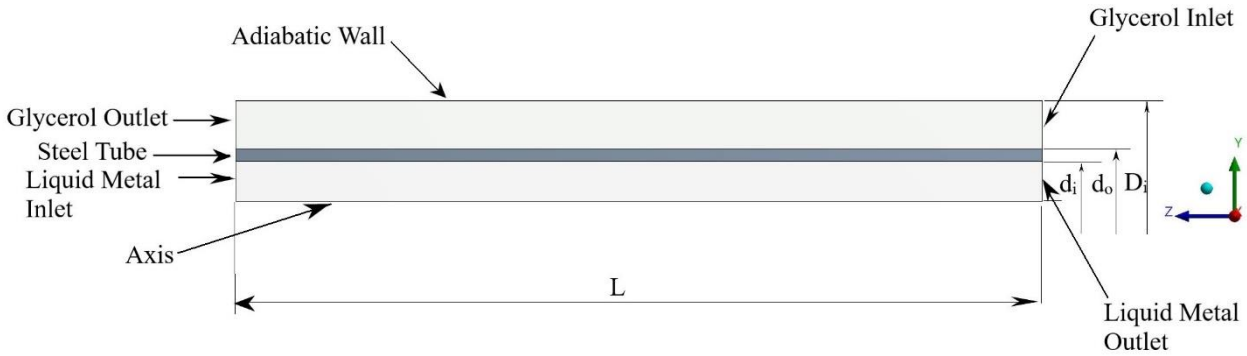


Fig. 4.2 2-Dimensional Model of IHX used for simulation

Fig. 4.3 is showing the variation of the total rate of heat transfer with increasing Reynolds number of LBE for various inlet temperature comparing 3-dimensional and 2-dimensional modelling of IHX. The outputs for the total rate of heat transfer is seen to be in very close range and the relative squared error (RSE) for 3D and 2D outputs is coming out to be 0.09065.

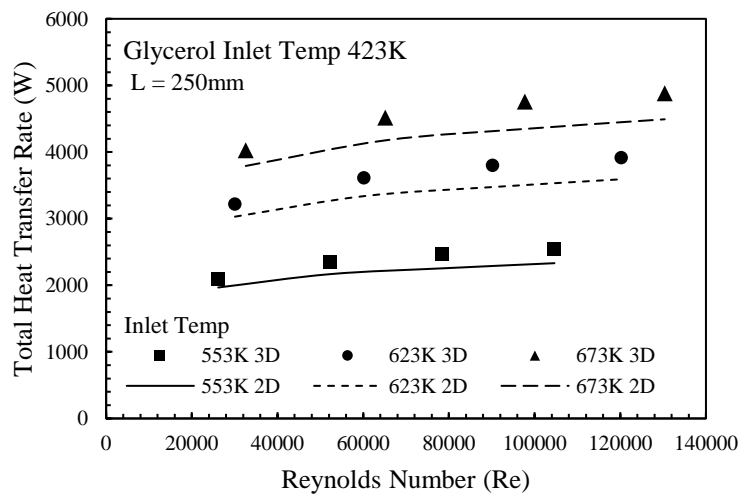


Fig. 4.3 Variation of Total Heat Transfer with Reynolds number showing comparisons between 3-dimensional & 2-dimensional CFD results

4.2. Turbulence Modelling

In this study, turbulence modelling is used since for all of the cases, the flow is in turbulent flow region. In Ansys Fluent, there are several types of viscous models, choosing the type of viscous model is crucial to the analysis and should be based on pre-calculations and judgement of the researcher. For this study, realizable $k - \varepsilon$ model is used for simulations.

The $k - \varepsilon$ is a two-equation model since along with 4 basic governing equations it also solves the equations for turbulent kinetic energy (k) and turbulent kinetic energy dissipation rate (ε) making it 6 equations in total. It is assumed that the turbulent flow is fully developed and the molecular viscosity is not taken into consideration for solving these equations.

For $k - \varepsilon$ model, the turbulent viscosity is

$$\nu_t = \frac{C_v k^2}{\varepsilon} \quad (4.1)$$

Where, C_v is the model constant.

For turbulence modelling for IHX in this thesis realizable $k - \varepsilon$ is chosen. The equation for turbulent kinetic energy (k) is

$$\frac{\partial \rho k}{\partial t} + \frac{\partial(\rho k u_j)}{\partial x_j} = \frac{\partial}{\partial x_j} \left\{ \left(\mu + \frac{\mu_t}{\sigma_k} \right) \frac{\partial k}{\partial x_j} \right\} + G_k + G_b - \rho \varepsilon - Y_M + S_k \quad (4.2)$$

The equation for the dissipation rate of turbulent KE (ε) is

$$\frac{\partial \rho \varepsilon}{\partial t} + \frac{\partial(\rho \varepsilon u_j)}{\partial x_j} = \frac{\partial}{\partial x_j} \left\{ \left(\mu + \frac{\mu_t}{\sigma_\varepsilon} \right) \frac{\partial \varepsilon}{\partial x_j} \right\} + \rho C_1 S_\varepsilon - \rho C_2 \frac{\varepsilon^2}{k + \sqrt{\nu \varepsilon}} + C_{1\varepsilon} \frac{\varepsilon}{k} C_{2\varepsilon} G_b + S_\varepsilon \quad (4.3)$$

Where, G_b & G_k is the generation of turbulent KE due to buoyancy effect and mean velocity gradient respectively, $C_1 = \max \left[0.43, \frac{\eta}{\eta+5} \right]$, $\eta = S \frac{k}{\varepsilon}$, and $S = \sqrt{2S_{ij}^2}$, Y_M is

the fluctuating dilation in compressible turbulence to dissipation rate, and S_k & S_ε are user-defined sources. The values of model constants are $\sigma_k = 1.0$, $\sigma_\varepsilon = 1.2$, $C_{1\varepsilon} = 1.44$, and $C_{2\varepsilon} = 1.9$, the values of these constants are estimated by several experiments of turbulent flow and it has found to be valid for a huge range of Reynolds number in the turbulent region.

In a fully developed turbulent flow, the effects of turbulence are directly influenced by the wall on which the fluid is flowing. Consider the flow very close to the wall, the Reynolds number very close to the wall will be,

$$Re_y = \frac{\rho V y}{\mu} \quad (4.4)$$

Where, Re_y is the Reynolds number based on y distance, which is the normal distance from the wall. For the regions very close to wall, $y \sim 0.001$. The Reynolds number will be low and lie in the laminar region, therefore the flow region very close to the wall is called laminar sub-layer. Subsequently, as we move away from the wall, the y value increases and the Reynolds number increases to transition and then to the turbulent region. To assess the turbulence near the wall, the near wall stress can also be represented in the form

$$\tau_w = \rho u_\tau^2 \quad (4.5)$$

Where, u_τ is the friction velocity.

$$u_\tau = \sqrt{\frac{\tau_w}{\rho}} \quad (4.6)$$

Non-dimensional distances are introduced here to understand the behaviour of velocity and distance from the wall very close to the wall, $y \sim 0.001$. The different layers formed very close to the wall are shown in Fig. 4.4.

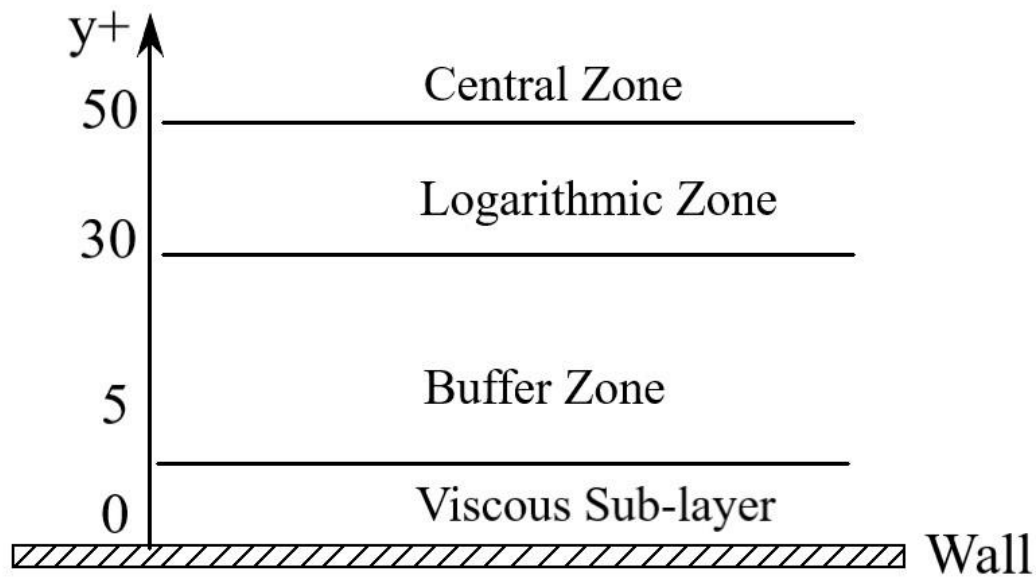


Fig. 4.4 Different layers near turbulence near the wall in hydraulic boundary layer

Fig. 4.4 shows the different layer of layers formed very close to the wall during turbulent flow. To understand the behaviour of these layers and their behaviour with distance & velocity, non-dimensional terms have been defined.

$$u^+ = \frac{V}{u_\tau} \quad (4.7)$$

$$y^+ = \frac{u_\tau y}{\nu} \quad (4.8)$$

1. Viscous Sub-layer: In this zone, viscous forces are dominant and a very thin layer of fluid flows in the laminar region. In this layer,

$$u^+ = y^+ \quad (4.9)$$

Until $y^+ = 5$.

2. Buffer Zone: This zone extends from $y^+ = 5$ to $y^+ = 30$, in this region turbulent kinetic energy has maximum production.
3. Logarithmic Zone: This zone has $y^+ > 30$, a logarithmic profile is followed in this region.

$$u^+ = \frac{1}{\kappa} \ln(y^+) + B \quad (4.10)$$

Where, κ is Karman constant, $\kappa = 0.41$ and $B = 5.5$.

4. Central Zone: For $y^+ > 50$, is the region where the viscous effects of the wall become negligible.

Fig. 4.5. shows the non-dimensional velocity as the function of non-dimensional normal distance from the wall surface, representing the functional relations between the two.

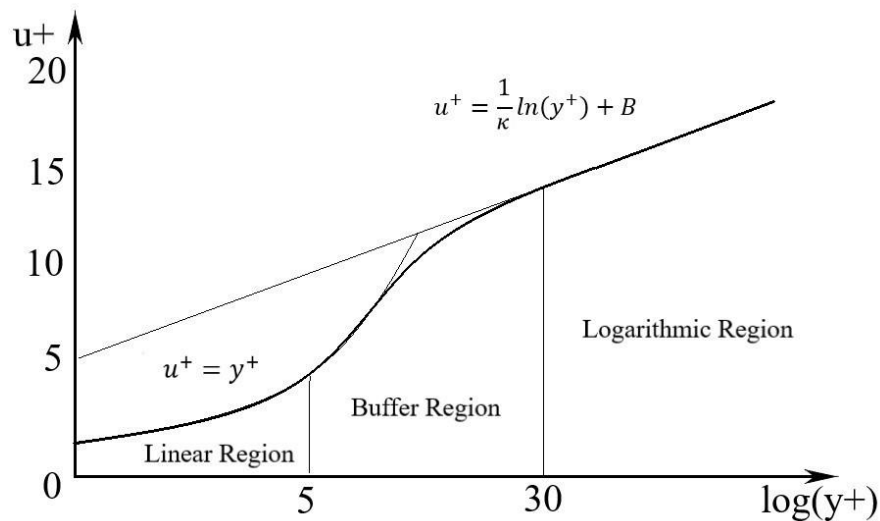


Fig. 4.5 Non-dimensional velocity profile for near the wall

During the mesh generation of a fluid domain for turbulence modelling, special care is required to assess the y^+ value at the fluid-solid wall interface. Choosing a y^+ is directly correlated to region till which one wants to resolve the turbulence modelling. Usually for $k - \epsilon$ model, suitably $30 < y^+ < 100$, this implies that you are resolving the logarithmic layer. Thus, the mesh size near the wall is chosen in such a way that the simulation results the y^+ in this range and this requires some hit & trial to achieve. In the IHX models designed for this thesis, the y^+ values were not coming in the given range hence, the near wall treatment option was chosen. The first mesh size was chosen in such a way that y^+ value for all the cases came out to be less than 5 ($y^+ < 5$). It

implies that for turbulence modelling, laminar sub-layer is also getting resolved without using the wall functions. In Fig. 4.6, y^+ values for 250mm, 500mm, & 1000mm IHX are shown in the form of y^+ contours for different inlet conditions. It is clear that for cases shown the y^+ value at the interfaces are well below 5.

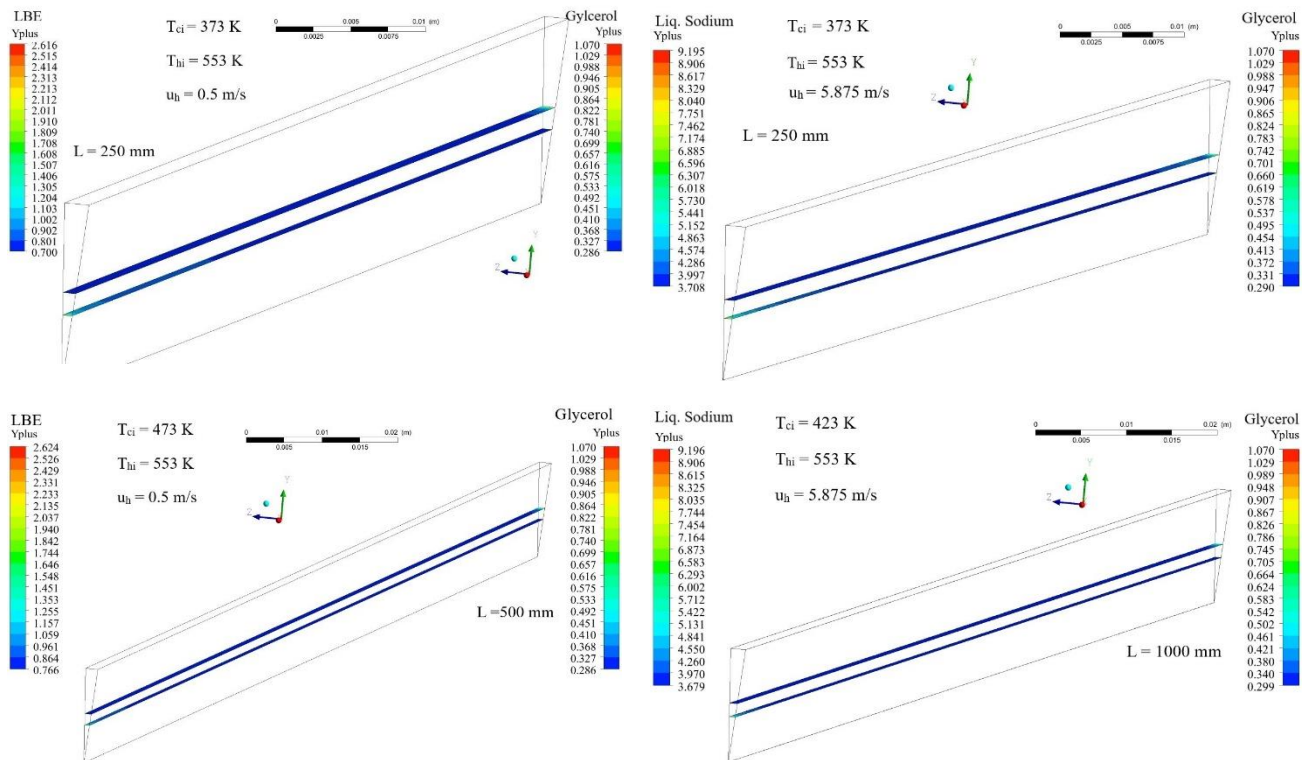


Fig. 4.6 y^+ values for LBE and Liq. sodium for various inlet boundary conditions and length of IHX

4.3. Mesh Formations

Mesh formation is a key aspect of CFD analysis, the Ansys software is used for mesh generation for all of models and cases. The 3D design of the IHX was initially used for the thesis. Fig. 4.7 shows the meshing of the 3-dimensional model of the IHX, general element size was set to 0.75 mm. There are two interfaces in the design, liquid metal-tube interface, and the glycerol-tube interface; for both the interfaces contact

sizing was done with size set to 0.5 mm . At the interfaces, inflation layers were given having 10 layers each with a growth rate of 1.5. This configuration was chosen after performing the grid independence test with 2 million elements. Fig. 4.8 shows the lateral view of the glycerol domain of Y-Z plane, it shows the uniformity by which the mesh was generated. Fig 4.9 shows a close-up look of the meshing, it is representing the inflation layers for both the interfaces very near to the tube walls.

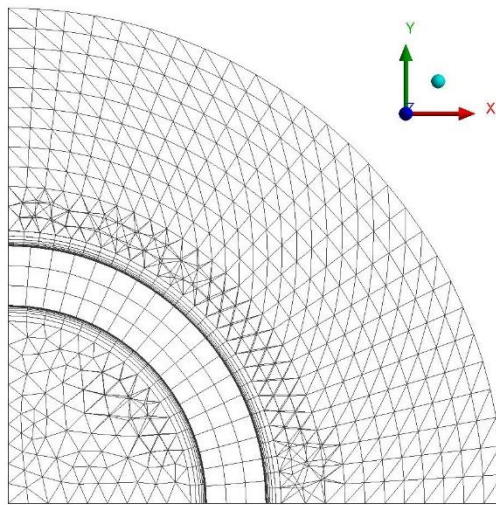


Fig. 4.7 Axial view of Meshing of 3D model of IHX

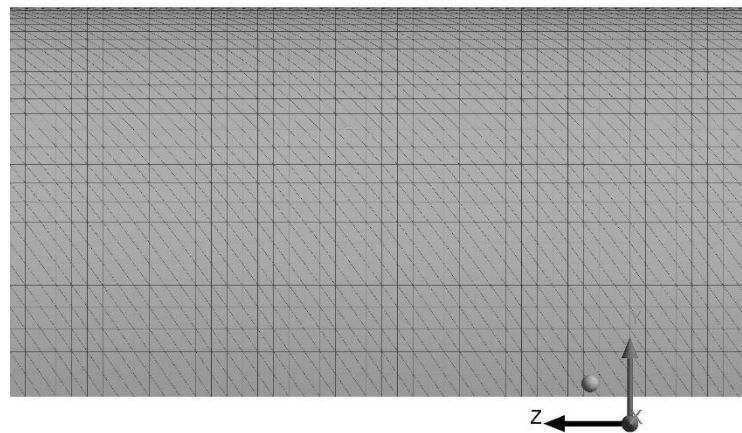


Fig. 4.8 Lateral view of 3D model of IHX showing the uniformity in meshing

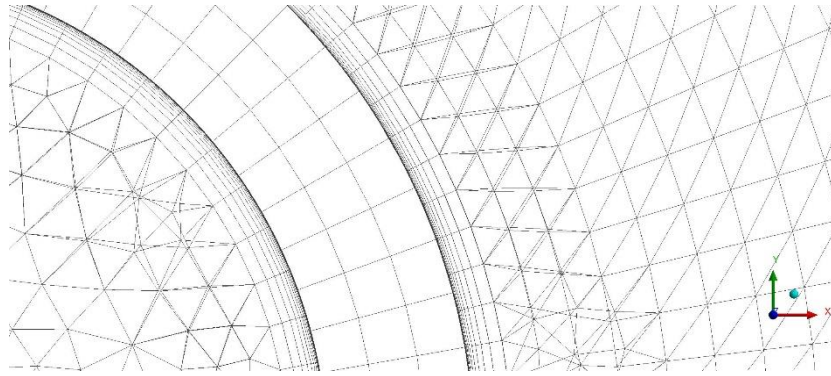


Fig. 4.9 Close up view of Meshing showing inflation region near the fluid-tube interface

Similarly, for the 3-dimensional models of the IHX with fins the general element size was set to 0.75 mm and the contact size at the interface was set to 0.5 mm and inflation layer having 10 layers and growth rate set to 1.5, this configuration resulted in 2.24 million elements. Fig. 4.10 is showing the meshing of the 3-dimensional model of the IHX with 24 fins and 4 mm fin length. Fig. 4.11 shows a close-up view of the meshing clearing showing the inflation layers near the tube walls.

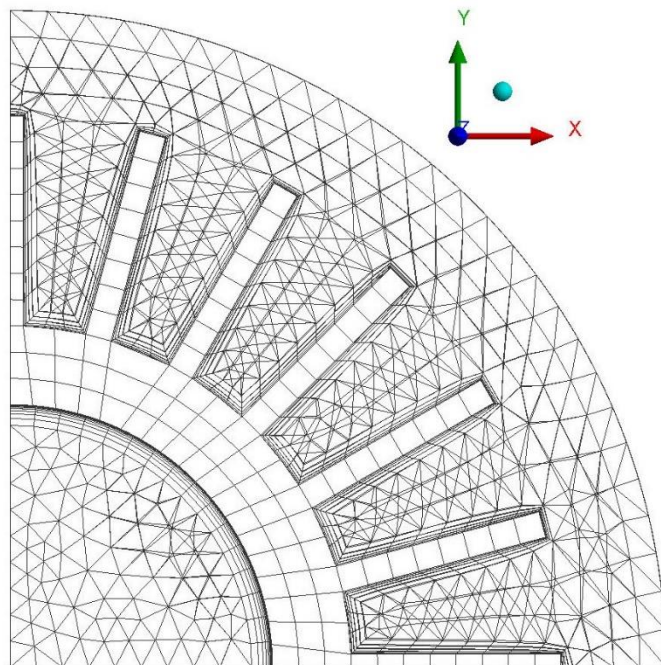


Fig. 4.10 Meshing of 3D model of IHX with fins

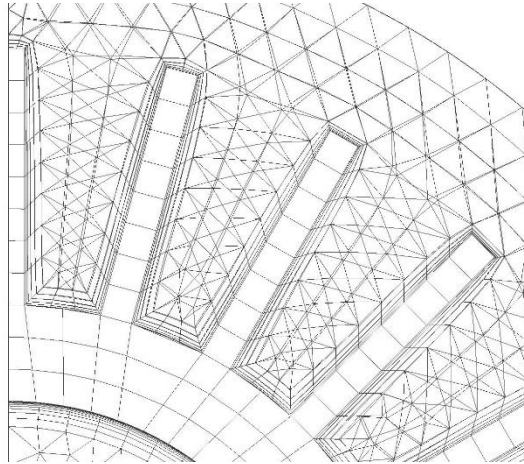


Fig. 4.11 Close up view of Meshing of 3D model of IHX with fins showing the inflation regions near tube walls

Due to the limitations of the computing power of the system, 2-dimensional designs were prepared since solving a model with more than 2 million elements was taking extremely long processing time and the purpose of the thesis would not have been solved with few number of cases of the IHX model. For mesh generation of the 2-dimensional model of the IHX general size of 1.0 mm was chosen and hexahedron type of meshing element was selected which is quadrilaterally shaped in 2-dimensions. Selecting a quadrilateral meshing element resulted in a structured high-quality mesh as shown in Fig. 4.12 which is beneficial for simulations. Biased sizing with biasing ratio of 40 was done near the tube walls to achieve inflation type of growth at both fluid-solid interfaces.

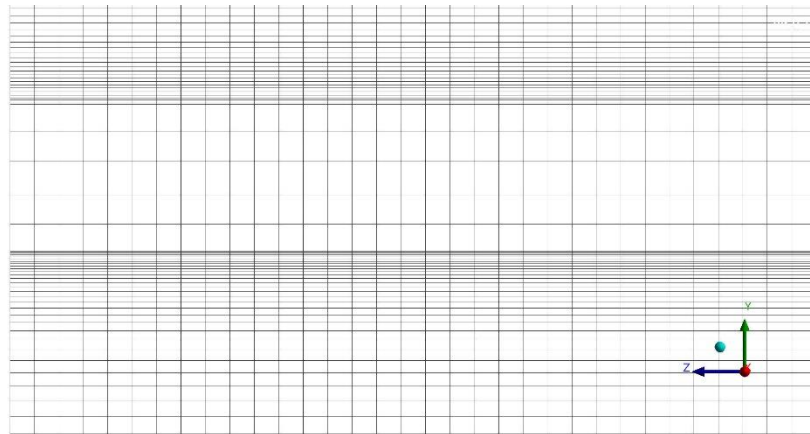


Fig. 4.12 Meshing of 2D model of IHX showing the near wall treatment

4.4. Validation

For analysis of Nusselt number in liquid metals, various studies have been conducted as mentioned in the literature survey section of the thesis. A CFD analysis was performed for a simple tube flow with variation in inlet flow condition of different liquid metals which results in variation of Peclet number. The Nusselt number was recorded for the simulation cases and were compared with previously conducted studies of [5], [24], [41]–[43], [64], [60] & [62]. Fig. 4.13 is showing the variation of Nusselt number computed from present CFD results with increasing Peclet number along with the variation of Nusselt number computed by the correlations developed by [5], [24], [64], [62] for constant heat flux at the tube walls. It can be asserted that the present CFD results are in close proximity with Lyon's [64] & Ibragimov's [5] correlations and are relatively at a distance from the outputs of correlations provided by [24] & [62].

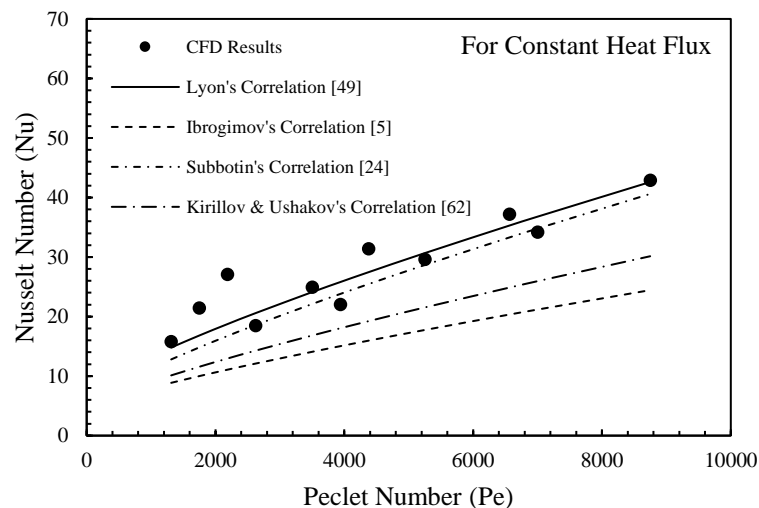


Fig. 4.13 The Nusselt number variation with increasing Peclet number for constant heat flux

Fig. 4.14 is showing the Nusselt number variation with increasing Peclet number for various correlation presented by different authors and present CFD results for isothermal tube wall. The CFD results are varying in close proximity of the

correlations developed by [41]–[43] & [60] and the Nusselt number with the increase in Peclet number.

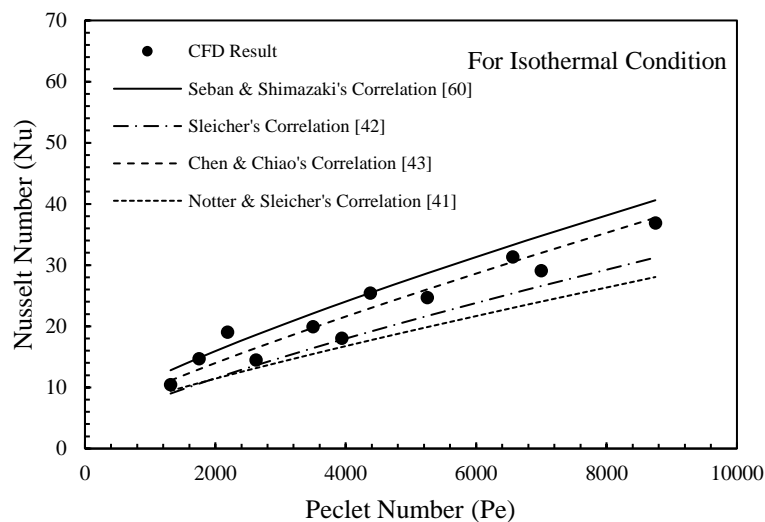


Fig. 4.14 The Nusselt number variation with increasing Peclet number for isothermal tube wall

The study conducted by Mochizuki [33] as mentioned in the literature survey performed CFD analysis on the turbulent flow of mercury and LBE for the same boundary conditions and geometrical parameters as the done by Johnson et al. [50]. The results showed remarkable agreements. A similar validation has been performed in the thesis, [33] used $k - \varepsilon$ turbulent model on a 3D geometry however, in the present case 2D geometry has been used for analysis. The inner diameter of steel pipe is 16.52 mm and the outer diameter is 19.05 mm with an aluminium jacket of thickness 6.35 mm as shown in Fig. 4.15. The Fig. 4.16 shows the meshing of the 2D model used for the CFD analysis showing the respective domains in the model, it is visible that a biased sizing with biasing factor of 40 has been done on the liquid metal-tube interface to mimic the inflation condition. The sizing close to the wall was sufficiently small to maintain the y^+ value below 5 for the fluid-solid interface.

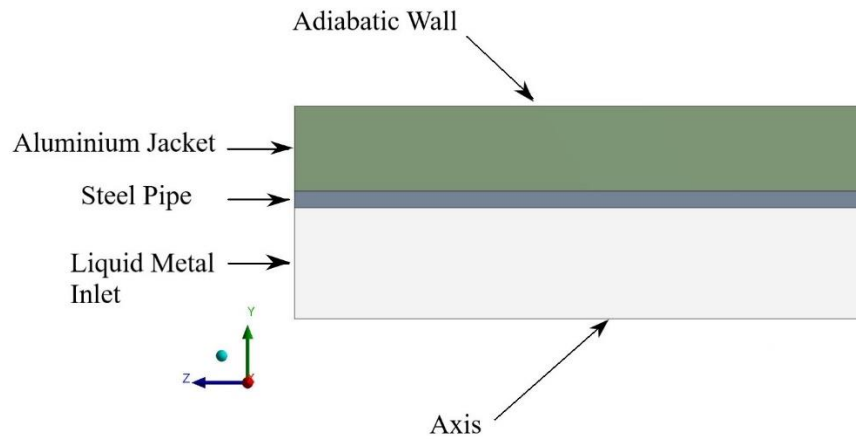


Fig. 4.15 2D model of Johnson's Experiment

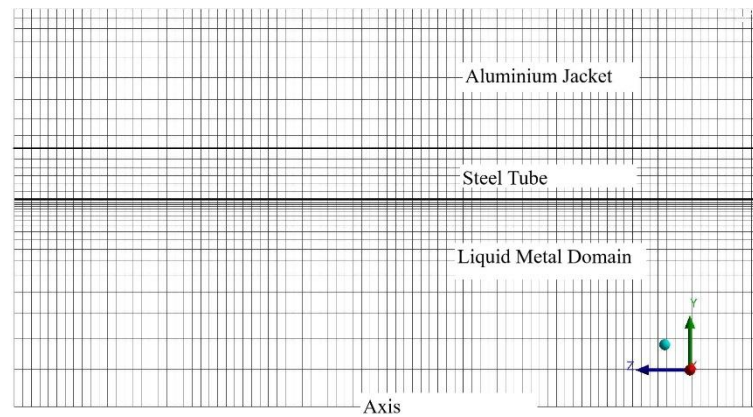


Fig. 4.16 Meshing of 2D model of Johnson's Experiment

Fig. 4.17 and 4.18 show the variation of Nusselt number with Peclet number for present CFD results, Mochizuki's [33] outputs, and the results of Johnson et al. [50] experimental values for Mercury and LBE respectively. It can be positively asserted that computed Nusselt number is over estimated with respect to experimental Nusselt number for both the liquid metals. Moreover, present numerical results are in agreement to results computed by [33]. Hence, it can be outlined that 2-dimensional CFD analysis can be used instead of 3-dimensional for the liquid metal turbulent flow which will inherently save computational time and resources.

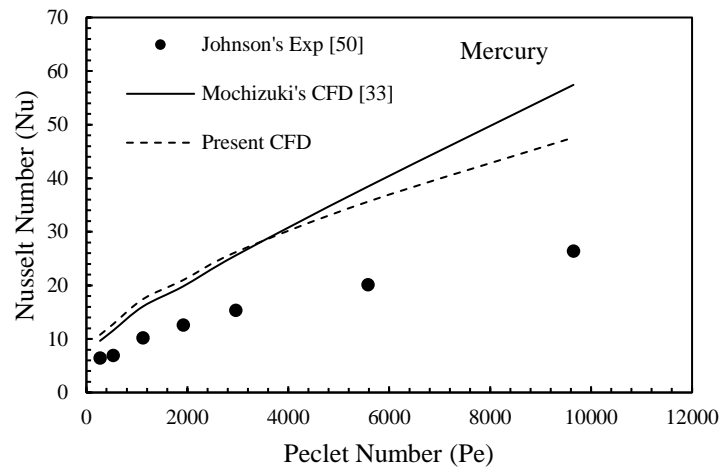


Fig. 4.17 Nu vs Pe for Johnson's [50] and current CFD result with Mochizuki's [33] for Mercury

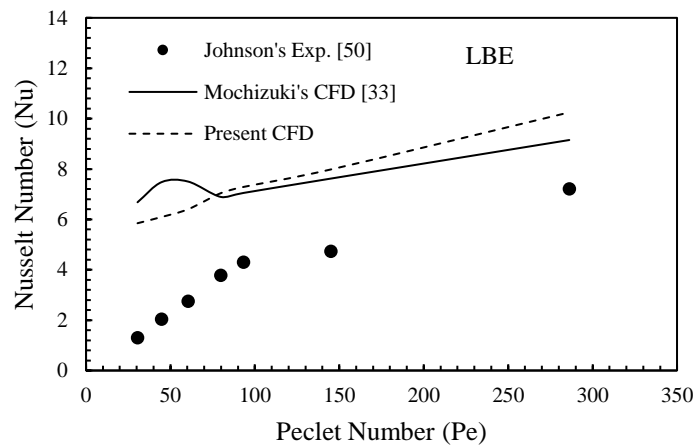


Fig. 4.18 Nu vs Pe for Johnson's [50] and current CFD result with Mochizuki's [33] results for LBE

4.5. Artificial Neural Network Modelling

Machine learning (ML) is a field of computer sciences where the computers are given the ability to “learn” without being explicitly programmed by the user. The term “learn” refers to the ability of a computer to do complex mathematical calculations and store data which is incomprehensible to the human brain and use that data to do

tasks specified by the user such as regression, classification, clustering, association etc. Artificial Neural Network (ANN) is the subset of machine learning sciences where the basic fundamental is derived from the design of a neuron in the brain. Even though the ANN is based upon the brain neurons, the working of it is strictly mathematical.

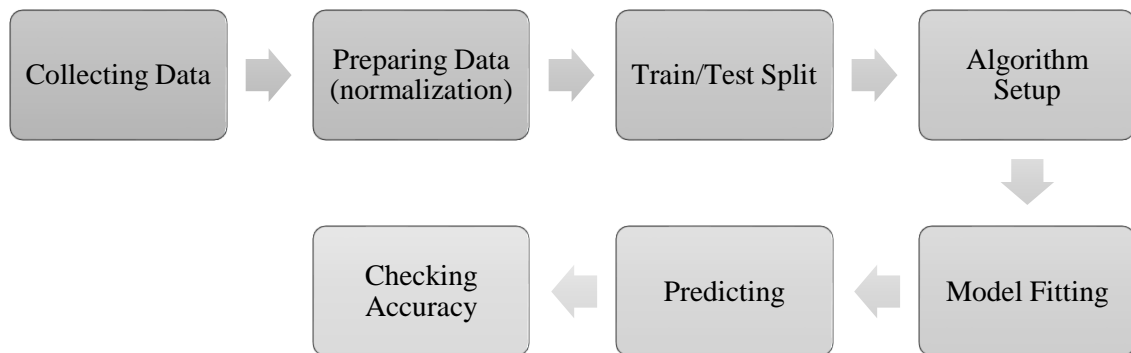


Fig. 4.19 Flow chart showing the steps of artificial neural network programming

Fig. 4.19 is a flow chart showing the steps involved in the programming of a machine learning algorithm or an ANN algorithm. Initially, the raw data is collected from the source which is Ansys Fluent in our case, this raw data is analyzed for any anomaly and discrepancy. Usually, for good outputs the data is normalized, which implies converting the values of each row in form of normal distribution curves, therefore, the values are always in the vicinity of 0. The normalized data is split into two portions: train data and test data. The training data is used by the algorithm for learning and the test data is used for model fitting to check the accuracy of the ANN model. The ANN algorithm is modelled with an appropriate number of nodes and hidden layers to achieve maximum accuracy, which is done on a hit-and-trial basis. Subsequently, the testing data is fed into the system for model fitting, where the algorithm predicts the output corresponding to the input variables and those predictions are then compared with the actual output variables.

Fig. 4.20 shows a neural network chart which is representing layers and nodes which are an essential part of the algorithm. In a deep neural network, each neuron is connected to every other neuron on the next layer and the output neuron is being

connected to every single neuron in the layer before it. The input data is fed to each neuron on the hidden layer in a form of a linear function with weights and bias values.

$$z_{11} = x_1w_{11} + x_2w_{12} + x_3w_{13} + b_1 \quad (4.11)$$

Where, z_{11} is the interim output of 1st node at the 1st hidden layer, x_i are the input variables, w_{ij} show the value of weights in the matrix of $w_{3,5}$ with element of i^{th} row and j^{th} column, and $w_{3,5}$ shows that it is 3 by 5 matrix of real values, and b_1 is the biased values added for balancing the equations.

The neurons in the hidden layer stores these values but the outputs given to the next layer is not in linear form. The Activation functions are used to transform linear functions as shown in 4.11 to non-linear functions which are only used in the hidden layers. This transformation is beneficial for achieving more accuracy during the prediction stage. In this study rectified linear function (ReLU) has been used for activation, the ReLU function is shown below,

$$a = \begin{cases} 0 & \text{if } z < 0 \\ z & \text{if } z > 0 \end{cases} \quad (4.12)$$

Where, $a = 0$, means no activation, and $a = z$ means, linear activation. There are also several types of activation functions which are beyond the scope of this thesis. Coming to the next hidden layer, that a_{ij} becomes the input for the next layer and this process is continued until the output layer. The final value of the predicted output is then compared with the actual output values for those particular input variables. Then, the program calculates the squared error between the predicted and the actual values. This error is “back – propagated” into the network and the values of the weights and biased are altered in such a way that the error is reduced for every next iteration process. These back – propagation iterations are carried out until sufficiently low error values are not achieved or until the user decides it to stop the iterations.

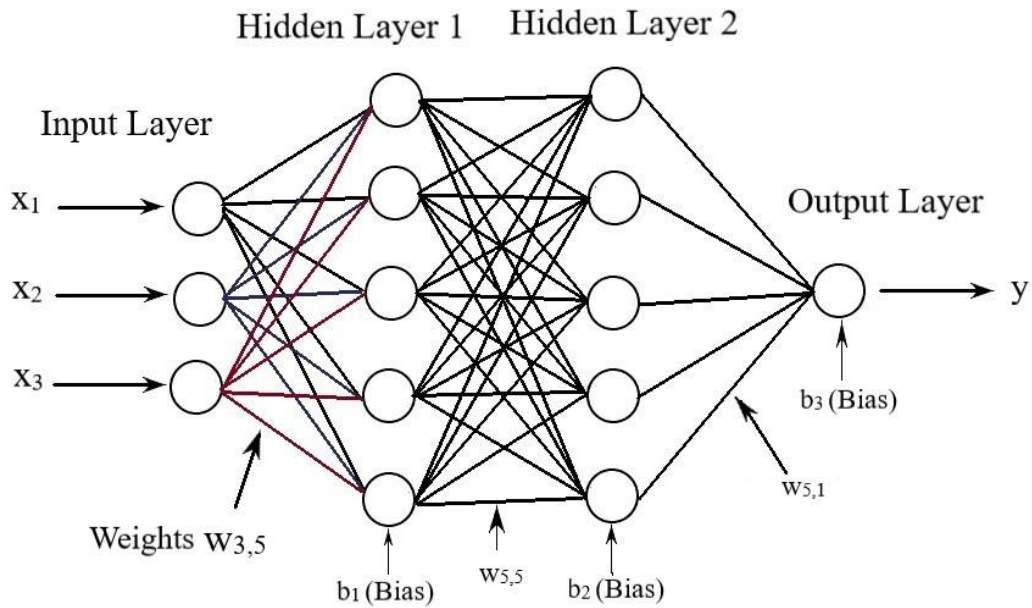


Fig. 4.20 Artificial Neural Network showing the number of layers and nodes

In this thesis, for the analysis of IHX and the data collection was achieved with the variation of input variables like the inlet velocity of liquid metal, inlet temperature of liquid metal, the inlet temperature of glycerol in the annulus region and the length of the IHX. The variation in the inlet condition of liquid metal resulted in the variation of Reynolds number, Prandtl number and the thermal conductivity of the LBE and Liq. sodium. These are referred to as the independent input variables. This resulted in 5 input variables with 180 cases each for both LBE and Liq. sodium. The output was considered to be the overall heat transfer coefficient because it is incorporating the total heat transfer and the LMTD, moreover, it is the most appropriate variable that can be used for quantitative and qualitative assessment of a heat exchanger.

Chapter 5 – Results and Discussion

This chapter contains in-depth analysis of the heat transfer and pressure drop characteristics for turbulent flow in the intermediate heat exchanger. The heat transfer analysis contains the analysis of the thermal boundary layer and density variation in LBE and Liq. sodium during fluid flow in the tube of IHX. In the analysis, the variation of total heat transfer, logarithmic mean temperature difference, and overall heat transfer coefficient with variation in inlet boundary conditions have been depicted in the form of plots and are analyzed & commented upon. The thermophysical properties of liquid metals have been inspected in the CFD analysis. The pressure drop across the tube length has been compared with prior experimental results. A correlation is developed depicting overall heat transfer coefficient as a function of independent variables using GRG technique and ANN algorithm has been employed for regression analysis of the same data, an in-depth comparison of two techniques has also been carried out.

5. RESULTS AND DISCUSSION

In this thesis, a detailed CFD analysis of intermediate heat exchanger designed to be used in the liquid metal cooled nuclear reactor is carried out. The IHX under consideration is double-pipe single pass heat exchanger with liquid metal on the tube side and 100% glycerol on the annulus side. The inlet boundary conditions such as inlet velocity and inlet temperature of liquid metal have been varied, and the inlet temperature of glycerol is also being varied to analyze the impact of these variations on heat transfer and fluid flow characteristics such as total heat transfer, overall heat transfer coefficient, LMTD, and pressure drop.

A 2-dimensional analysis was performed with careful implementation of turbulence modelling. The inlet temperature of glycerol (T_{ci}) was varied from 373 K to 473 K and the inlet velocity (u_c) was fixed at 1.163 m/s. The inlet temperature of liquid metals (T_{hi}) is varying from 553 K to 773 K. There are two liquid metal considered, lead-bismuth eutectic (LBE) with inlet velocity (u_h) varying from 0.5 m/s to 2.0 m/s, secondly Liq. sodium with inlet velocity varying from 5.875 m/s to 23.5 m/s. The inlet velocities are chosen in order to maintain an equal mass flow rate for both liquid metals at the inlet temperature of 553 K. The overall analysis of the IHX is performed for three lengths, 250, 500, & 1000 mm, to capture the effect of the variation of tube length on the performance parameters of IHX.

Fig 5.1 – 5.3 are depicting the thermal boundary layer and the variation of density along the tube length. The lower contour is the temperature variation of the liquid metal under steady-state heat transfer condition which is a mirror image of the actual contour of the cross-section and the upper contour is the density variation

corresponding to the bulk temperature because the density is the function of the bulk temperature of the liquid metal. Fig. 5.1 shows the plumes for IHX length of $L = 250 \text{ mm}$ for Liq. sodium with $u_h = 5.875 \text{ m/s}$ and inlet temperature of $T_{hi} = 553 \text{ K}$ for $T_{ci} = 373 \text{ K}$ & 423 K respectively. For these configurations the total rates of heat transfer are $Q = 3631.26 \text{ W}$ & 2613.49 W , the decrease in Q is due to the decrease in the inlet temperature difference which in turn is decreasing the LMTD.

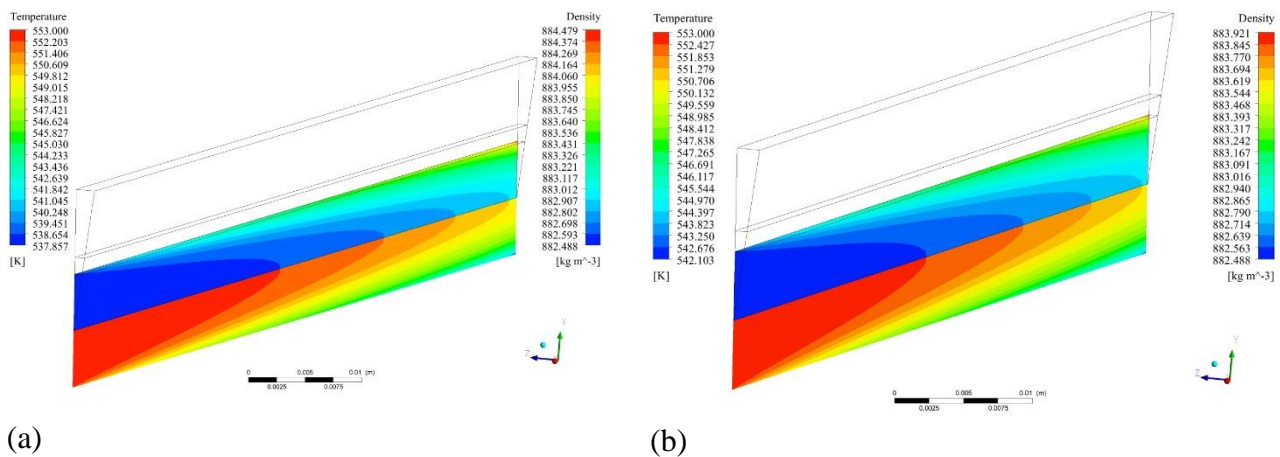


Fig. 5.1 Thermal boundary layer & density variation for Liq. Na with $L=250\text{mm}$

Similarly, Fig. 5.2 & 5.3 are showing the thermal boundary layer and density variation for LBE and Liq. sodium at 500 mm and 1000 mm tube lengths respectively with a similar pattern as observed in Fig. 5.1. Fig. 5.2 shows the contours for IHX of length $L = 500 \text{ mm}$ for LBE with $u_h = 0.5 \text{ m/s}$ and inlet temperature of $T_{hi} = 553 \text{ K}$ for $T_{ci} = 373 \text{ K}$ & 423 K respectively and the total rate of heat transfer being $Q = 6845.98 \text{ W}$ & 4944.18 W . Fig. 5.2 shows the contours for IHX of length $L = 1000 \text{ mm}$ for Liq. sodium with $u_h = 5.875 \text{ m/s}$ and inlet temperature of $T_{hi} = 553 \text{ K}$ for $T_{ci} = 373 \text{ K}$ & 423 K respectively and the total rate of heat transfer is $Q = 13343.7 \text{ W}$ & 9608.66 W , the decrement in the Q is due to the decrease in LMTD.

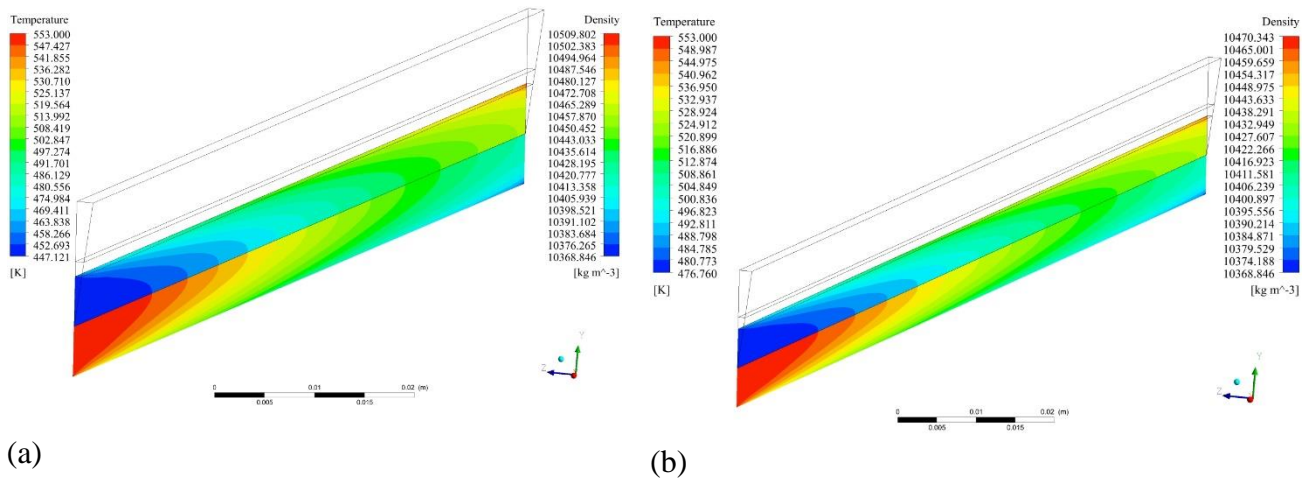


Fig. 5.2 Thermal boundary layer & density variation for LBE with $L=500\text{mm}$

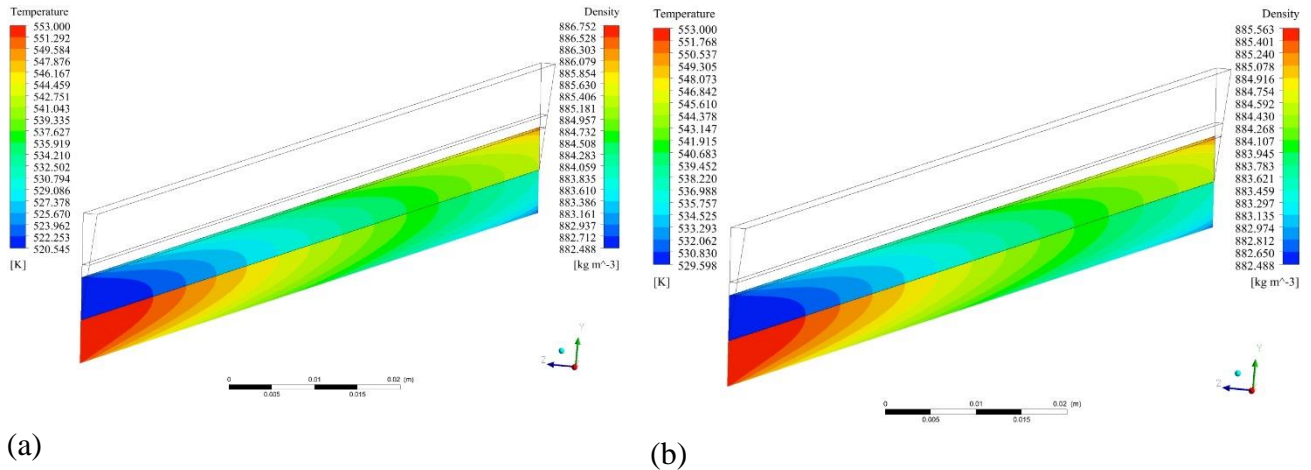


Fig. 5.3 Thermal boundary layer & density variation for Liq. Na with $L=1000\text{ mm}$

Fig. 5.4 & 5.5 are showing the thermal boundary layer for glycerol flowing in the annulus region of the IHX. Fig. 5.4 is showing the temperature plume for IHX of $L = 250\text{ mm}$ for LBE and Liq. sodium respectively with $T_{hi} = 553\text{ K}$ and $T_{ci} = 373\text{ K}$ and Fig. 5.5 is for IHX of $L = 1000\text{ mm}$ with $T_{hi} = 553\text{ K}$ and $T_{ci} = 423\text{ K}$. The thermal boundary layer for glycerol is very thin as compared to LBE or Liq. sodium due to its low thermal diffusivity making it ideal for extracting a large amount of thermal energy from the hot fluid which is in this case is liquid metals.

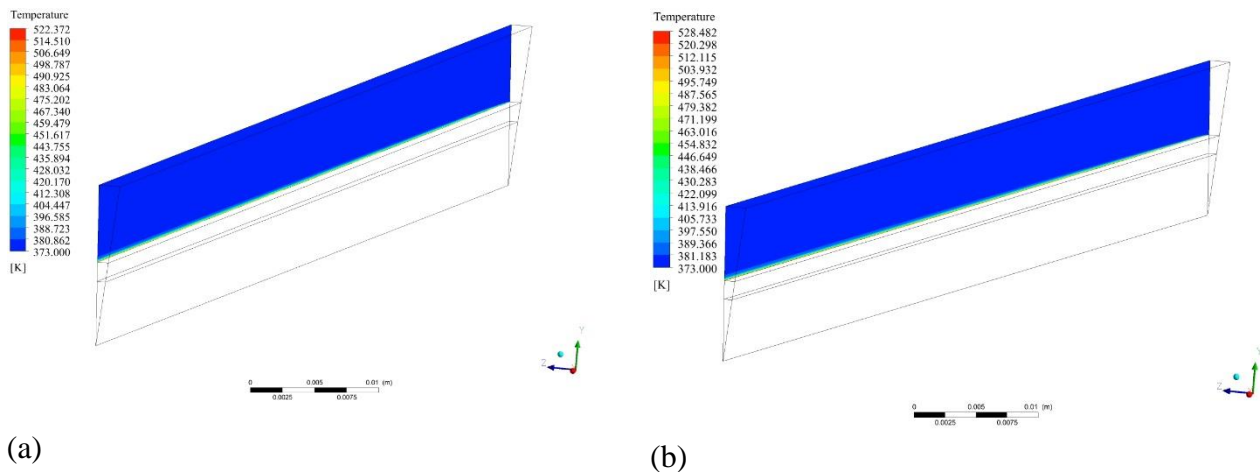


Fig. 5.4 Thermal boundary layer of Glycerol for $L=250\text{mm}$ for a) LBE b) Liq. Na

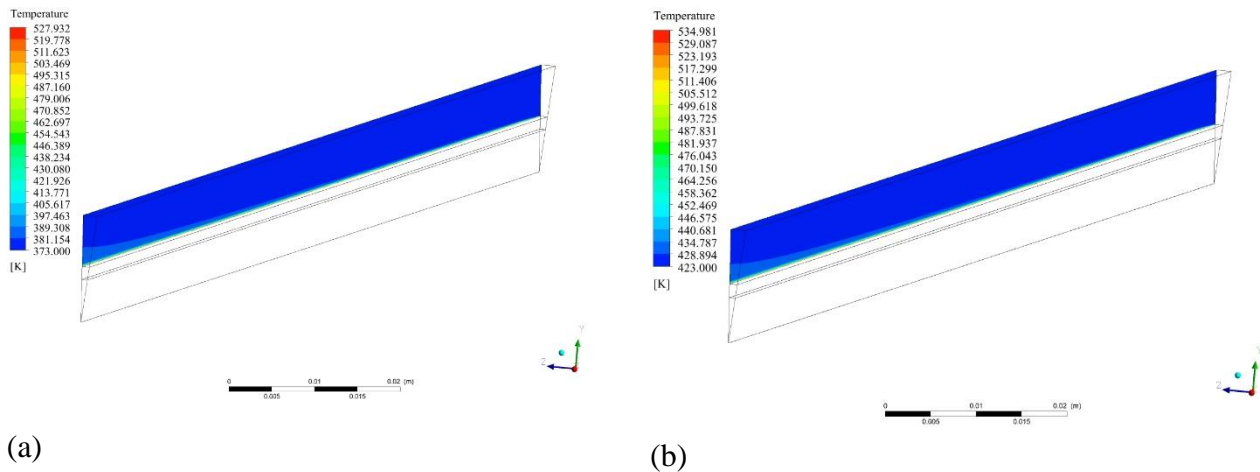


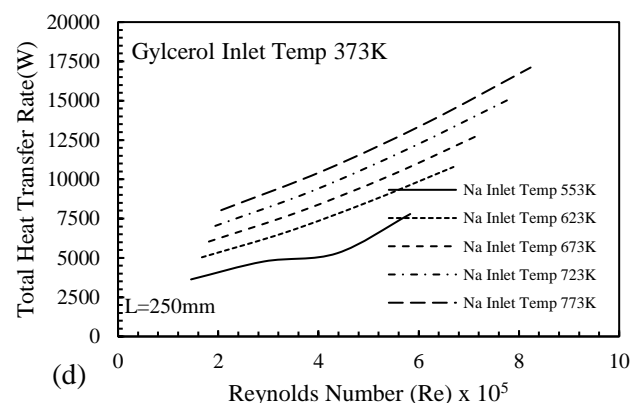
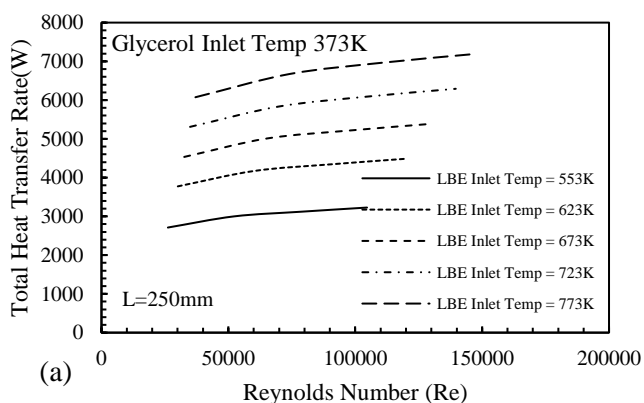
Fig. 5.5 Thermal boundary layer of Glycerol for $L=1000\text{mm}$ for a) LBE b) Liq. Na

5.1. Effect of Reynolds Number

The performance of a heat exchanger is measured by the total heat load, the heat load is the total rate of heat transfer achieved by the HX under steady-state conditions. The heat transfer in IHX is directly related to the Reynolds number of the working fluids, however, in this case, the Reynolds number for glycerol in annulus region is kept constant while the Reynolds number of the liquid metals have been varied to observe

its effects on the total rate of heat transfer. Fig. 5.6 is showing the variation of total rate of heat transfer with increasing Reynolds number for different glycerol inlet temperature and different inlet temperatures for LBE and Liq. sodium for IHX of length $L = 250 \text{ mm}$. The highest rate of heat transfer for IHX of length 250 mm for LBE is 7195.52 W & for Liq. sodium is 17109.2 W and both were achieved at $T_{hi} = 773 \text{ K}$, $T_{ci} = 373 \text{ K}$ with an inlet velocity of 2.0 m/s & 23.5 m/s respectively. Moreover, for these same inlet conditions, the highest rate of heat transfer for IHX of length 500 mm with LBE is 13269.4 W and with Liq. sodium is 32558.6 W , and for the IHX of length 1000 mm , the highest Q for LBE is 23296 W and for Liq. sodium highest value is 61329.3 W .

Fig. 5.7 and 5.8 are showing the same variations for $L = 500 \text{ mm}$ & 1000 mm respectively. It can be observed from the plots that for LBE, the Q is increasing with the increase in Reynolds number up to a certain value and then it is on the verge of becoming constant, this implies if we furthermore increase the flow rate of LBE, the increment in the total heat transfer will be negligible but pumping power will substantially increase, making the functioning of the IHX expensive. For the Liq. sodium, it can be seen that the rate of heat transfer is increasing with the increase in Reynolds number. Thus, the heat transfer rate can be further increased by increasing the flow rate of the Liq. sodium, but with subsequent increase in pumping power an optimized value can be achieved for adequate heat transfer rate.



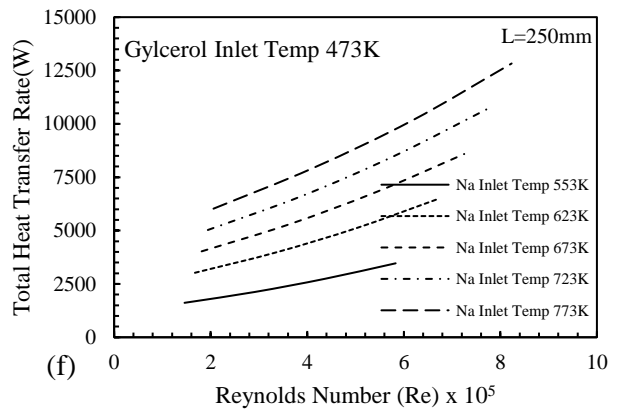
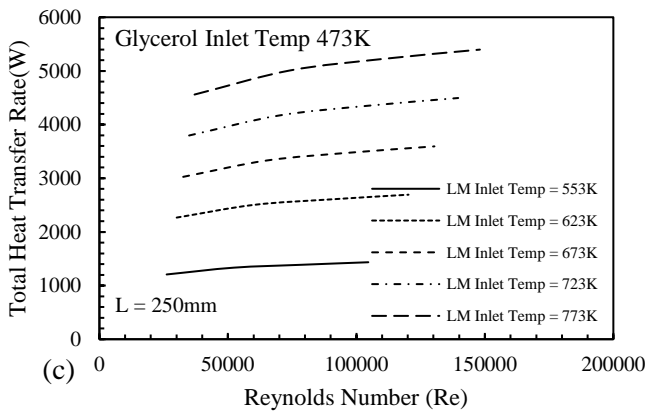
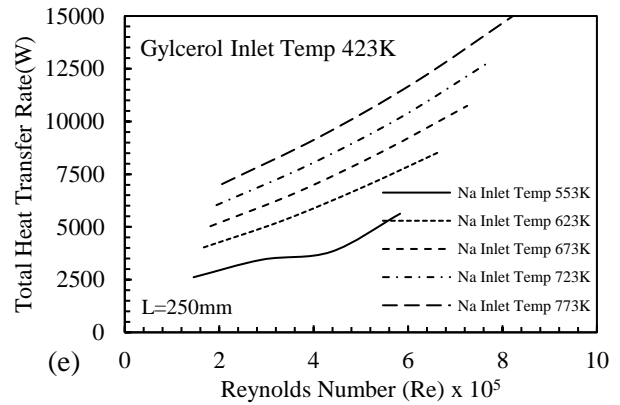
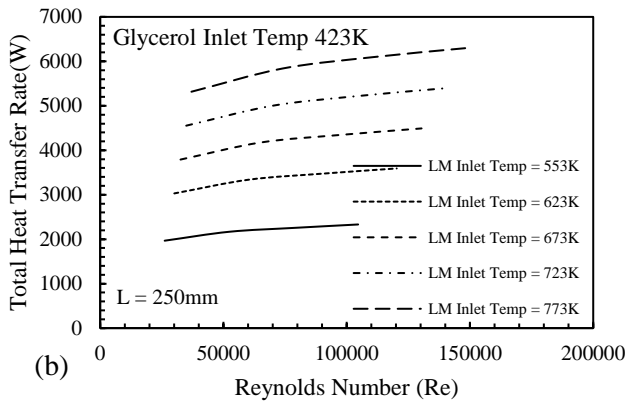
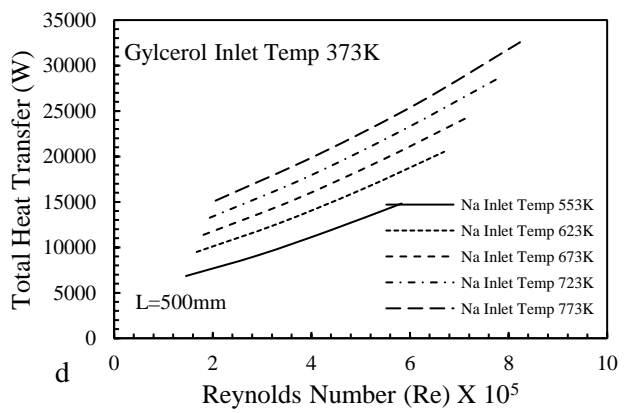
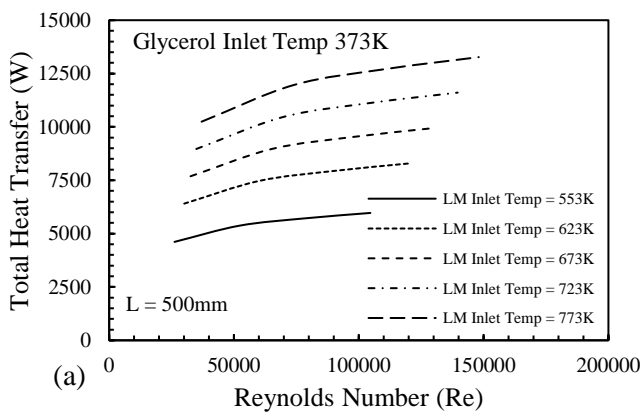


Fig. 5.6 Variation of total rate of heat transfer with increasing Reynolds number for L=250mm for various inlet conditions



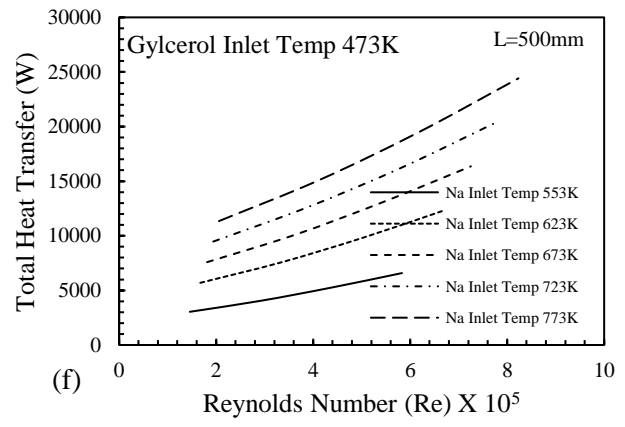
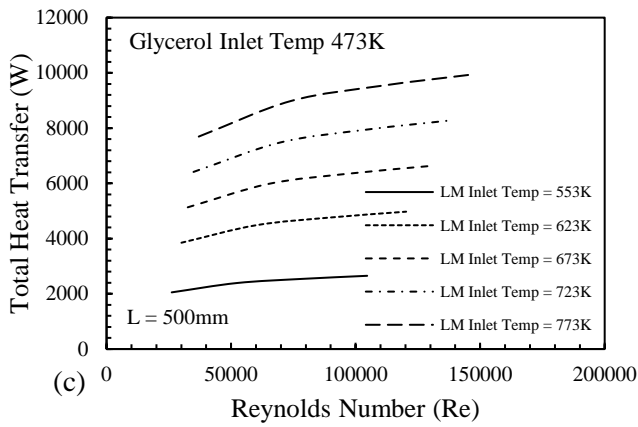
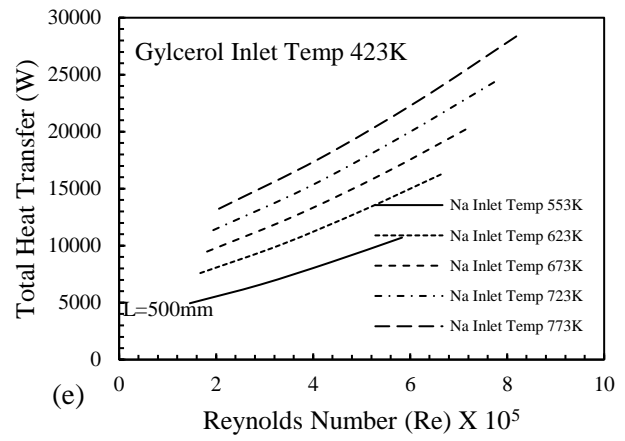
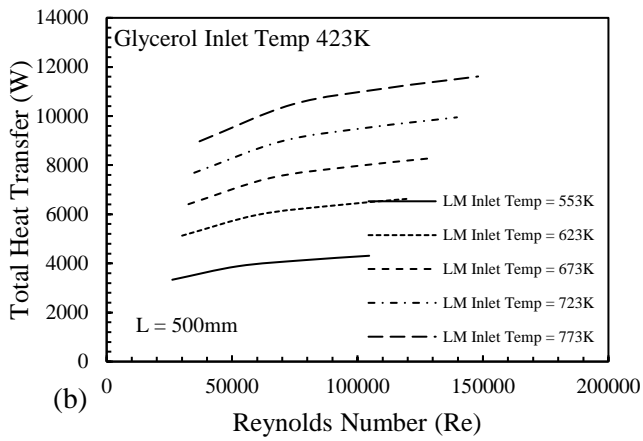
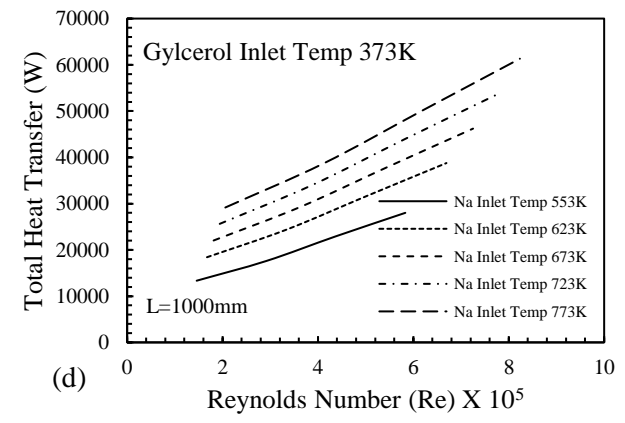
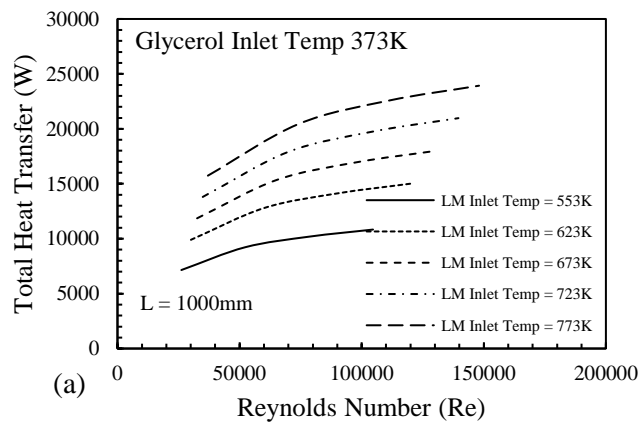


Fig. 5.7 Variation of total rate of heat transfer with increasing Reynolds number for $L=500\text{mm}$ for various inlet conditions



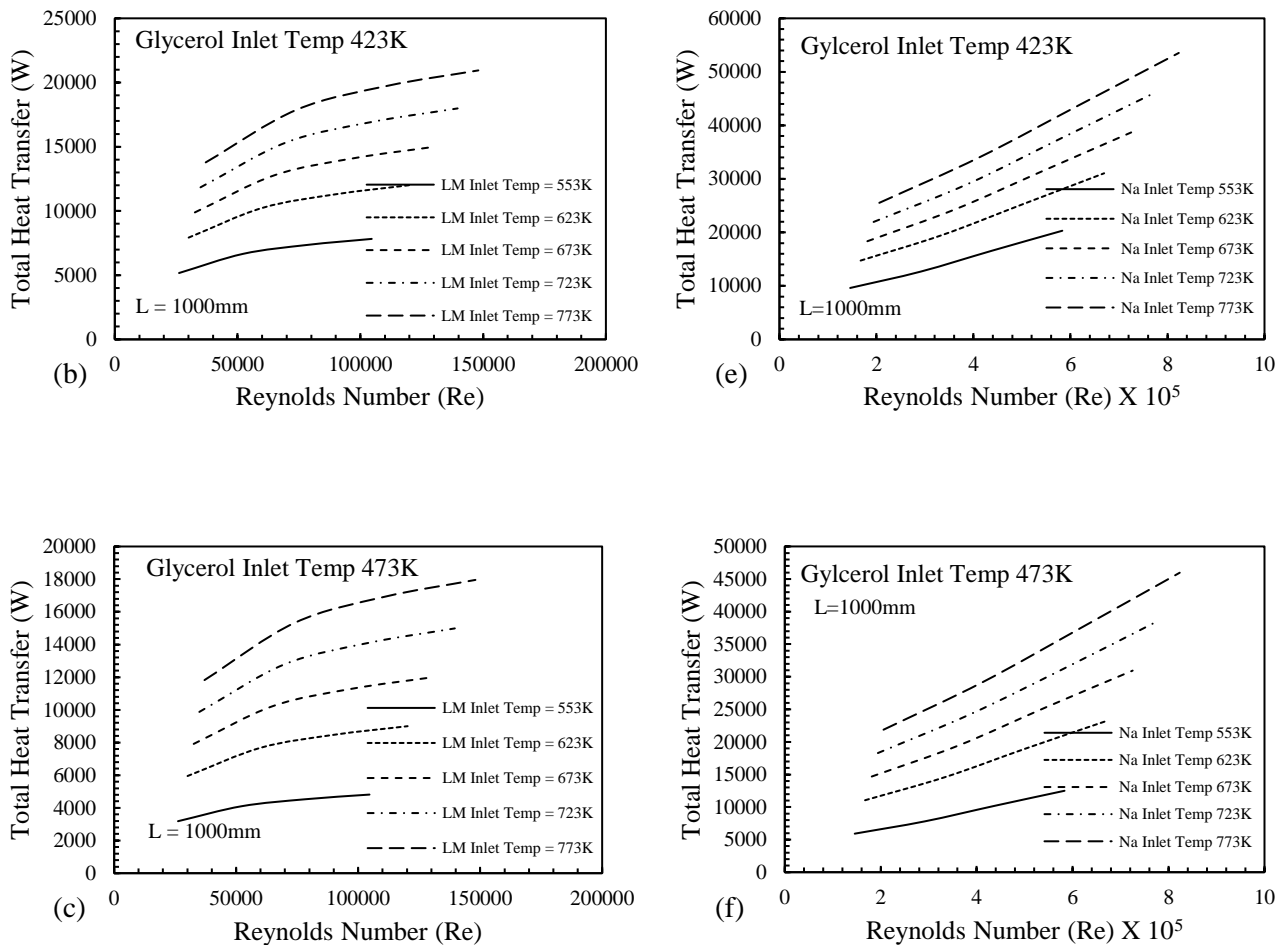


Fig. 5.8 Variation of total rate of heat transfer with increasing Reynolds number for $L=1000\text{mm}$ for various inlet conditions

Pressure drop is directly related to the pumping power; therefore, its optimization is of great significance. As designers, it is preferable to minimize the pumping power and maximize the rate of heat transfer, this problem is categorized as multi-modal optimization problem. Multi-objective optimization is quite complex and is thus avoided in this thesis. However, an analysis of pressure drop and its variation with Reynolds number is observed for LBE and Liq. Sodium for the three lengths of the IHX.

Friction pressure drop for LBE and Liq. sodium for IHX lengths of 250, 500, & 1000 mm have been observed for various inlet temperatures. The frictional pressure drop depends on the Reynolds number and the surface roughness of the tube. In this study, 316L stainless steel is chosen which has a surface roughness of

$\epsilon_R = 0.015 \text{ mm}$. In Fig. 5.9, the skin friction coefficient computed by CFD results is being compared with the skin friction coefficient calculated by Moody's correlation [19] (Eq. 3.65) and Colebrook's correlation [20] (Eq. 3.63). Fig. 5.9 a) is depicting the variation of skin friction coefficient with increasing Reynolds number for LBE inlet temperature of 553 K . Fig. 5.9 b) is depicting the variation of skin friction coefficient with the variation of the Reynolds number along with the values calculated by the correlations (Eq. 3.63 & 3.65). The CFD results in comparison to the correlation results show moderate agreement which is acceptable since the correlations are developed by experimental results that are subjected to different conditions.

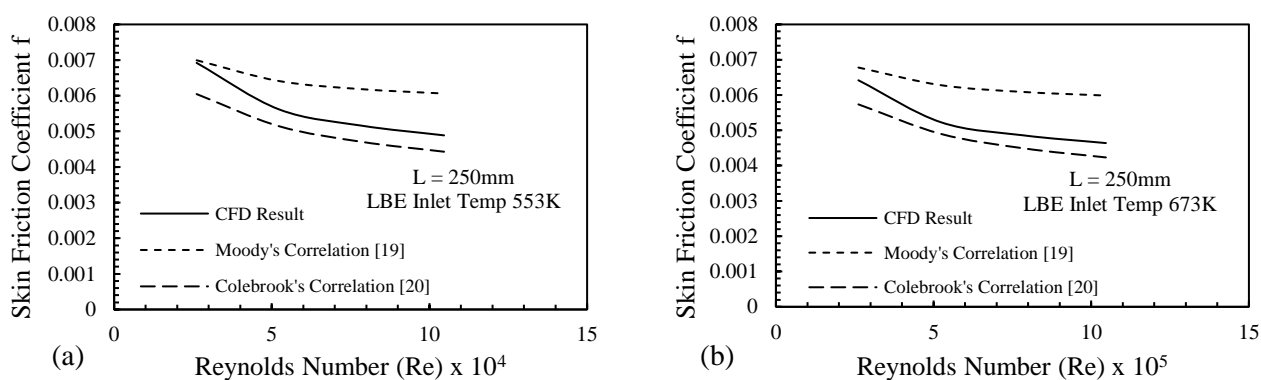


Fig. 5.9 Skin friction coefficient as the function of the Reynolds number

Fig. 5.10 is showing the variation of pressure drop in the tube for lengths 250 mm , 500 mm , & 1000 mm of the IHX with LBE and Liq. sodium for various inlet temperatures of liquid metal. For all the cases of LBE, Fig. 5.10 a), b), and c), the pressure drop is increasing with the increase in Reynolds number and the CFD results being in between the two presented correlations. For lower values of the inlet temperature, the CFD results are overlapping with the pressure drops computed by the Moody's correlation. For the cases of Liq. sodium, the CFD results are conclusively much closer to the results computed by the Colebrook's correlation. However, there is an anomaly in the outcomes for the Liq. sodium with $T_{hi} = 553 \text{ K}$ for $L = 1000 \text{ mm}$, there is an observable deflection from the set pattern that was observed in the other plots.

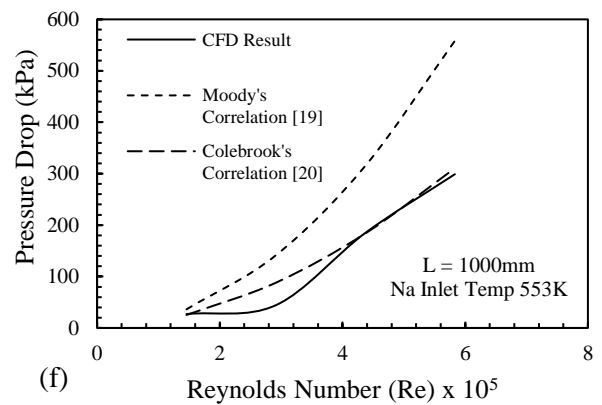
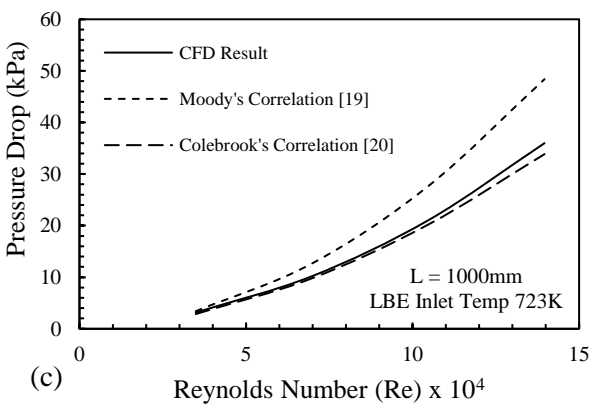
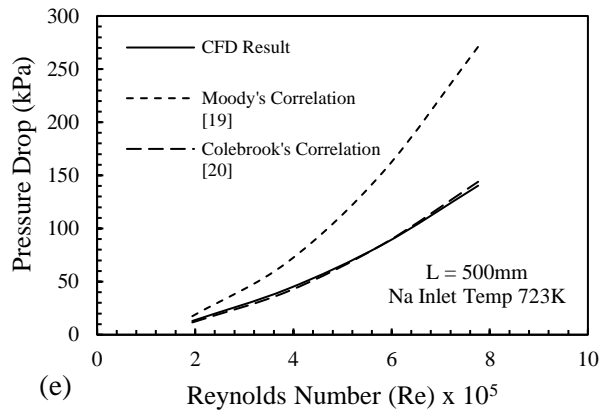
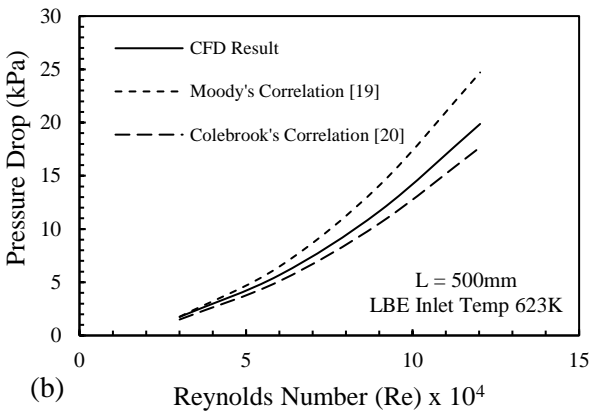
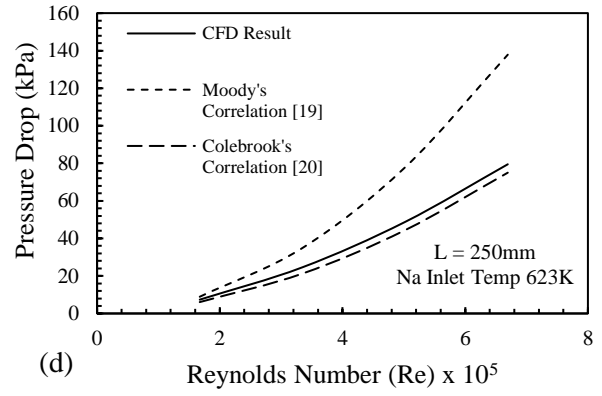
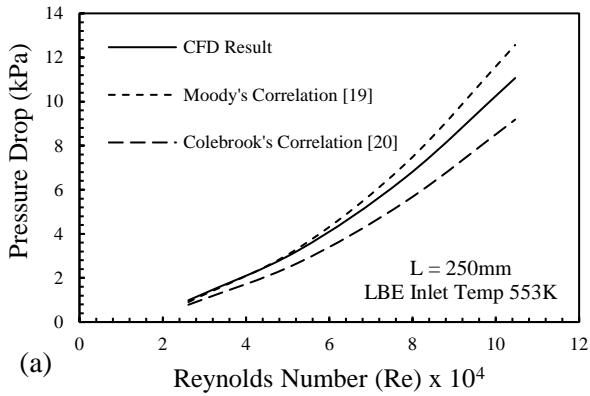
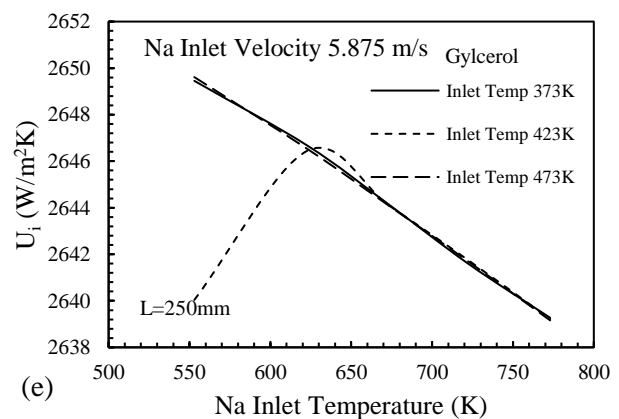
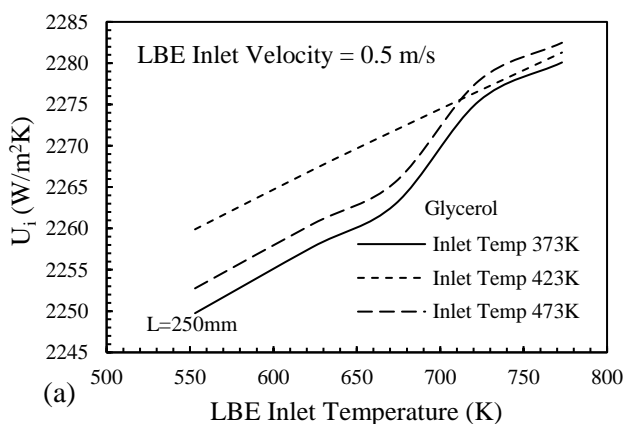


Fig. 5.10 Pressure Drop variation with increasing Reynolds number for various IHX lengths and inlet temperatures

5.2. Effect of Inlet Temperature

Overall heat transfer coefficient is the thermal performance characteristic which deals with the size of the HX along with the heat load, therefore, it is considered to be the key designing and comparison parameters between different type of heat exchangers. The overall heat transfer coefficient is analogous to the convective heat transfer coefficient, taking into the fact that dimensional units are the same. Overall heat transfer coefficient ascertains the performance of heat exchangers just like the Convective heat transfer coefficient shows the performance of heat transfer in single-phase fluid.

Fig. 5.11, 5.12, and 5.13 are showing the variation of overall heat transfer coefficient (U) with the increasing inlet temperature of the liquid metals (T_{hi}) having different inlet velocities for IHX of length 250 mm, 500 mm, and 1000 mm, for different inlet temperatures of glycerol. It can be asserted that the overall heat transfer coefficient for LBE is relatively insensitive towards change in the inlet velocity, however, for Liq. sodium, the overall heat transfer coefficient is substantially increasing with the increase in the inlet velocity.



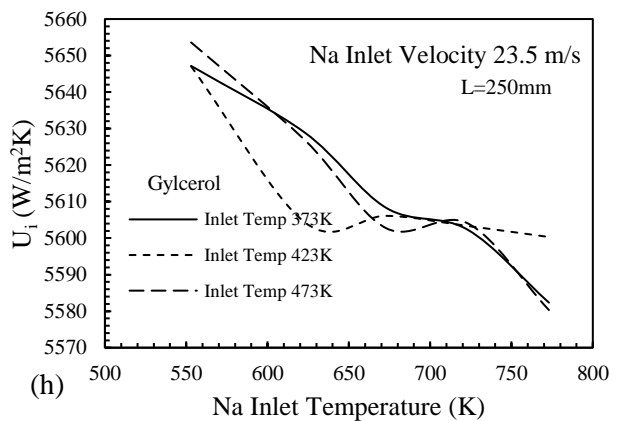
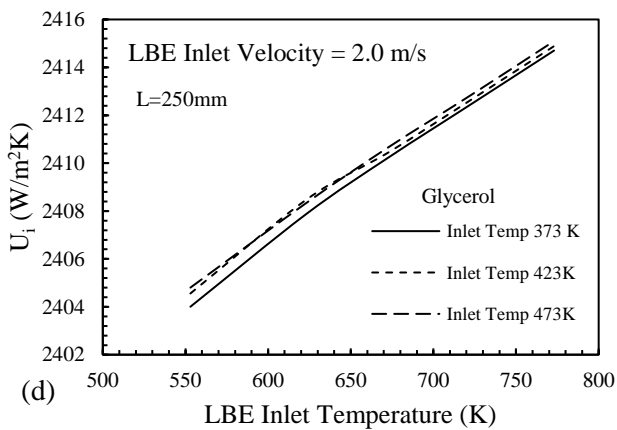
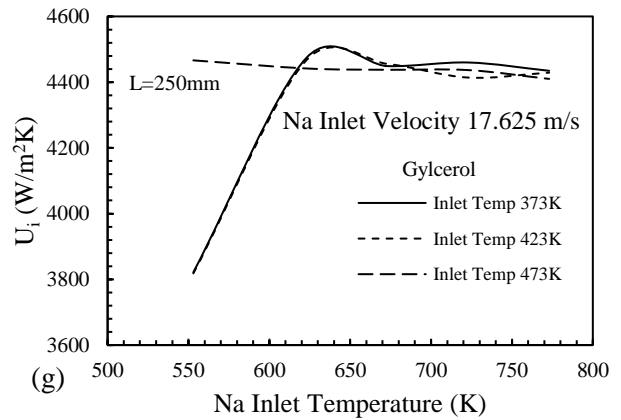
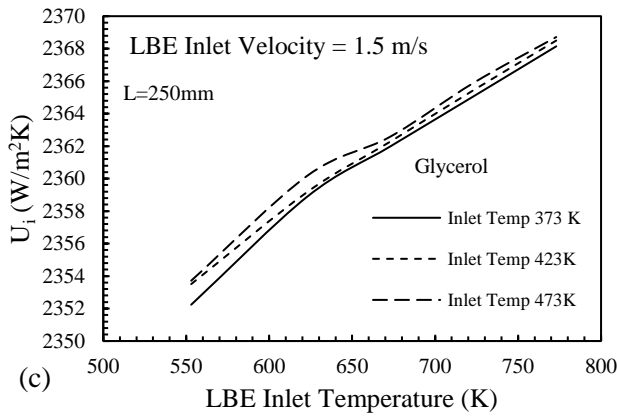
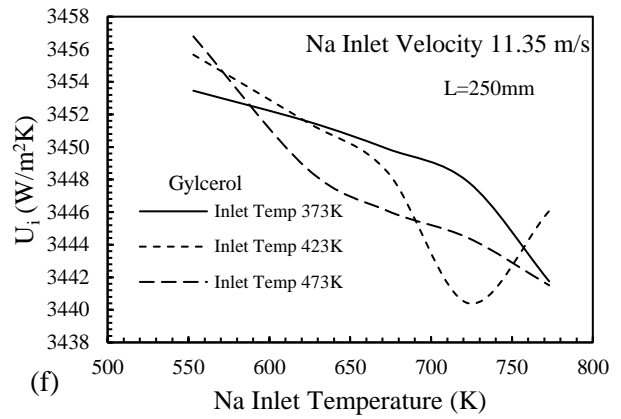
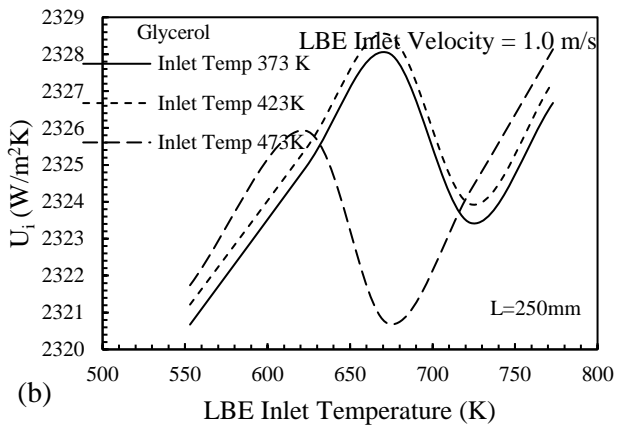


Fig. 5.11 Variation of overall heat transfer coefficient with inlet temperature of liquid metals for L = 250mm

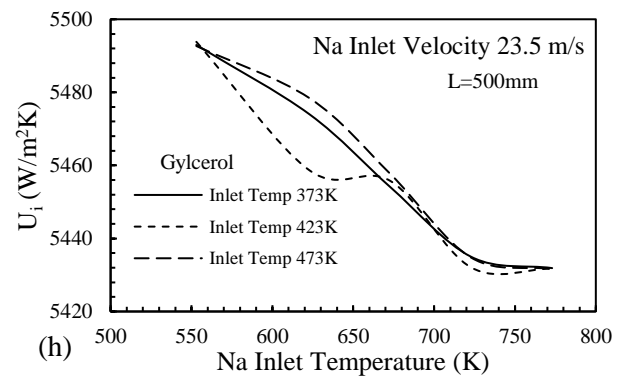
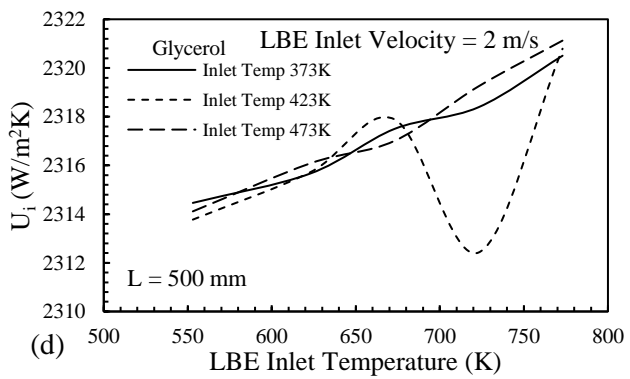
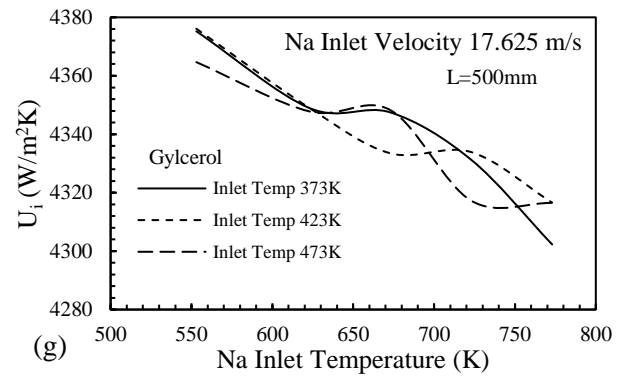
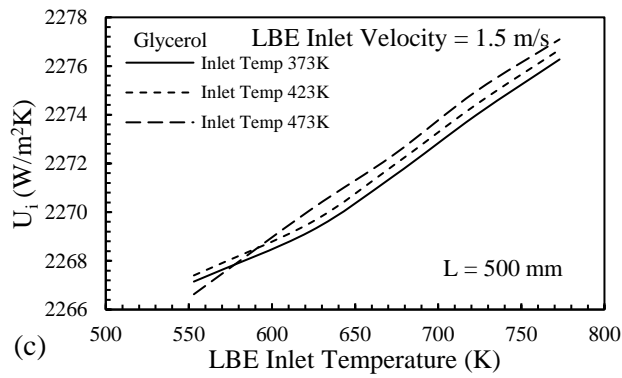
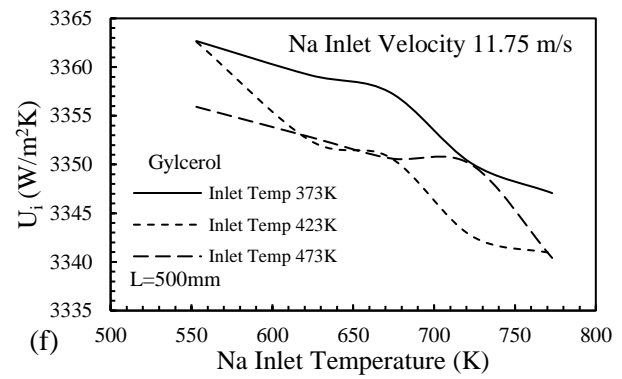
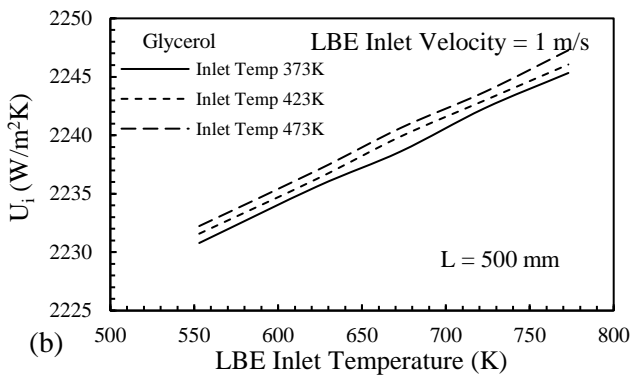
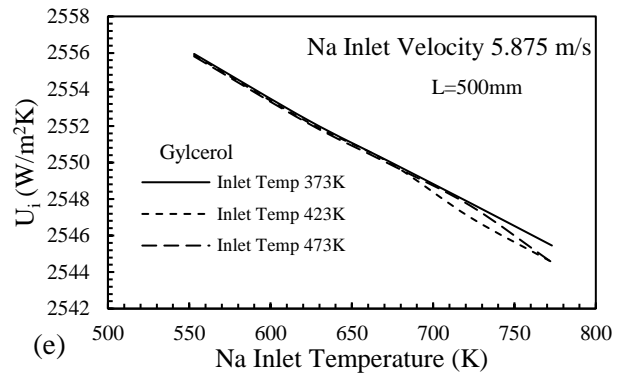
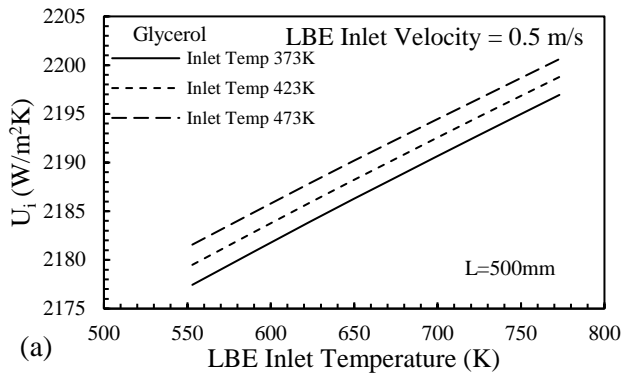


Fig. 5.12 Variation of overall heat transfer coefficient with inlet temperature of liquid metals for L = 500mm

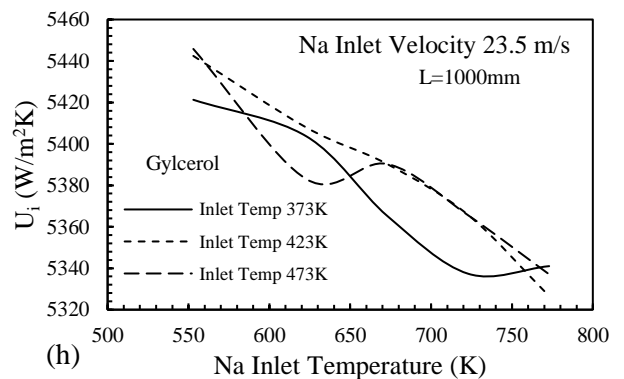
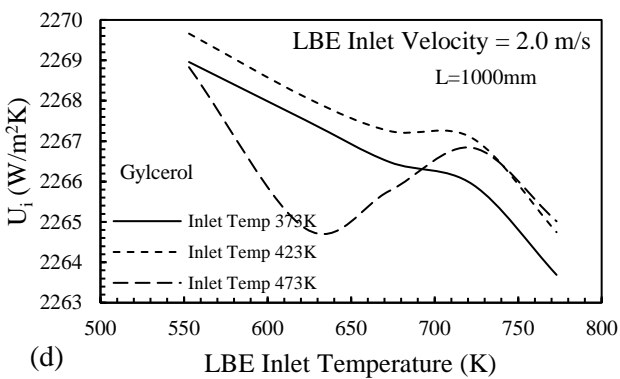
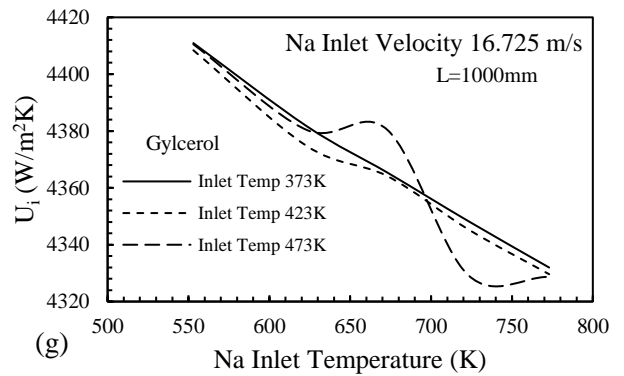
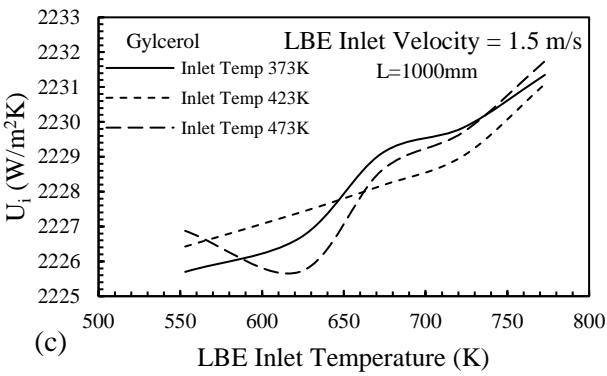
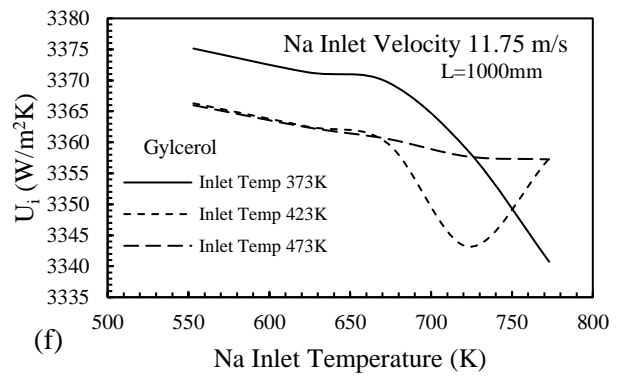
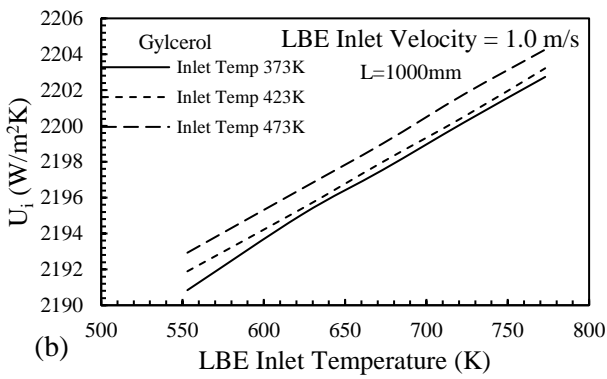
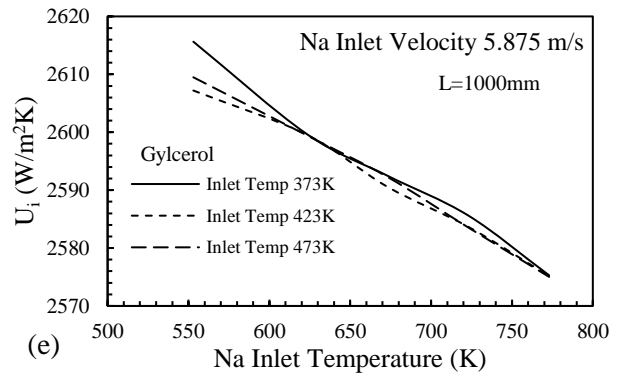
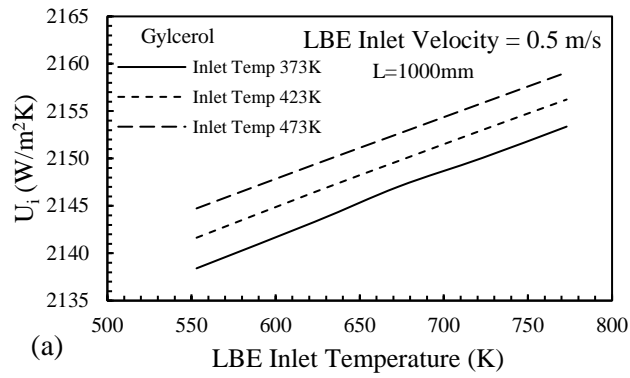


Fig. 5.13 Variation of overall heat transfer coefficient with inlet temperature of liquid metals for L = 1000mm

From Fig. 5.11, 5.12, and 5.13, it can be observed that for LBE the overall heat transfer coefficient is increasing with the increase in inlet temperature. However, for Liq. sodium, U is generally decreasing with the increase in inlet temperature. This general trend was found for all inlet velocities and all inlet temperature of glycerol.

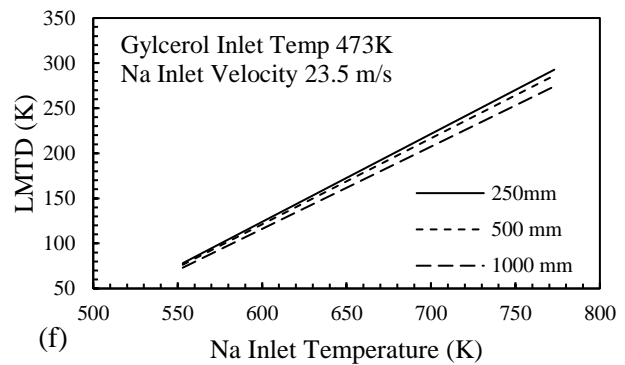
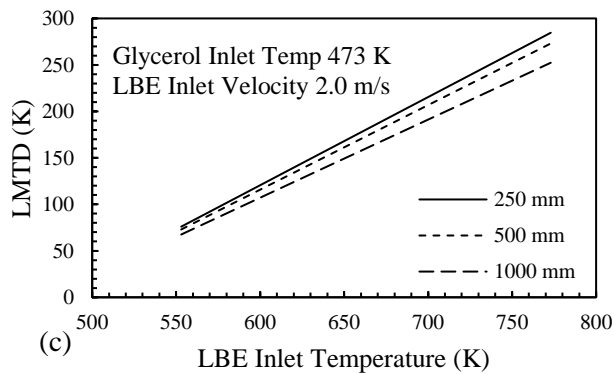
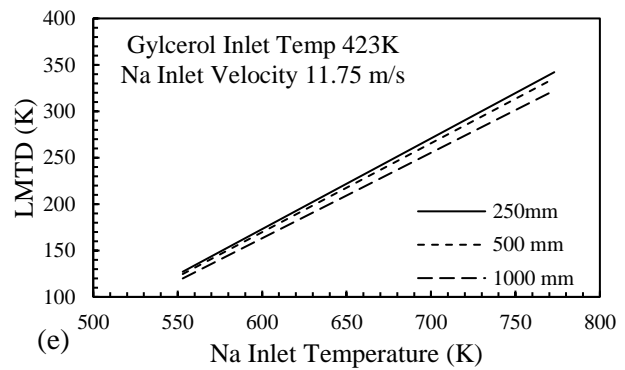
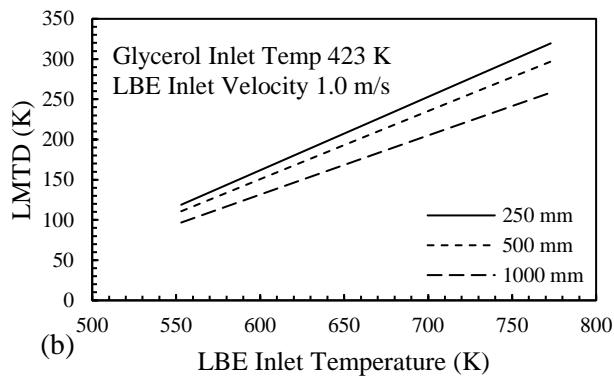
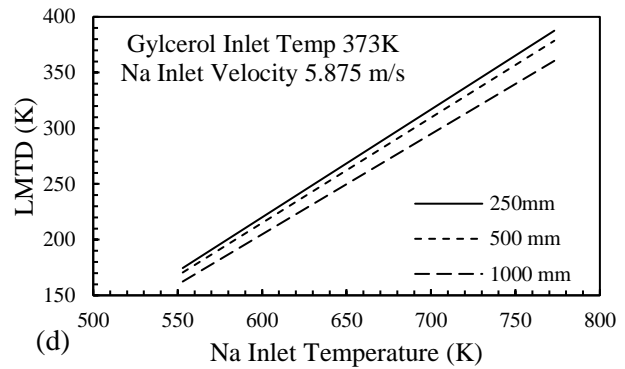
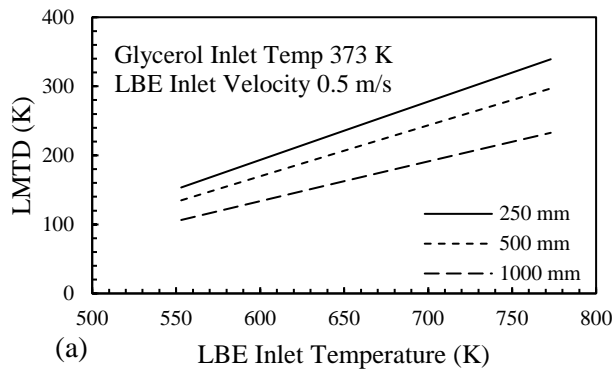


Fig. 5.14 Logarithmic mean temperature difference as the function of inlet temperature of liquid metal

Fig. 5.14 is representing the logarithmic mean temperature difference (LMTD) as a function of liquid metal inlet temperature (T_{hi}) for various inlet conditions. It can be inferred that the LMTD is increasing with the inlet temperature regardless of the fluid. The high values of LMTD are achieved when the difference between the inlet temperatures of the liquid metal and the glycerol is high. The maximum value of LMTD for LBE is 379.414 K and for Liq. sodium is 390.974 K for the inlet conditions of $T_{hi} = 773\text{ K}$, $T_{ci} = 373\text{ K}$, and $u_h = 2.0\text{ m/s}$ & 17.625 m/s respectively.

5.3. Effect of Extended Surfaces

Extended surfaces (fins) are widely employed in various heat transfer components that are used in a wide range of applications like heat sinks, microprocessor cooling & latent thermal energy storage devices and thus the fins have always been a notable domain for research. Increasing the exposed surface area by attaching the fins is a prominent method to enhance the rate of heat transfer with the advantage of being economically feasible. Extensive studies are available which analyze the thermal performance and costing of different types of fins. Krishnayatra et al. [67] conducted a numerical study to elaborate on the use of fins for heat transfer enhancements in a heat exchanger device with an isothermal inner wall for natural convection heat transfer. The 3-dimensional model used in the study along with the schematic representation is shown in Fig. 5.15. Table 5.1 is showing the geometrical parameters and boundary temperatures.

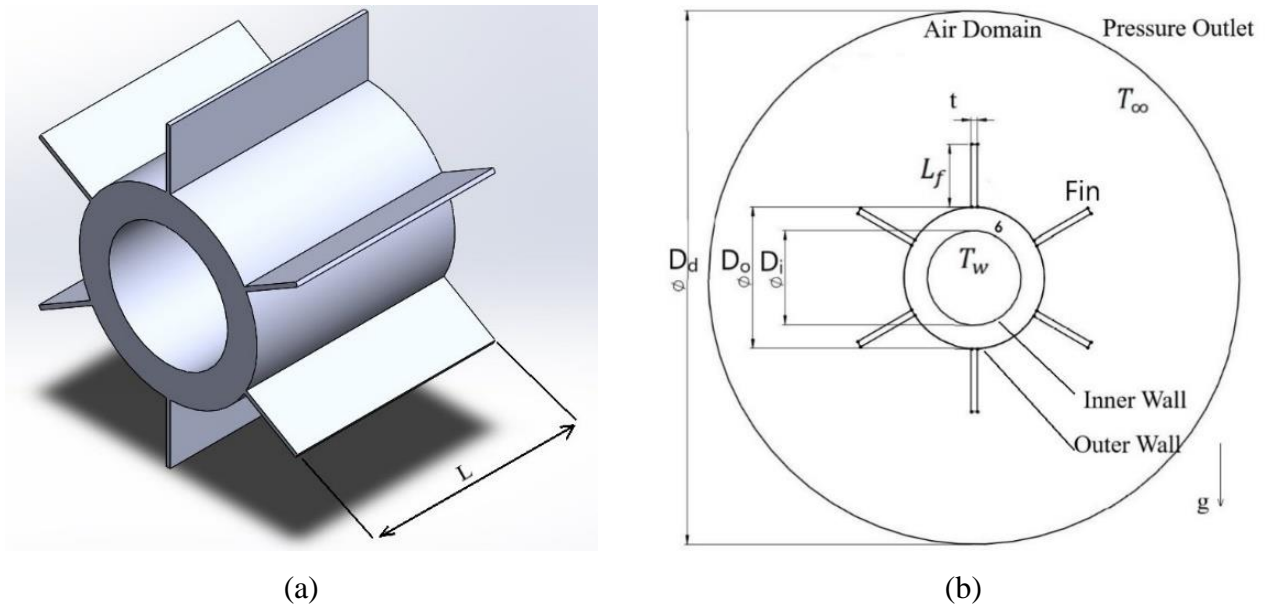


Fig. 5.15 a) 3-Dimensional representation of the model used for simulation b) Schematic diagram showing the geometrical dimensions for [67]

Table 5.1 Geometrical Parameter of the Finned-tube system

Parameter	Values		
Inner Diameter of Tube (D_i)	45 mm		
Outer Diameter of Tube (D_o)	30 mm		
Fin thickness (t)	1.0 mm	1.5 mm	2.0 mm
Fin length (L_f)	10 mm	15 mm	20 mm
Inner wall Temperature (T_w)	310 K		
Free Stream Temperature (T_∞)	290 K		
Bulk Temperature of air (T_b)	300 K		

Fig. 5.16 a) is showing the variation of effectiveness for increasing number of fins for 1 mm fin thickness, it can be observed that the effectiveness is maximum for longest fin length and for $L^* = \frac{L_f}{D_o} = 0.333$ & 0.444, it is increasing with the number of fins.

Fig. 5.16 b) is showing the effectiveness as the function of non-dimensional fin length. It can be inferred that for every number of fins there exists an optimum fin length.

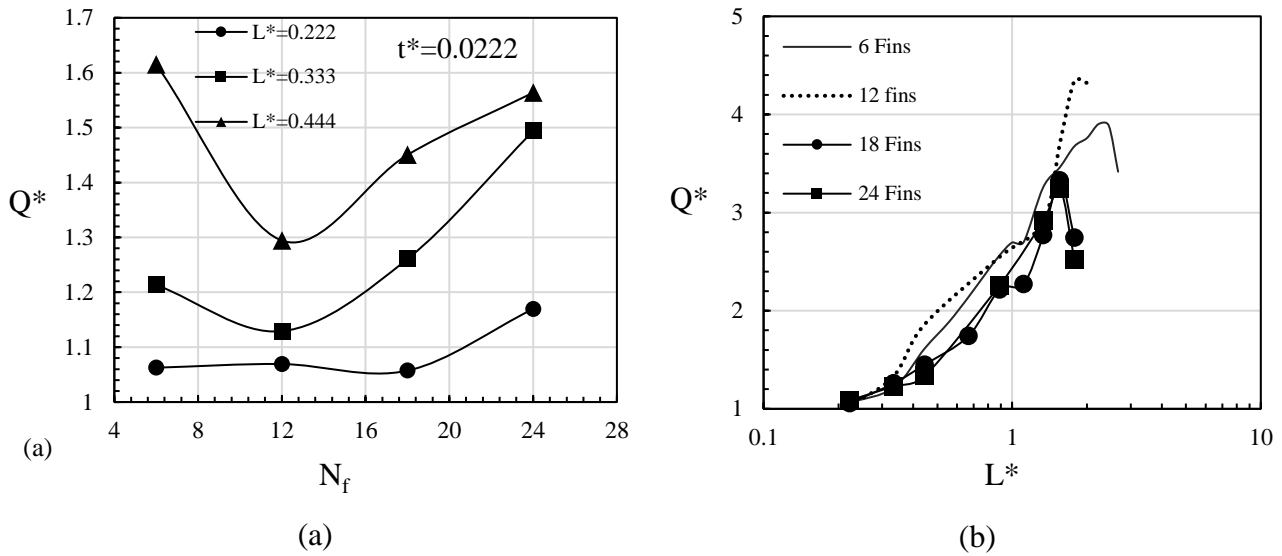


Fig. 5.16 a) Effectiveness as a function of number of fins for different fin lengths b) Effectiveness as a function of non-dimensional fin length for different N_f

After a thorough literature review, it was deduced that some designs of finned-tube heat exchangers are particularly overlooked. Krishnayatra et al. [48] conducted one such study in which the design and numerical analysis of a finned-tube heat exchanger with novel fin were conducted. The finned-tube heat exchanger consists of a hollow tube with an isothermal boundary condition at the inner wall (in order to simulate some of the industrial applications) having the novel rectangular fins attached axially at the outer wall. The novel design of fins consists of a fin-on-fin approach, wherein Fig. 5.17, it is visible that the tube has primary fins (coloured in black), this is a simple case of longitudinal fins attached to the outer surface of the tube. But consequently, another set of fins, the secondary fins (coloured in blue), are attached on to the primary fins in order to increase the total finned area that proportionately enhances the total rate of heat transfer. In this study, the variations of the overall Efficiency and the Effectiveness of the novel finned-tube system was analyzed with respect to the varying fin thickness, fin spacing, material of the system, and the convective heat transfer coefficient using Ansys Fluent. Moreover, Machine learning technique called k -Nearest Neighbor (k -NN) was employed for regression analysis to predict the thermal performance of the novel finned-tube system. A similar study was conducted by Tokas

et al. [49] which had a greater number of secondary fins attached to the primary fins for increasing convective heat transfer area.

The design consisted of a tube with the inner diameter (D_i) and the outer diameter (D_o) of 5 & 6 mm respectively with the fin thickness (t) being varied from 0.2 to 2.4 mm and having the fin spacing (δ) from 0.6 to 48 mm as shown in Fig. 1. The two materials of the finned-tube system chosen were Copper ($K_{Cu} = 387.6 \text{ W/m.K}$) and Steel ($K_{Ss} = 16.7 \text{ W/m.K}$). The conjugated heat transfer is taking place from the inner isothermal wall ($T_w = 400 \text{ K}$) to the ambient air ($T_\infty = 300 \text{ K}$). To reduce computational cost and time, the simulated flow of air on the outer surface of the finned-tube system has not been considered. However, a range of convective heat transfer coefficient was taken which covers almost all the practical applied values found in heat exchangers in order to visualize the impact of its variation on the efficiency and the effectiveness of the system. The convective heat transfer coefficient (h) at the outer surface is being varied from 5 to 200 W/m.K.

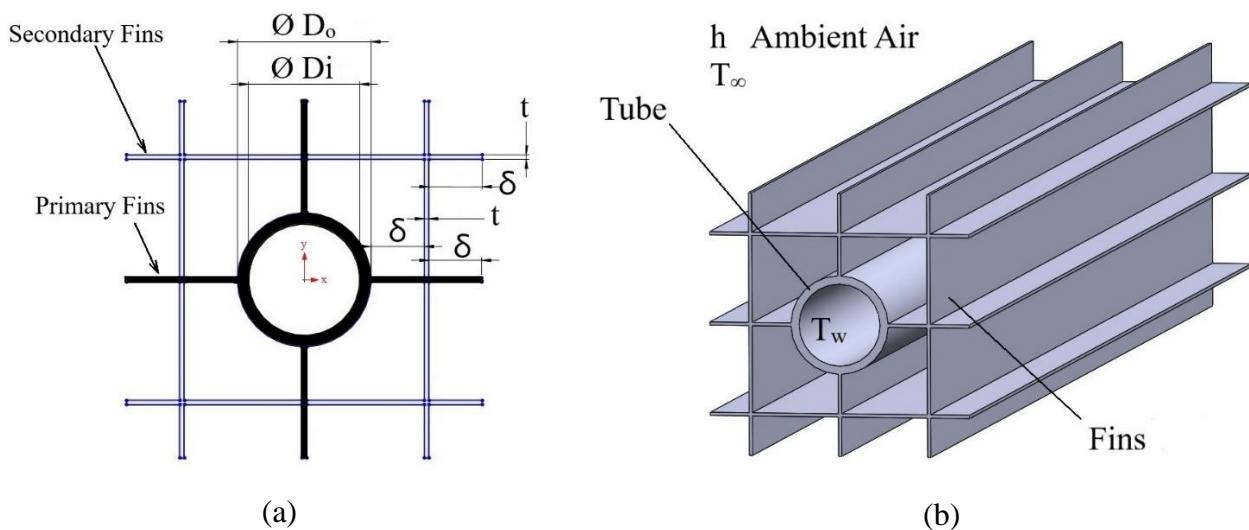


Fig. 5.17 a) Schematic diagram showing the geometrical dimensions for [48] b) 3-Dimensional representation of the model

Fig. 5.18 a) is showing the variation of effectiveness with non-dimensional fin spacing, which is essentially non-dimensional fin length, for different fin thickness. It can be seen that for stainless steel, the effectiveness is insensitive to change in non-

dimensional fin spacing after a certain value. Fig. 5.18 b) shows the comparison between the predicted effectiveness from the machine learning regression and the computed effectiveness from the CFD results, it can be inferred that machine learning technique can be successfully employed for output prediction in the case of heat transfer in a heat exchanger with fins.

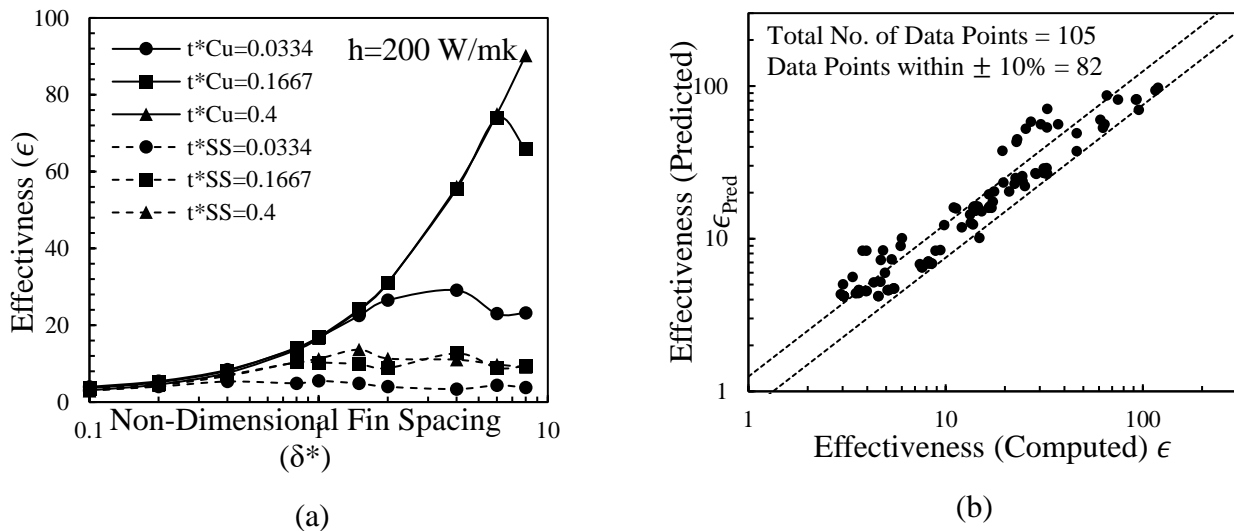


Fig. 5.18 a) Effectiveness as a function of non-dimensional fin spacing b) Effectiveness predicted with respect to computed effectiveness representing the accuracy of machine learning regression

In this thesis, longitudinal fins are attached to the outer surface of the inner tube with constant fin thickness of 0.5 mm having fin lengths 2.5 mm , 4.0 mm , & 5.5 mm for the case with inlet boundary conditions of $T_{hi} = 553 \text{ K}$ and $T_{ci} = 423 \text{ K}$. Fig. 5.19 a) is showing the variation of the overall effectiveness of the finned-tube system with increasing non-dimensional fin length ($L^* = \frac{L_f}{D_i}$) for 16 and 24 fins. It can be seen that effectiveness is higher with 24 fins for all fin lengths. Fig. 5.19 b) is showing the variation of non-dimensional overall heat transfer coefficient ($U^* = \frac{U_{fins}}{U_o}$), where U_o is the overall heat transfer coefficient for the IHX without fins for same inlet conditions.

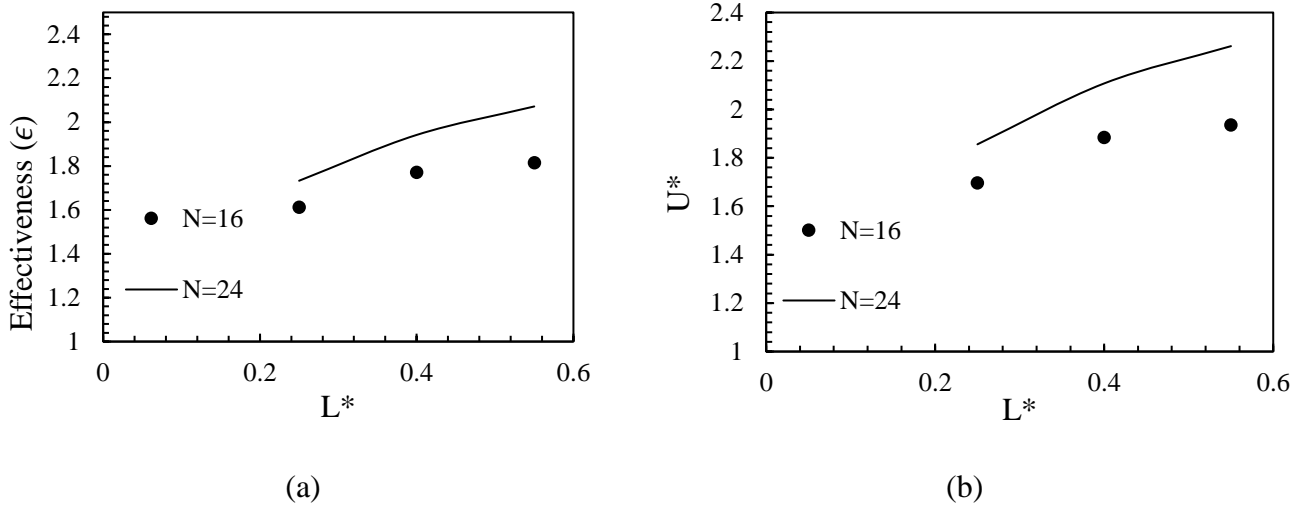


Fig. 5.19 a) Effectiveness of the fins with increasing fin length b) Non-dimensional overall heat transfer coefficient as a function of fin length

Fig. 5.20 shows the density variation and the thermal boundary layer under steady-state heat transfer of the IHX.

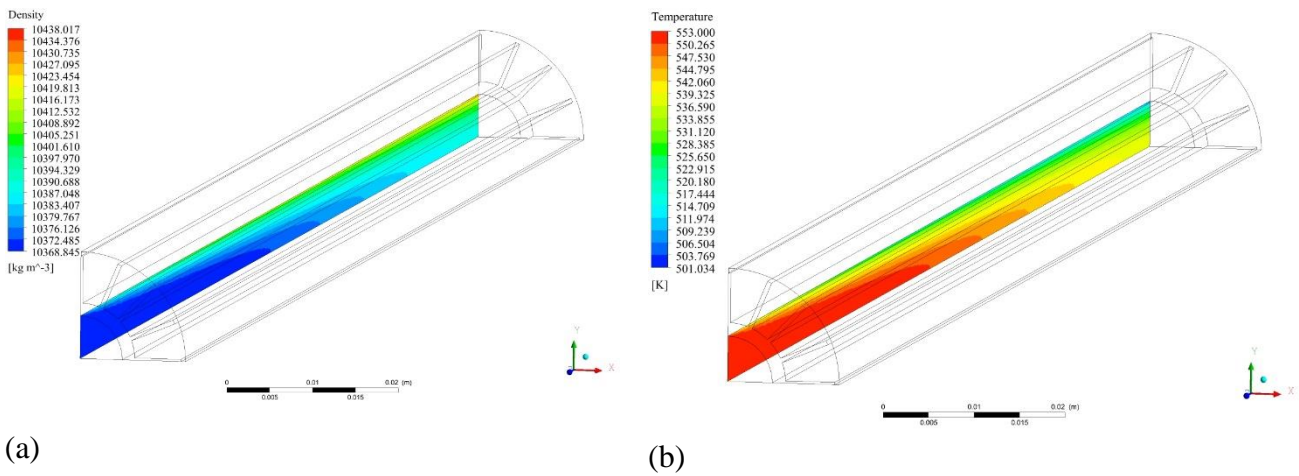


Fig. 5.20 Showing a) density variation and b) temperature plume along the length at steady state heat transfer for N=16 fins and 5.5 mm fin length

5.4. Comparison of LBE & Liq. Sodium

In earlier sections, the differences between the thermophysical properties of LBE & Liq. sodium were discussed. In this section, the impact of those differences on the rate of heat transfer has been analyzed and commented upon. Fig. 5.22 a) is showing the variation of the Prandtl number of LBE & Liq. sodium with the temperature. It can be seen that LBE has a higher value than that of Liq. sodium for all working temperature range. The Nusselt number is the non-dimensional form of convective heat transfer coefficient which is directly related to the Prandtl number, which implies that higher value of Prandtl number should result in higher convective heat transfer coefficient, which in turn gives a higher rate of heat transfer. Fig. 5.22 b) is showing the thermal conductivity of LBE & Liq. sodium as a function of temperature and it can be observed that LBE has a lower value for the whole temperature range. Even with higher Prandtl number of LBE, Liq. sodium has significantly higher thermal conductivity. As signified earlier, during the convective heat transfer of liquid metals the thermal conductivity has much greater significance than other temperature-dependent thermophysical properties.

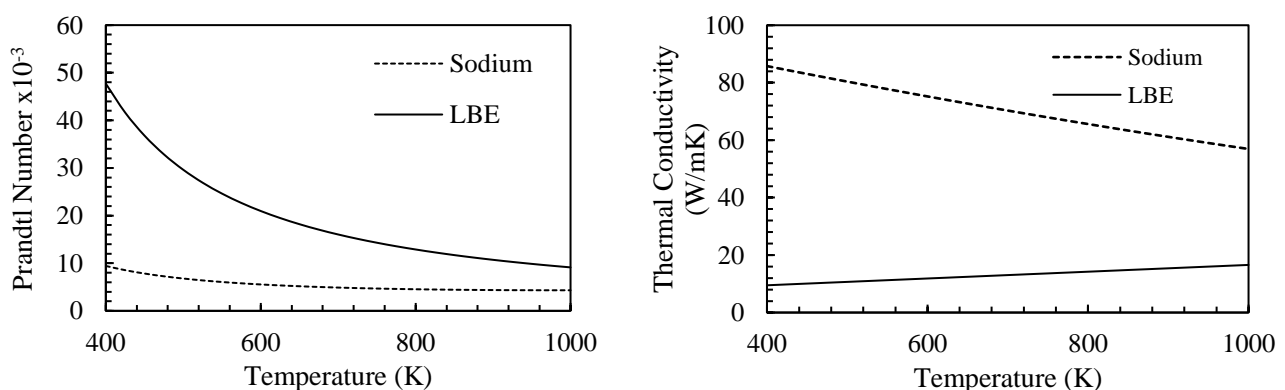


Fig. 5.21 a) Prandtl number as a function of temperature for various liquid b) Thermal conductivity as a function of temperature for various liquid metals

Fig. 5.23 is showing a comparison of the total heat transfer rate between LBE and Liq. sodium for same mass flow rate. It can be seen that the Liq. sodium has a much higher rate of heat transfer for all glycerol inlet temperature and for all values of corresponding mass flow rate, due to the fact that Liq. sodium has significantly higher thermal conductivity.

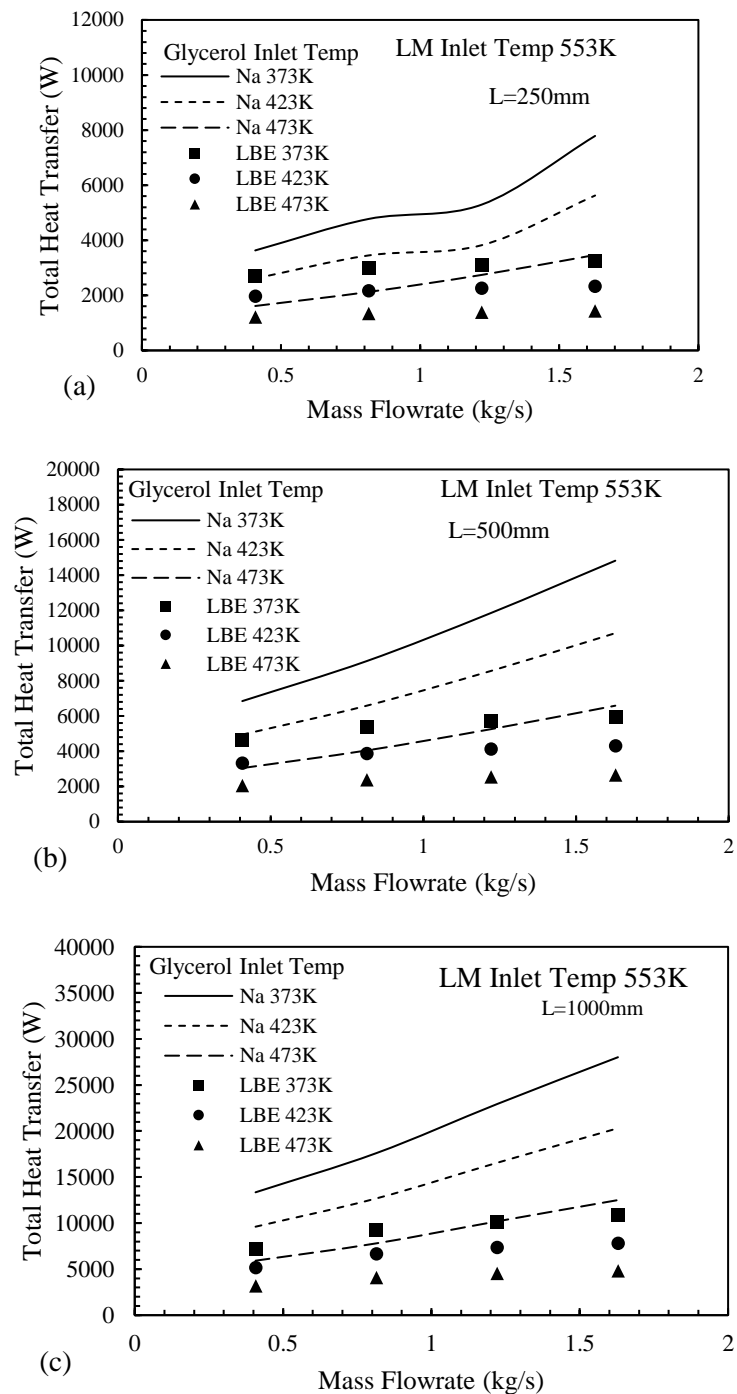


Fig. 5.22 Total Rate of Heat Transfer comparison for LBE and Liq. sodium

5.5. Correlation Formation

A non-linear regression analysis using the Generalized Reduced Gradient (GRG) is done by developing a correlation between the overall heat transfer coefficient (inner side) U_i and the input boundary conditions. Regression analysis of the overall heat transfer coefficient of the IHX is performed in order to assess the impact and sensitiveness of the variations of the inlet conditions.

$$\frac{1}{US} = \frac{1}{U_i S_i} = \frac{1}{U_o S_o} = \frac{1}{h_h S_i} + \frac{\ln(r_2/r_1)}{2\pi LK} + \frac{1}{h_c S_o} \quad (5.1)$$

Eq. 5.1 shows the overall heat transfer coefficient as the function of the convective heat transfer coefficient of the hot & cold side, the geometry of tube, and the thermal conductivity of the tube material.

$$\frac{1}{U_i} = \frac{1}{h_h S_i} + \frac{\ln(r_2/r_1)}{2\pi LK/S_i} + \frac{1}{h_c (S_o/S_i)} \quad (5.2)$$

From Eq. 5.2, it can be seen that U_i depends upon the convective heat transfer coefficient of hot fluid (liquid metal), the inner surface area of the tube, convective heat transfer coefficient, the outer surface area of the tube, length of the IHX. It is known that the convective heat transfer coefficient is the function of Reynolds number and the Prandtl number. Considering all the constants and all the independent variable in the Eq. 5.1 & 5.2, then Eq. 5.2 can be simplified and written in a generalized form as:

$$\frac{1}{U_i} = \frac{1}{k_h (a_1 Re_h^{a_2} Pr_h^{a_3})} + \frac{a_4}{L} + a_5 T_{ci}^{a_6} + a_7 \quad (5.3)$$

Where, a_i are the coefficients, k_h is the thermal conductivity of (hot fluid) liquid metal, Re_h & Pr_h are the Reynolds number and Prandtl number of the LM.

Generalized reduced gradient (GRG) algorithm [65] is being used to find the correlation between the overall heat transfer coefficient and the independent input

variables which are namely the Reynolds number and the Prandtl number of the liquid metal, the thermal conductivity of the liquid metal, the length of the IHX, the inlet temperature of the glycerol for both the liquid metal considered for the IHX. An iterative method is used while applying the GRG algorithm to optimize the coefficients of the correlations in order to minimize the sum of the squared difference between the computed outputs from simulation results and the predicted outputs based on the developed correlations. This method is suitable when there are fewer number of independent variables and when a justified parametric correlation is used along with suitable coefficient values [66].

The correlation developed for the overall heat transfer coefficient for LBE is:

$$\frac{1}{U_{LBE}} = \frac{1}{k_h(577.6371Re_h^{0.1606}Pr_h^{0.3938})} - \frac{8.3708 \times 10^{-6}}{L} + 0.00035T_{ci}^{-0.003435} + (1.0241 \times 10^{-5}) \quad (5.4)$$

The correlation developed for the overall heat transfer coefficient for Liq. sodium is:

$$\frac{1}{U_{Na}} = \frac{1}{k_h(0.3159Re_h^{0.4118}Pr_h^{0.08604})} - \frac{4.1027 \times 10^{-6}}{L} + (3.1877 \times 10^{-5})T_{ci}^{-0.4197} + (7.1148 \times 10^{-6}) \quad (5.5)$$

The predicted values of the U_i are compared to the computed U_i from the simulation results in terms of R^2 values to check the accuracy of the regression model. The R^2 value is the coefficient of determination which is given by the following relation:

$$R^2 = 1 - \frac{\sum_i (y_i - p_i)^2}{\sum_i (y_i - \bar{y})^2} \quad (5.6)$$

Where, y_i is the i^{th} output variable and p_i is the corresponding predicted value for the i^{th} element in the data and \bar{y} is the mean of the output variable.

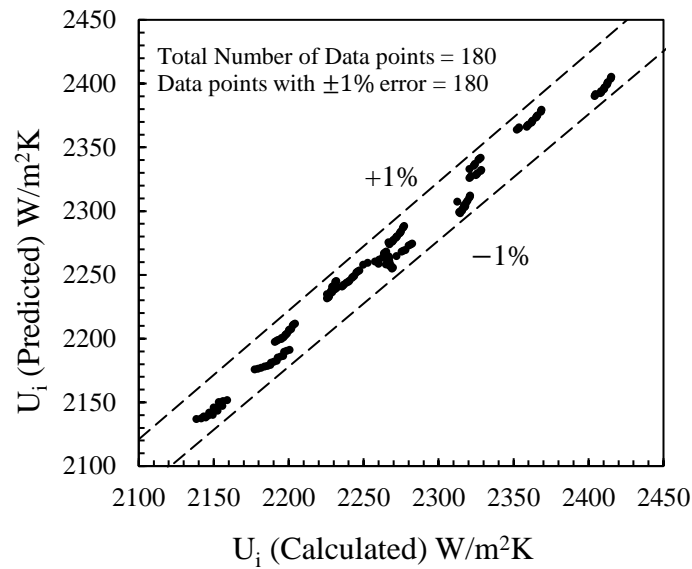


Fig. 5.23 Predicted values and calculated values of overall heat transfer coefficient for LBE

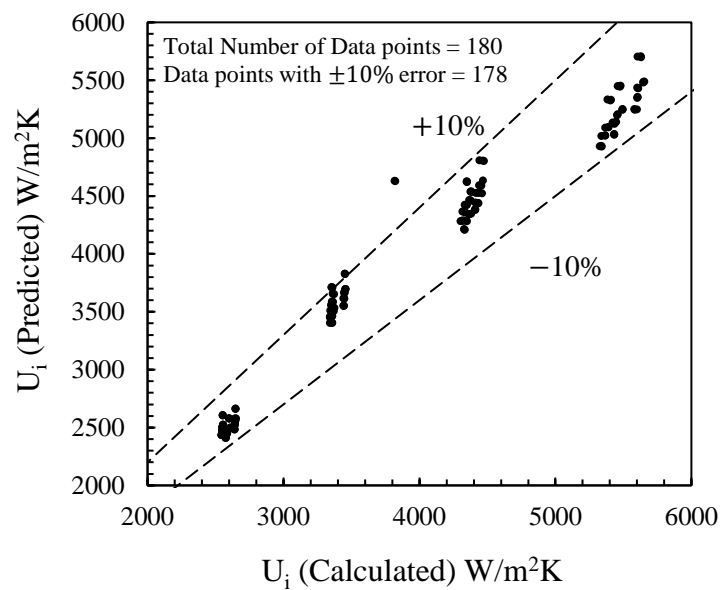


Fig. 5.24 Predicted values and calculated values of overall heat transfer coefficient for Liq. sodium

Fig. 5.23 is showing the predicted values of the overall heat transfer coefficient using the correlation developed for LBE given in Eq. 5.4 against the calculated values by the CFD results. Similarly, Fig. 5.24 is showing the predicted versus calculated overall heat transfer coefficient for Liq. sodium. The R^2 value for the regression model of LBE is 0.9847 and for Liq. sodium is 0.9624, which can be classified as a fairly accurate model.

5.6. ANN Regression Analysis

A backpropagation artificial neural network (ANN) regression algorithm has been employed for predicting the overall heat transfer coefficient (U_i) using Python code. The variables under consideration are given in Table 5.2.

Table 5.2 Variables taken for ANN regression analysis

Input Variables	Output Variable
Reynolds number – liquid metal (Re_h)	Overall heat transfer coefficient – inner wall (U_i)
Prandtl number – liquid metal (Pr_h)	
Thermal Conductivity – liquid metal (k_h)	
Length of the IHX (L)	
Inlet temperature of glycerol (T_{ci})	

For applying the ANN, various combinations of number of hidden layers and number of nodes were considered and the hit-and-trial method was used for achieving the optimized values. Consider an ANN model with two hidden layers and 4 & 5 nodes in those hidden layers respectively, then the model is termed as a (4, 5) ANN model. Hence, several combinations were tried and tested for achieving an optimized result. Table 5.3 & 5.4 is showing the various configuration considered for ANN models and the corresponding R^2 values representing their prediction accuracies for LBE and Liq. sodium respectively. It can be observed that for LBE, the (6, 8, 6) configuration was giving the highest accuracy and for Liq. sodium the configuration of (10, 12, 10) was giving the highest accuracy. Therefore, these configurations are chosen for the prediction of U_i . For all the ANN models, the data was normalized and then divided into two equal parts for training and testing. After the model fitting, the predicted data was exported from Python.

Table 5.3 ANN configuration with the corresponding R^2 values for LBE

ANN configuration	R^2 value
(6, 6)	0.9960
(6, 8, 6)	0.9964
(6, 10, 6)	0.9949
(6, 12, 6)	0.9951
(8, 8)	0.9900
(8, 10, 8)	0.9913
(8, 12, 8)	0.9899
(10, 10)	0.9852
(10, 12, 10)	0.9915

Table 5.4 ANN configuration and the corresponding R^2 values for Liq. sodium

ANN configuration	R^2 value
(6, 6)	0.9905
(6, 8, 6)	0.9856
(6, 10, 6)	0.9816
(6, 12, 6)	0.9903
(8, 8)	0.9905
(8, 10, 8)	0.9895
(8, 12, 8)	0.9838
(10, 10)	0.9917
(10, 12, 10)	0.9918

Fig. 5.25 & 5.26 are showing the predicted values of the overall heat transfer coefficient from the ANN model with the computed values from the CFD results for LBE & Liq. sodium respectively. For LBE, it can be observed that all data points are within the $\pm 1\%$ error lines. For Liq. sodium, it is observed that two data points are showing an anomaly, these data points are called outliers. Outliers are usually common in such type of models, where the data is generated first hand. However, the rest of the 78 data points are lying within $\pm 4\%$ error lines. While comparing with the non-linear

regression model applied earlier by using the correlation, it can be firmly concluded that using the ANN model is more accurate as evident by the R^2 values, for both the liquid metal.

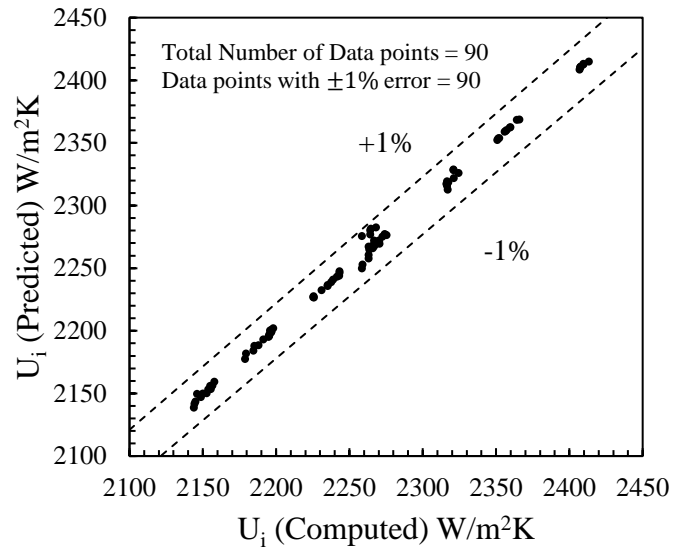


Fig. 5.25 Predicted and computed values of the overall heat transfer coefficient for LBE using ANN regression model

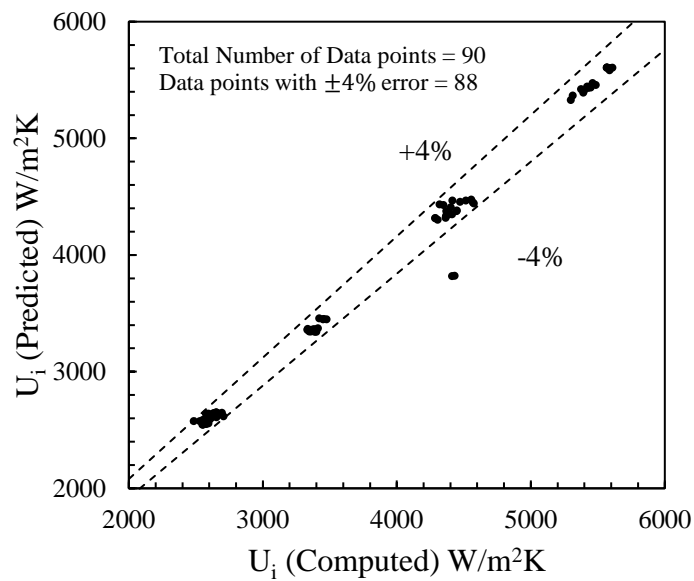


Fig. 5.26 Predicted and computed values of the overall heat transfer coefficient for Liq. sodium using ANN regression model

6. CONCLUSIONS

The main objective of this thesis is to perform a thermal hydraulic analysis of a double-pipe Intermediate Heat Exchanger (IHX) which can be potentially used in liquid metal cooled nuclear reactor (LMCR) using numerical techniques. A CFD analysis was performed on the heat transfer and fluid flow characteristics of Lead-Bismuth Eutectic (LBE) and Liq. Sodium for turbulent flow region flowing the tubular part of the IHX. Moreover, the thermal performance of the IHX is analyzed with the variation in inlet conditions which resulted in 180 cases for each liquid metal, all of these 360 cases were simulated using Ansys Fluent.

The fundamentals of Nuclear thermal energy were explained along with the working and construction of Liquid Metal Fast Breeder Reactor (LMFBR). The significant advantages of the use of liquid metals as a coolant in nuclear reactors were also explained in Chapter 1. The governing equations with respect to the thermophysical properties of liquid metals were described and numerical modelling was explained in Chapter 2 & 4.

Conclusively, this study gives us some insights which are:

1. The heat transfer and fluid flow simulations for 3D models of the IHX were computational expensive and time consuming, therefore, axis-symmetrical 2D models can be used in the place of 3D without compromising the accuracy of the CFD results.
2. 2-Dimensional CFD modelling of liquid metal flowing in a long tube under turbulent flow regime were in fairly close agreement with the experimental results of [5], [24], [41], [42], [43], [49], [60], & [62].

3. The longest IHX with length 1000 mm achieved the maximum rate of heat transfer, however, there is a scope of optimization of the size of the heat exchanger which can be considered as a future perspective.
4. The extended surfaces can be used as a heat transfer enhancement technique in double-pipe IHX where the fins are attached on the outer wall of the inner tube, for this size of IHX, the maximum achieved effectiveness was 2.07.
5. For the same mass flow of Lead-Bismuth Eutectic and Liq. Sodium, the Liq. sodium shows higher values of heat transfer rate for all inlet conditions therefore, it is the preferable choice of liquid metal coolant with the obvious advantages of having low density and low viscosity.
6. The overall heat transfer coefficient (U) can be considered as a function of thermal conductivity, Reynolds number, and Prandtl number of liquid metal, & the length of the heat exchanger and also the inlet temperature of glycerol. A correlation was developed for both the liquid metals, the R^2 score for LBE is 0.9847 and for Liq. sodium is 0.9624. These high R^2 values show that the GRG algorithm can be used for developing a correlation computing the overall heat transfer coefficient without actually performing the CFD analysis which inherently saves time and resources.
7. The Artificial Neural Network (ANN) which is used for regression analysis for predicting the overall heat transfer coefficient for the same independent input variables show remarkable accuracies. The ANN configuration which resulted in highest accuracy had 3 hidden layers. For IHX with LBE, the (6, 8, 6) configuration showed the highest accuracy with the R^2 value of 0.9964 and for Liq. Sodium, the configuration of (10, 12, 10) resulted in the highest accuracy with 0.9918 R^2 score. This implies that the ANN algorithm is robust, precise, and accurate and it can be used for regression analysis for predicting overall heat transfer coefficient for a double-pipe IHX with liquid metal flowing through the tube.

There are various future perspectives on this thesis. In this study, RANS approach was used for CFD analysis of the IHX. However, techniques like LES & DNS can be used in this type of analysis since these techniques are notably more accurate than the RANS. Other designs of the heat exchangers can be considered for this type of analysis as well.

REFERENCES

- [1] H. Akimoto, Y. Anoda, K. Takase, H. Yoshida, and H. Tamai, “Nuclear Thermal Hydraulics”, vol. 4, *Springer – Japan*, 2016.
- [2] F. Roelofs, *Introduction to liquid metal cooled reactors*. Elsevier Ltd., 2018.
- [3] M. M. El-Wakil, “Powerplant Technology,” *McGraw-Hill Book Company*, U.S.A., Int. Ed., 1985.
- [4] P. Saha, “Nuclear Reactor Thermal Hydraulic: Past , Present and Future ”, no. 4. *ASME Press*, 2011.
- [5] M. K. Ibragimov, V. I. Subbotin, and P. A. Ushakov, “Investigation of heat transfer in the turbulent flow of Liquid Metals in Tubes,” *Atomnaya Energiya*, no. 1, pp. 54–56, 1960.
- [6] E. Dwyer, “Eddy Transport Heat Transfer in Liquid-Metal,” *A.I.Ch.E. Journal* vol. 9, no. 2, pp. 261–268, 1963.
- [7] R. E. Holtz, “Investigation of heat transfer to liquid metals flowing in Circular Tubes,” *A.I.Ch.E. Journal*, vol. 11, no. 6, pp. 1151–1153, 1965.
- [8] R. P. Stein, “Liquid Metal Heat Transfer”, *Advances in Heat Transfer*, vol. 3, pp. 101-174, 1966, doi: [https://doi.org/10.1016/S0065-2717\(08\)70051-0](https://doi.org/10.1016/S0065-2717(08)70051-0).
- [9] J. H. Rust, “A parametric analysis of Lyon’s Integral equation for Liquid-metal heat transfer coefficient”, *Nuclear Engineering and Design*, vol. 16, pp. 223–236, 1971.
- [10] W. J. Minkowycz and R. P. Stein, “A design guide for calculating liquid-metal turbulent forced convection heat transfer with non-uniform heat fluxes and

- transients,” *Nuclear Engineering and Design*, vol. 31, no. 1, pp. 21–30, 1974, doi: [https://doi.org/10.1016/0029-5493\(74\)90130-7](https://doi.org/10.1016/0029-5493(74)90130-7).
- [11] R. Nijsing and W. Eifler, “A computational analysis of transient heat transfer in fuel rod bundles with single phase liquid metal cooling,” *Nuclear Engineering and Design*, vol. 62, no. 1, pp. 39–68, 1980, doi: [https://doi.org/10.1016/0029-5493\(80\)90020-5](https://doi.org/10.1016/0029-5493(80)90020-5).
- [12] W. M. Kays, “Turbulent Prandtl Number - Where Are We?”, *Trans. ASME*, vol. 116, pp. 284–295, 1994.
- [13] S. Raghupathy, O. P. Singh, S. Govindarajan, S. C. Chetal, and S. B. Bhoje, “Design of 500 MWe prototype Fast Breeder Reactor,” *Nuclear India*, 2004.
- [14] X. Cheng and N. I. Tak, “CFD analysis of thermal-hydraulic behavior of heavy liquid metals in sub-channels,” *Nuclear Engineering and Design*, vol. 236, no. 18, pp. 1874–1885, 2006, doi: [10.1016/j.nucengdes.2006.02.001](https://doi.org/10.1016/j.nucengdes.2006.02.001).
- [15] W. A. Khan, J. R. Culham, and M. M. Yovanovich, “Analytical study of heat transfer from circular cylinder in liquid metals,” *Heat and Mass Transfer/Waerme- und Stoffuebertragung*, vol. 42, no. 11, pp. 1017–1023, 2006, doi: [10.1007/s00231-005-0068-4](https://doi.org/10.1007/s00231-005-0068-4).
- [16] T. S. Mathews, M. Ramakrishnan, U. Parthasarathy, A. J. Arul, and C. S. Kumar, “Functional reliability analysis of Safety Grade Decay Heat Removal System of Indian 500 MWe PFBR,” *Nuclear Engineering and Design*, vol. 238, no. 9, pp. 2369–2376, 2008, doi: [10.1016/j.nucengdes.2008.02.012](https://doi.org/10.1016/j.nucengdes.2008.02.012).
- [17] Y. Deng and J. Liu, “Design of practical liquid metal cooling device for heat dissipation of high performance CPUs,” *Journal of Electronic Packaging, Transactions of the ASME*, vol. 132, no. 3, pp. 1–6, 2010, doi: [10.1115/1.4002012](https://doi.org/10.1115/1.4002012).
- [18] J. Guo and X. Huai, “Thermodynamic analysis of lead-bismuth eutectic turbulent flow in a straight tube,” *Energy*, vol. 57, pp. 600–606, 2013, doi: [10.1016/j.energy.2013.05.008](https://doi.org/10.1016/j.energy.2013.05.008).
- [19] W. Ma, A. Karbojian, B. R. Sehgal, and T. N. Dinh, “Thermal-hydraulic performance of heavy liquid metal in straight-tube and U-tube heat

- exchangers,” *Nuclear Engineering and Design*, vol. 239, no. 7, pp. 1323–1330, 2009, doi: 10.1016/j.nucengdes.2009.03.014.
- [20] F. Chen, J. Cai, X. Li, X. Huai, and Y. Wang, “3D numerical simulation of fluid-solid coupled heat transfer with variable property in a LBE-helium heat exchanger,” *Nuclear Engineering and Design*, vol. 274, pp. 66–76, 2014, doi: 10.1016/j.nucengdes.2014.04.024.
- [21] J. Pacio *et al.*, “Heavy-liquid metal heat transfer experiment in a 19-rod bundle with grid spacers,” *Nuclear Engineering and Design*, vol. 273, pp. 33–46, 2014, doi: 10.1016/j.nucengdes.2014.02.020.
- [22] J. Pacio, L. Marocco, and T. Wetzel, “Review of data and correlations for turbulent forced convective heat transfer of liquid metals in pipes,” *Heat and Mass Transfer/Waerme- und Stoffuebertragung*, vol. 51, no. 2, pp. 153–164, 2014, doi: 10.1007/s00231-014-1392-3.
- [23] D. Taler, “Heat Transfer in Turbulent Tube Flow of Liquid Metals,” *Procedia Engineering*, vol. 157, pp. 148–157, 2016, doi: 10.1016/j.proeng.2016.08.350.
- [24] V. I. Subbotin, A. K. Papovyants, P. L. Kirillov, and N. N. Ivanovskii, “A study of heat transfer to molten sodium in tubes,” *Soviet Atomic Energy*, vol. 13, no. 4, pp. 991–994, 1963, doi: 10.1007/BF01480861.
- [25] W. Jaeger, “Heat transfer to liquid metals with empirical models for turbulent forced convection in various geometries,” *Nuclear Engineering and Design*, vol. 319, pp. 12–27, 2017, doi: 10.1016/j.nucengdes.2017.04.028.
- [26] K. Hata, K. Fukuda, and S. Masuzaki, “Computational study of heat transfer from the inner surface of a circular tube to force high temperature liquid metal flow in laminar and transition regions,” *Heat and Mass Transfer/Waerme- und Stoffuebertragung*, vol. 54, no. 9, pp. 2853–2869, 2018, doi: 10.1007/s00231-018-2325-3.
- [27] S. Unger, E. Krepper, M. Beyer, and U. Hampel, “Numerical optimization of a finned tube bundle heat exchanger arrangement for passive spent fuel pool cooling to ambient air,” *Nuclear Engineering and Design*, vol. 361, no. April 2019, p. 110549, 2020, doi: 10.1016/j.nucengdes.2020.110549.

- [28] H. Mochizuki and M. Takano, "Heat transfer in heat exchangers of sodium cooled fast reactor systems," *Nuclear Engineering and Design*, vol. 239, no. 2, pp. 295–307, 2009, doi: 10.1016/j.nucengdes.2008.10.013.
- [29] H. Mochizuki, "Heat transfer in intermediate heat exchanger under low flow rate conditions," *Nuclear Technology*, vol. 170, no. 1, pp. 90–99, 2010, doi: 10.13182/NT10-A9448.
- [30] R. A. Seban and T. T. Shimazaki, "Heat Transfer to a Fluid Flowing Turbulently in a Smooth Pipe with Walls at Constant Temperature," *Transactions of the American Society of Mechanical Engineers*, 1951.
- [31] H. Mochizuki, "Liquid metal heat transfer in heat exchangers under low flow rate conditions," *Journal of Nuclear Science and Technology*, vol. 52, no. 6, pp. 821–828, 2015, doi: 10.1080/00223131.2014.980349.
- [32] H. Mochizuki, "Liquid metal heat transfer under low PECLET number conditions," *International Topical Meeting on Nuclear Reactor Thermal Hydraulics 2015, NURETH 2015*, vol. 2, pp. 1020–1032, 2015.
- [33] H. Mochizuki, "Consideration on Nusselt numbers of liquid metals under low Peclet number conditions," *Nuclear Engineering and Design*, vol. 339, no. July, pp. 171–180, 2018, doi: 10.1016/j.nucengdes.2018.09.010.
- [34] H. Mochizuki, "Consideration on Nusselt numbers of liquid metals flowing in tubes," *Nuclear Engineering and Design*, vol. 351, no. May, pp. 1–19, 2019, doi: 10.1016/j.nucengdes.2019.05.022.
- [35] G. Diaz, M. Sen, K. T. Yang, and R. L. McClain, "Simulation of heat exchanger performance by artificial neural networks," *ASHRAE Transactions*, vol. 106, pp. 195–208, 2000.
- [36] Y. Islamoglu, "A new approach for the prediction of the heat transfer rate of the wire-on-tube type heat exchanger - Use of an artificial neural network model," *Applied Thermal Engineering*, vol. 23, no. 2, pp. 243–249, 2003, doi: 10.1016/S1359-4311(02)00155-2.
- [37] G. N. Xie, Q. W. Wang, M. Zeng, and L. Q. Luo, "Heat transfer analysis for shell-and-tube heat exchangers with experimental data by artificial neural

- networks approach,” *Applied Thermal Engineering*, vol. 27, no. 5–6, pp. 1096–1104, 2007, doi: 10.1016/j.applthermaleng.2006.07.036.
- [38] C. K. Tan, J. Ward, S. J. Wilcox, and R. Payne, “Artificial neural network modelling of the thermal performance of a compact heat exchanger,” *Applied Thermal Engineering*, vol. 29, no. 17–18, pp. 3609–3617, 2009, doi: 10.1016/j.applthermaleng.2009.06.017.
- [39] W. Versteeg, H.K. Malalasekera, “Introduction to computational fluid dynamics”, *Pearson Education Ltd.*, U.K., 2006.
- [40] Y. Wu *et al.*, “Review on heat transfer and flow characteristics of liquid sodium (1): Single-phase,” *Progress in Nuclear Energy*, vol. 104, no. June, pp. 306–316, 2018, doi: 10.1016/j.pnucene.2017.11.004.
- [41] R. H. Notter and C. A. Sleicher, “A solution to the turbulent Graetz problem—III Fully developed and entry region heat transfer rates,” *Chemical Engineering Science*, vol. 27, no. 11, pp. 2073–2093, 1972, doi: [https://doi.org/10.1016/0009-2509\(72\)87065-9](https://doi.org/10.1016/0009-2509(72)87065-9).
- [42] C. A. Sleicher, A. S. Awad, and R. H. Notter, “Temperature and eddy diffusivity profiles in NaK,” *International Journal of Heat and Mass Transfer*, vol. 16, no. 8, pp. 1565–1575, 1973, doi: [https://doi.org/10.1016/0017-9310\(73\)90184-1](https://doi.org/10.1016/0017-9310(73)90184-1).
- [43] C. Ching-Jen and Jenq Shing Chiou, “Laminar and turbulent heat transfer in the pipe entrance region for liquid metals,” *International Journal of Heat and Mass Transfer*, vol. 24, no. 7, pp. 1179–1189, 1981, doi: [https://doi.org/10.1016/0017-9310\(81\)90167-8](https://doi.org/10.1016/0017-9310(81)90167-8).
- [44] X. Cheng and N. il Tak, “Investigation on turbulent heat transfer to lead-bismuth eutectic flows in circular tubes for nuclear applications,” *Nuclear Engineering and Design*, vol. 236, no. 4, pp. 385–393, 2006, doi: 10.1016/j.nucengdes.2005.09.006.
- [45] N. Forgione, D. Castelliti, A. Gerschenfeld, M. Polidori, A. del Nevo, and R. Hu, “System thermal hydraulics for liquid metals,” *Thermal Hydraulics Aspects*

- of Liquid Metal Cooled Nuclear Reactors*, pp. 157–184, 2018, doi: 10.1016/B978-0-08-101980-1.00004-1.
- [46] N. Sheriff and D. J. O’kane, “Sodium eddy diffusivity of heat measurements in a circular duct,” *International Journal of Heat and Mass Transfer*, vol. 24, no. 2, pp. 205–211, 1981, doi: [https://doi.org/10.1016/0017-9310\(81\)90028-4](https://doi.org/10.1016/0017-9310(81)90028-4).
- [47] O.J. Foust, “Sodium-NaK Engineering Handbook. Volume I. Sodium Chemistry and Physical Properties.,” vol. I, 1972, doi: <https://www.osti.gov/biblio/4631555>.
- [48] G. Krishnayatra, S. Tokas, and R. Kumar, “Numerical heat transfer analysis & predicting thermal performance of fins for a novel heat exchanger using machine learning,” *Case Studies in Thermal Engineering*, vol. 21, p. 100706, Oct. 2020, doi: 10.1016/j.csite.2020.100706.
- [49] S. Tokas, G. Krishnayatra, and M. Zunaid, “Numerical investigation of thermal performance of extended surfaces for a novel heat exchanger”, *Heat Transfer*, p. htj.21879, Jul. 2020, doi: 10.1002/htj.21879.
- [50] H.A. Johnson, J.P. Hartnett, and W.J. Clabaugh, “Heat transfer to lead-bismuth and mercury in laminar and transition pipe flow”, Berkeley, California, *United States Atomic Energy Commission*, AECU-2637, 1953.
- [51] S.E. Isakoff, and T.B. Drew, “Heat and momentum transfer in turbulent flow of mercury”, No. AECU-1199. Columbia Univ. and Brookhaven National Lab., 1951.
- [52] W.K. Stromquist, “Effect of Wetting on Heat Transfer Characteristics of Liquid Metals:(thesis)” Vol. 93. *United States Atomic Energy Commission*, Technical Information Service, 1953.
- [53] R. L. Merriam, “An Investigation of Liquid-metal Heat Transfer in a Cocurrent-flow, Double-pipe, Heat Exchanger”, *Reactor Engineering Division, Argonne National Laboratory*, 1965.

- [54] N.A. Ampleyev, "Heat transfer with liquid metal in a vertical pipe at low Peclet numbers", pp. 8-27, 1969.
- [55] V.D. Talanov, "Study of heat transfer in liquid metals in round pipes", pp. 1-7, 1969.
- [56] S. Aoki, "A Consideration on the Heat Transfer in Liquid Metal", *Bulletin of the Tokyo Institute of Technology*, pp. 63-73, 1963.
- [57] R. C. Martinelli, "Heat transfer to molten metals", *Trans. ASME*, vol. 69, pp. 947-959, 1947.
- [58] S. Kakac, R.K. Shah, and W. Aung, "Handbook of single-phase convective heat transfer", *John Wiley and Sons Inc*, U.S.A., 1987.
- [59] F.P. Incropera, D.P. Dewitt, T.L. Bergman, and A.S. Levine, "Fundamentals of Heat and Mass Transfer", 6th Edition, *John Wiley & Sons*, U.S.A., 2007.
- [60] R. A. Seban, and T. T. Shimazaki, "Heat transfer to a fluid flowing turbulently in a smooth pipe with wall at constant temperature", *Trans. Am. Soc. Mech. Eng.* Vol. 73, pp. 803-809, 1950.
- [61] C. Sleicher, and M. Tribus Jr, Heat transfer in a pipe with turbulent flow and arbitrary wall temperature distribution. *Trans. Am. Soc. Mech. Eng.*, vol. 79, pp. 788-797, 1957.
- [62] P.L. Kirillov, and P.A. Ushakov, "Heat transfer to liquid metals: Specific features, methods of investigation, and main relationships", 2001.
- [63] C. Reed, "Convective heat transfer in liquid metals". In: Kakac, S, Shah RK, Aung W (eds) *Handbook of single-phase convective heat transfer*, chap 8. *Wiley*, New York, 1987.
- [64] R. Lyon, "Heat transfer coefficient in liquid metals." *Chemical Engineering Progress* 47.2, pp. 75-81, 1951.

- [65] L. S. Lasdon, R. L. Fox, M. W. Ratner, "Nonlinear optimization using the gradient reduced gradient method", *R. A. I. R. O.*, vol. 3, pp. 73-104, 1974.
- [66] L. Massaron, A. Boschetti, "Regression Analysis with Python", *Packt Publishing ltd.* Birmingham UK. 2016.
- [67] G. Krishnayatra, S. Tokas, R. Kumar, M. Zunaid, "Parametric study of natural convection showing effects of geometry, number and orientation of fins on a finned tube system: a numerical approach", *Journal of Thermal Engineering*.
[Article In Press]

Appendix A

User Defined Functions

The thermophysical properties of liquid metals are temperature dependent as mentioned earlier in the thesis. Therefore, during the pre-processing stage, the properties of the liquid metal domain are not left as constant. Therefore, user-defined functions (UDF) for the thermophysical properties of Liq. sodium, LBE, and mercury then were imported to ANSYS Fluent for simulation setup. The UDF for the liquid metals are mentioned below.

C code UDF for thermophysical properties of Mercury:

```
#include "udf.h"
DEFINE_PROPERTY(cell_density,c,t)
{
    real rho;
    real temp = C_T(c,t);
    rho = 13479.2246;
    rho = 13595*(1-(1.8144*pow(10,-4)*(temp-273.15))-(7.016*pow(10,-9)*pow((temp-273.15),2))-(2.8625*pow(10,-14)*pow((temp-273.15),3))-(2.617*pow(10,-14)*pow((temp-273.15),4)));
    return rho;
}
DEFINE_PROPERTY(cell_thermcond,c,t)
{
```

```

real ktc;
real temp = C_T(c,t);
ktc = 8.8150;
ktc = 8.178+(1.36*pow(10,-2)*(temp-273.15))-(6.378*pow(10,-8)*pow((temp-
273.15),2));
return ktc;
}
DEFINE_PROPERTY(cell_viscosity,c,t)
{
real mu;
real e = 2.71;
real temp = C_T(c,t);
mu = 0.00137266;
mu = 0.3*pow(10,-3)*pow(temp,0.07939)*pow(e,(341.13/temp));
return mu;
}

```

C code UDF for thermophysical properties of LBE:

```

#include "udf.h"
DEFINE_PROPERTY(cell_density,c,t)
{
real rho;
real temp = C_T(c,t);
rho = 10368.84;
rho = 11105-1.3312*temp;
return rho;
}
DEFINE_PROPERTY(cell_thermcond,c,t)
{
real ktc;

```

```

real temp = C_T(c,t);

ktc = 11.8866;
ktc = 5.3557+1.181*pow(10,-2)*temp;
return ktc;
}
DEFINE_PROPERTY(cell_viscosity,c,t)
{
real mu;
real e = 2.71;
real temp = C_T(c,t);
mu = 0.0019897;
mu = 5.293*pow(10,-4)*pow(e,(732.3/temp));
return mu;
}

```

C code UDF for thermophysical properties of Liq. Sodium:

```

#include "udf.h"
DEFINE_PROPERTY(cell_density,c,t)
{
real rho;
real temp = C_T(c,t);
rho = temp*(temp*(0.9667*(pow(10,-9))*(temp)-0.46005*pow(10,-5))-
0.1273534)+954.1579;
return rho;
}
DEFINE_PROPERTY(cell_thermcond,c,t)
{
real ktc;
real tf;

```

```
real temp = C_T(c,t);
tf = 1.8*(temp-273.15)+32;
ktc = 93.9892-3.2503*pow(10,-2)*tf+3.6197*pow(10,-6)*pow(tf,2);
return ktc;
}
DEFINE_PROPERTY(cell_viscosity,c,t)
{
real mu;
real den;
real a;
real b;
real e = 2.71;
real temp = C_T(c,t);
den = temp*(temp*(0.9667*pow(10,-9)*temp-0.46005*pow(10,-5))-
0.1273534)+954.1579;
a = 0.11259*pow(10,-3)*pow(e,((749.08*den)/(1000*temp)));
b = pow((1000/den),0.333);
mu = a/b;
return mu;
}
```


Appendix B

ANN Python Code

ANN algorithm coded in Python used for regression analysis:

In	<pre> import pandas as pd import numpy as np import scipy import matplotlib.pyplot as plt import random from tensorflow import keras from keras.models import Sequential from keras.layers import Dense from sklearn.model_selection import train_test_split data=pd.read_csv("C:\\Users\\Gaurav\Desktop\Python\Major Project 2\Data_Na_final.csv") data </pre>						
Out	L	k	Re_h	Pr_h	Tci		
	0	0.25	77.6152	145789.4063	0.006005	373	2649.451347
	1	0.25	77.6152	291578.8125	0.006005	373	3453.452115
	2	0.25	77.6152	437368.2189	0.006005	373	3821.511607

```

3    0.25  77.6152  583157.6252  0.006005  373  5647.157290
4    0.25  76.0660  167354.7188  0.005341  373  2646.666140
...   ...   ...      ...      ...      ...   ...
175  1.00  69.1950  776405.7500  0.004775  473  5365.491489
176  1.00  66.8475  205837.1875  0.004600  473  2575.018789
177  1.00  66.8475  411674.3750  0.004600  473  3357.247517
178  1.00  66.8475  617511.5625  0.004600  473  4328.683755
179  1.00  66.8475  823348.7500  0.004600  473  5337.052672

```

180 rows x 6 columns

```

In X=pd.DataFrame(data,columns=['L','k','Re_h','Pr_h','Tci']).to_numpy()

Y=pd.DataFrame(data,columns=['Ui']).to_numpy()

X_train, X_test, Y_train, Y_test = train_test_split(X, Y, test_size=0.5,
random_state = 42)

X_train.shape

Y_train.shape

```

```

Out (90, 5)

(90, 1)

```

```

In X_mean = X_train.mean(axis=0)

X_train -= X_mean

X_std = X_train.std(axis=0)

X_train /= X_std

Y_mean = Y_train.mean(axis=0)

Y_train -= Y_mean

Y_std = Y_train.std(axis=0)

```

```
Y_train /= Y_std  
X_test -= X_mean  
Y_test -= Y_mean  
X_test /= X_std  
Y_test /= Y_std  
n_cols=X.shape[1]
```

```
In model = Sequential()  
model.add(Dense(6,activation='relu',input_shape=(n_cols,)))  
model.add(Dense(10,activation='relu'))  
model.add(Dense(6,activation='relu'))  
model.add(Dense(1))  
model.compile(optimizer='adam',loss='mse')  
model.fit(X_train, Y_train, epochs=1000, batch_size=1)
```

```
Out Epoch 1/1000  
90/90 [=====] - 0s 909us/step -  
loss: 6.2595e-04  
Epoch 2/1000  
90/90 [=====] - 0s 809us/step -  
loss: 8.0311e-04  
Epoch 3/1000  
90/90 [=====] - 0s 831us/step -  
loss: 4.6923e-04  
Epoch 4/1000  
90/90 [=====] - 0s 864us/step -  
loss: 2.5882e-04  
Epoch 5/1000
```

	<pre> 90/90 [=====] - 0s 820us/step - loss: 3.2099e-04 </pre>
In	<pre> Y_pred=model.predict(X_test) Y_pred2= Y_pred*Y_std + Y_mean Y_test2= Y_test * Y_std + Y_mean print("Mean Absolute Error: %f" % np.mean(np.absolute(Y_pred- Y_test))) print("Mean Squared Error (MSE) : %f" % np.mean((Y_pred - Y_test)**2)) print("RMS Error: %f" % (np.mean((Y_pred-Y_test)**2)**0.5) Y1 = np.sum((Y_test- Y_pred)**2) Y2 = np.sum((Y_test - np.mean(Y_test))**2) R2 = 1 - Y1/Y2 R2 </pre>
Out	0.9864
In	<pre> Y_dat = np.concatenate((Y_pred2, Y_test2),axis=1) np.savetxt('ANN_data_Na.csv', Y_dat , delimiter=',') </pre>

The above code is used for applying ANN regression algorithm for predicting the overall heat transfer coefficient by learning from half of the dataset and then testing the accuracy from the other half, this particular code contains 3 hidden layers with 6, 10, 6 nodes respectively.

LIST OF PUBLICATIONS

1. *Gaurav Krishnayatra*, and Rajesh Kumar, “Convective Heat Transfer Analysis of Longitudinal Fins on Horizontal Hollow Cylinder”, *International Journal of Mechanical and Production Engineering (IJMPE)*, 7 (11), 32-37, 2019. URL-
http://www.iraj.in/journal/journal_file/journal_pdf/2-615-157839106232-37.pdf
2. *Gaurav Krishnayatra*, Sulekh Tokas, Rajesh Kumar, and Mohammad Zunaid, “3 Dimensional CFD analysis of Laminar Flow Natural Convection of Hollow Cylinder with Annular Fins”, *Proc. 5th World Cong. Mech. Chem. Mat. Engg.*, HTFF-181 (1-10), 2019. DOI: 10.11159/htff19.181.
3. *Gaurav Krishnayatra*, Sulekh Tokas, and Rajesh Kumar, “Numerical heat transfer analysis & predicting thermal performance of fins for a novel heat exchanger using machine learning”, *Case Studies in Thermal Engineering*, 21, 100706, 2020. DOI: <https://doi.org/10.1016/j.csite.2020.100706>
4. Sulekh Tokas, *Gaurav Krishnayatra*, and Mohammad Zunaid, “Numerical investigation of thermal performance of extended surface for a novel heat exchanger”, *Wiley – Heat Transfer*, 2020. DOI: <https://doi.org/10.1002/htj.21879>
5. *Gaurav Krishnayatra*, Sulekh Tokas, Rajesh Kumar, and Mohammad Zunaid, “Parametric study of natural convection showing effects of geometry, number and orientation of fins on a finned-tube system: a Numerical approach”, *Journal of Thermal Engineering*, Yildiz University Press. [Article in Press]
6. *Gaurav Krishnayatra*, and Rajesh Kumar, “Comparison of k-Nearest Neighbor and Generalized reduced gradient algorithm for Non-linear Multivariable Regression analysis of Buoyancy Driven Heat Transfer”, *Australian Journal of Mechanical Engineering*, Taylor & Francis Publications. [Under Review]